INFRARED SPECTROSCOPY OF ACETYLENE, CARBON MONOXIDE, AND DEUTERATED HYDROGEN CYANIDE FOR PLANETARY ATMOSPHERIC APPLICATIONS

KOOROSH ESTEKI
Bachelor of Science, Foulad University of Technology, 2012

A Thesis
Submitted to the School of Graduate Studies
of the University of Lethbridge
in Partial Fulfilment of the
Requirements for the Degree

MASTER OF SCIENCE

Department of Physics and Astronomy
University of Lethbridge
LETHBRIDGE, ALBERTA, CANADA

INFRARED SPECTROSCOPY OF ACETYLENE, CARBON MONOXIDE, AND DEUTERATED HYDROGEN CYANIDE FOR PLANETARY ATMOSPHERIC APPLICATIONS

KOOROSH ESTEKI

Date of Defence: July 18, 2016

Dr. Adriana Predoi-Cross Co-Supervisor	Professor	Ph.D.
Dr. Behnam Seyed-Mahmoud Co-Supervisor	Associate Professor	Ph.D.
Dr. Albert Cross Thesis Examination Committee Member	Adjunct Professor	Ph.D.
Dr. Brant Billinghurst Thesis Examination Committee Member	Adjunct Professor	Ph.D.
Dr. Kenneth Vos Chair, Thesis Examination Committee	Associate Professor	Ph.D.

Abstract

I present the results of three spectroscopic projects. First, we analysed spectra of acetylene diluted by carbon dioxide (CO_2) in the R-branch region of the v_1+v_3 combination vibrational band (6470-6618 cm^{-1}). The spectra were recorded over a range of pressures between 50 to 500 Torr and temperatures between 216 to 333 K. The objective was to obtain the CO_2 broadened Lorentz half width, line-shift parameters as well as their temperature dependency for all measurable transitions. Second, we have re-analyzed high-resolution, room temperature spectra of pure CO and CO broadened by hydrogen recorded in the spectral range of the first overtone band. Self- and H_2-broadened line parameters were obtained for 48 ro-vibrational transitions. Third, we studied the infrared emission spectra of Deuterium Cyanide (DCN) in the 450 to 850 wavenumbers range, recorded at 1370 K at the Justus-Liebig University, Giessen, Germany. We report the ro-vibrational constants for the DCN molecule.

Acknowledgements

> *"I can understand pessimism, but I don't believe in it. It's not simply a matter of faith, but of historical evidence. Not overwhelming evidence, just enough to give hope, because for hope we don't need certainty, just possibility."*
>
> Howard Zinn

I would like to take this chance and express the deepest gratitude towards all who helped me to conclude my commitment to this study. Frist of all, it was a great honor to work, be educated and instructed by a women in Physics, Professor Adriana Predoi-Cross. She was patient, kind and persuasively conveyed the spirit of science in her research and teaching. I will defiantly miss working with her.

Next, I would like to give my especial appreciation to my co-supervisor, Professor Behnam Seyed Mahmoud. I consider myself very lucky to have had him in my supervisory committee. I appreciate his guidance during my research activities.

I also would like to thank my supervisory committee member Drs. Albert Cross and Brant Billinghurst. Dr. Albert Cross' comments in my supervisory committee meetings were very helpful to my research. Dr. Brant Billinghurst has been extremely helpful in advancement of my spectroscopic knowledge.

Moreover, I would like to thank all undergraduate and graduate students for their assistance in my research and their friendship, especially to Dr. Chad Povey, Mr. Hossein Naseri, Miss. Robab Hashemi and Hoimonti Rozario. Among my friends, I would to thank my very close and supportive friends Hossein Hosseini, Farzin Keykavoos and Lucía Isabel for their friendship and moral support during this journey.

Last but not least, I would like to thank my family: my mother, father, brother Kambiz, my sisters Fataneh, Ghazaleh and Sharareh, and my beautiful niece, Anushka for their support, love and encouragement.

It is greatly acknowledged the financial support that I have received from the School of Graduate Studies at University of Lethbridge, The NSERC CREATE AMETHYST and the Discovery Grant program of the Natural Sciences and Engineering Research Council of Canada (NSERC).

Contents

List of Figures

List of Tables

1. Introduction

1.1. Overview

In this chapter, the advantages of laser and Fourier transform spectroscopy will be presented in the context of high resolution spectroscopic studies, with emphasis on line shape studies. The presence of acetylene (C_2H_2), deuterium cyanide (DCN) and carbon monoxide as trace constituents of planetary atmospheres will be discussed. We review the status of knowledge on line shape studies of acetylene, carbon monoxide and the ro-vibrational energy states of deuterium cyanide in the spectral ranges of interest here. The outline of the thesis will be given at the end of the chapter.

1.2. Spectroscopy

1.2.1. History of spectroscopy and spectra of light

Isaac Newton made several discoveries during his life time such as, the gravitational laws that govern the universe, the invention of calculus and the dissociation of white light into its components (an illustration to rainbows). In 1666, Newton placed a glass prism in front of a narrow ray of sunlight coming from a darkened room. He observed a set of colours on the wall. Newton reversed the process by adding one more prism in the opposite direction, and he understood that it was converted to white light again. In 1672, Newton was the first scientist who introduced the word “spectrum” in his publication in the *Philosophical Transactions* entitled “A New Theory about Light and Colours” [1].

In 1800, the British astronomer Sir William Herschel who discovered the planet Uranus, proved that spectrum of light can be extended beyond the visible range. His need to filter light going to a blackened mercury thermometer bulb to reduce the heat coming through his telescope while studying the sun led him to realize that greater enhancement in temperature was obtained for light of wavelengths just beyond the red. He said [1, 2] “I likewise conclude that the full red falls still short of the maximum of heat, which perhaps lies even a little beyond visible refraction. In this case radiant heat will at least partly, if not chiefly consist, if I may be permitted the expression, of invisible light . . . .” Finally, this observation led him to discover the *infrared* range of electromagnetic light. Three years after, the ultraviolet range was discovered by Johann Wilhelm Ritter while he was testing the effect of light of different colors on silver salts.

James Clerk Maxwell, Scottish scientist, is known as one of the greatest mathematical physicist of all time. He made contributions to the theory of color conception (Maxwell color triangle), to the kinetic theory of gases (Maxwell-Boltzmann equation which describes the distribution of speed for a gas at the given temperature) and to the thermodynamics (the well-known Maxwell relations). However, his greatest achievement arises from applications of his famous equations in electromagnetism to light. He concluded that light is propagating through space as electromagnetic waves. Later on, this concept has been experimentally demonstrated by several scientists such as Heinrich Hertz and Augusto Righi [1].

In 1905 Albert Einstein, a German-born theoretical physicist, visualized light as tiny quantized packets and particles that he named “photons”. Einstein explained the Max Planck's blackbody spectrum by interaction of photons. This history gives rise to quantum mechanics, and a field of study, the interaction of electromagnetic of light with matter known as “*spectroscopy”*.

The term "laser" stands for "Light Amplification by Stimulated Emission of Radiation". Laser radiation is emitted monochromatic, coherent and directional.

Since the first laser was built by H. Maiman in 1960 [3], the applications of lasers have expanded in many aspects of our lives, such as: laser cutting, laser printers, optical disc drives, fiber optics, barcode scanners, laser pointers, free-space communication (using light to propagate in vacuum space to wirelessly transfer data by optical communication technology for telecommunications), laser surgery and spectroscopy.

Spectroscopic remote sensing studies of planetary atmospherics rely on having available accurate sets of line parameters for the majority of trace constituents that can be extrapolated at pressures and temperatures specific to each remote environment. Databases such as HITRAN [4, 5] and GEISA [6] store the results of the most appropriate and reliable laboratory data sets (retrieved experimental results) obtained through laser and/or Fourier Transform spectroscopy, complemented by theoretical studies.

Lasers can be classified based on the active medium that have been used to generate the population inversion and the lasing process, namely: solid state lasers, gas lasers, dye or liquid lasers, excimer lasers, and semiconductor lasers [7]. The spectra of acetylene perturbed by carbon dioxide presented in this thesis have been collected using a semiconductor Tunable Diode Laser Spectrometer (TDLS) system. This laser system has been described in details and diagrams in chapter 3 of Ref [8].

1.2.2. Fourier Transform Spectroscopy and its applications

FTIRS is the acronym for Fourier Transform Infrared Spectrometry, a spectroscopic technique that in the past few decades has proven to be a robust and reliable analytical technique used in many research and industrial applications. In the late 19th century, the physicist Michelson built an interferometer [9], and as early as 1892, Rayleigh [9] realized that the interferogram can be related to the absorption/emission spectrum by a mathematical function known as Fourier Transformation. From that time, this technique has been used frequently in spectroscopy and by the invention of digital computers, spectroscopists have been able to perform the transformation rapidly and efficiently. A diagram of a simple Michelson transform spectrometer is shown on Figure 1.1.

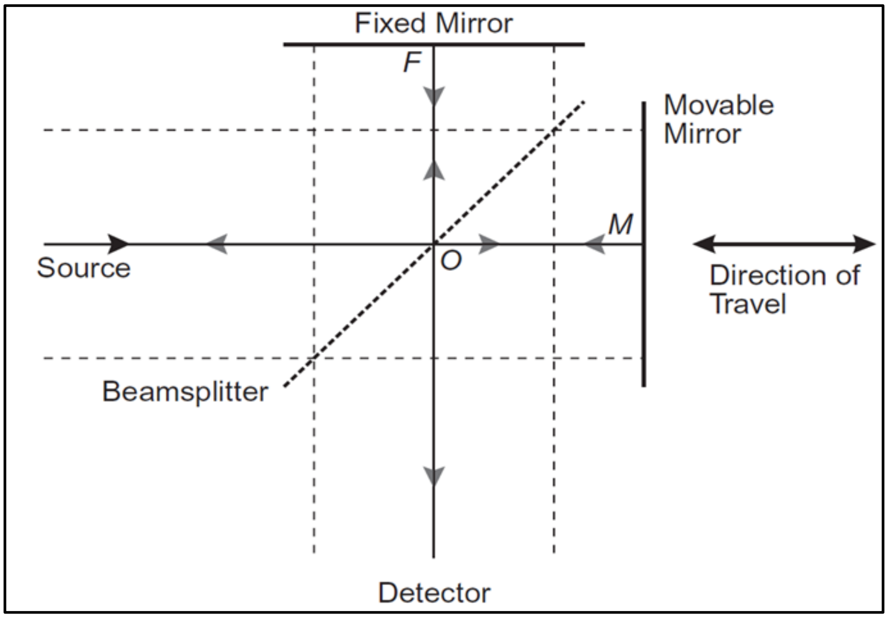

Figure 1.1. An overview of a Fourier transform spectrometer [10].

An interferometer is provided with optical components including: light source, beam splitter, fixed mirror, moving mirror, sample (in this study a tube filled with the interest of gas) and a detector. As shown in the Fig.1.1, the incoming infrared light source hits the beam splitter, and splits into two optical beams. One component of the incident beam is reflected off by the fixed mirror, and the other one will be bounced back of the moving mirror. The moving mirror is attached to a mechanism that allows it to travel a distance back and forth (the maximum distance travelled depends on its design) from the beam splitter. These two reflected beams interference after meeting again at the beam splitter. Due to the fact that the path of one ray is fixed (stationary mirror), and the other path constantly changes (movable mirror), the detector collects the signals of these two beams that overlap and interfere with each other. If the two rays are in phase, they will create a constructive interference. If not, a destructive interference occurs. The optical path difference (δ, or optical retardation) is defined as the path difference that were traveled by the two incident beams (δ = OM-OF, see Fig.1.1). Constructive interference takes place at the following given wavelength:

$$\delta = n\lambda \tag{1.1}$$

and for the destructive interference:

$$\delta = (n + 1/2)\lambda \tag{1.2}$$

where n = 0, 1, 2, 3, 4, … and λ is the wavelength of the incident beam.

The measurement is called an interferogram which contains information acquired simultaneously at each infrared frequency. However, the measured information cannot be analyzed directly since a plot of the intensity at each individual frequency is needed in order to make an interpretation. This can be accomplished through the mathematical process known as Fourier transformation.

There are several reasons why Fourier transform spectrometer has more popularity over similar spectroscopic techniques. FTIRS has the capability to measure all the incident IR (infrared) radiations that pass through the sample at once. This feature is called Jacquinot advantage or throughput. The Jacquinot advantage can increase the SNR (signal to noise ratio) due to the fact that there is no restriction on the wavelength range and thus the intensity of the IR radiation will not diminish. Moreover, this advantage makes FTIR to be a faster spectroscopic technique.

The second advantage is called the “Fellgett or multiplex” advantage. This characteristic is based upon the fact that all the wavelength of light can be detected by the detector at once while in other techniques only a small portion of wavelength of light is measured. Since the noise at each wavelength is proportional to the square root of the time spent detecting that wavelength, the SNR will enhance by measuring the entire wavelength.

The third advantage of the FTIRs is called the “Connes” advantage. A He-Ne (Helium Neon) laser is used to scale the wavelength of an interferometer because the wavelength of this laser is known precisely and is stable. Consequently, this wavelength calibration of interferometer has much better long term stability and is much more reliable than the calibration of dispersive instruments [11].

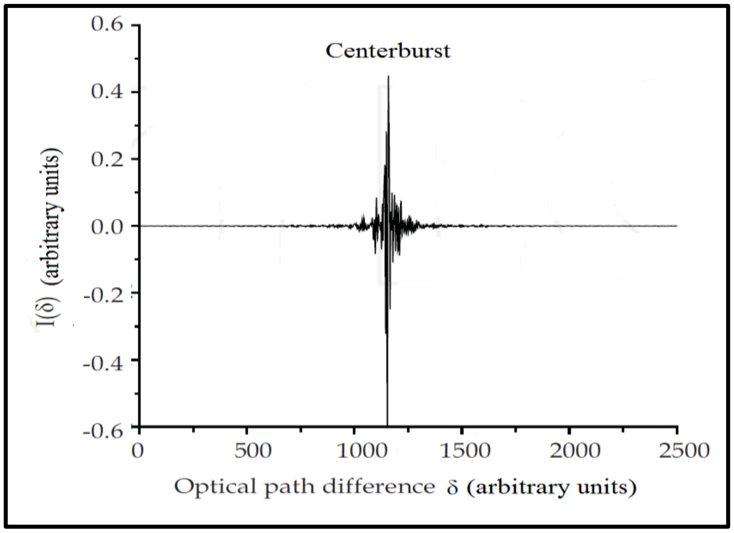

Figure 1.2. An overview of an interferogram [12].

An example of an interferometer is shown in Fig. 1.2. An interferogram can be written as sum of sinusoidal waves. This sinusoidal waves represent the information about the given wavelength peak and amplitude corresponding to that wavelength. Therefore, the infrared spectrum can be calculated using the Fourier transform analysis.

The *zero path difference* (ZPD) happens if the stationary and moving mirrors are the same distance from the beam splitter results in having same distance traveled by two beams that reflect off mirrors. A sharp intensity spike at the ZPD which is depicted in Fig 1.2 is called *center burst*. This sharp intensity illustrates that all the wavelengths constructively interference at the ZPD.

The resolution of the spectra can be estimated using the following expression [11]:

$$Resolution = \frac{1}{\Delta} \tag{1.3}$$

in which Δ is the maximum retardation and is equal to 2δ since the beam travels once to the moving mirror and again travels back to the beam splitter.

Since the resolution is inversely proportional to the time, it is possible to have control on the velocity of the moving mirror to change the resolution by the following expression [11]:

$$F_V = 2VW \tag{1.4}$$

where V is the velocity of the moving mirror, the F_V is the modulation frequency and W is the wavelength of the light in the interferometer. Therefore, the user should consider the speed of the moving mirror since it affects the resolution of the spectra recorded by the FTIRS.

1.2.3. Brief overview of reveal of acetylene studies

Acetylene is a linear, light molecule having the chemical formula of C_2H_2 that was first discovered by Edmund Davy in 1836 and named “new carburet of hydrogen” [13]. Acetylene was rediscovered by the French scientist Marcellin Berthelot in 1860 and was renamed “acetylene” [14]. This molecule plays an active chemical role as trace constituent of the Earth’s atmosphere [15]. It has been reported that the planetary atmospheres of Mars [16], Titan [17], Jupiter [18] and Saturn [19] also contain acetylene. Its presence as a trace constituent of Titan's atmosphere has been reported by the Cassini satellite instrument [20]. An investigation by Brooke *et al.* [21] illustrated that the infrared spectrum of the comet Hyakutake has strong absorption bands attributable to acetylene. Furthermore, due to the linear, simple and light features that this molecule has, it has become an ideal test molecule for line shape models [22], as proven by the extensive laboratory studies on acetylene during recent decades.

A summary of previous studies of acetylene broadened by different buffer gasses is given in the Table 1-1. More details regarding these published works are given in appendix A at the end of present document.

Table 1-1: Summary of previous studies of acetylene broadened by different buffer gases.

Vib. Band	Temp.(K)	Buffer Gas	Ass. Range	Line shape function[a]	Ref.
ν_5	297	N_2, O_2	P(29)-R(25)	VP	[23]
ν_5	297	N_2, O_2	P(35)-R(34)	Theoretical (RB)	[24]
ν_5	147-295	H_2, N_2,He, Ar	P(8)-R(21)	VP	[25]
ν_5	296	H_2, N_2, He, Ar	R(3)-R(34)	Theoretical(RB)	[26]
ν_5	173.4	N_2	P(29)-R(28)	RP,Theoretical(RB)	[27]
$\nu_4+\nu_5-\nu_4$	296	N_2, He	Q(1)-Q(35)	Theoretical(ECS)	[28]
$2\nu_5-\nu_5$	296	N_2, He	Q(1)-Q(35)	Theoretical(ECS)	[28]
$\nu_4+\nu_5-\nu_4$	183.2,198.2	N_2, He	Q(1)-Q(35)	Theoretical(ECS)	[29]
$2\nu_5-\nu_5$	183.2,198.2	N_2, He	Q(1)-Q(35)	Theoretical(ECS)	[29]
$\nu_4+\nu_5$	296	N_2, air	P(31)-R(20)	VP	[30]
$\nu_4+\nu_5$	173.2-273.2	N_2	P(1)-R(23)	VP, RP	[31]
$\nu_4+\nu_5$	298	N_2	P(17)-R(22)	VP, RP	[32]
$\nu_4+\nu_5$	173.2-298.2	N_2	P(11)-R(23)	VP, RP, GP	[33]
$\nu_1+\nu_3$	295	H_2, N_2, D_2, Air	P(31)-R(27)	VP	[34]
$\nu_1+\nu_3$	296	C_2H_2, N_2	P(11)	VP, RP, GP	[35]
$\nu_1+\nu_3$	195,373,473	N_2	P(25)-R(25)	VP	[36]
$\nu_1+\nu_5$	296	C_2H_2,N_2,Ar	R(0)-R(7),Q(7)-Q(29)	RP	[37]
$\nu_1+3\nu_3$	298	N_2, O_2, He, Ar, Ne, Kr, Xe	P(17)-R(22)	GP, RP	[38]
$\nu_1+\nu_2+\nu_4+\nu_5$	213-350	C_2H_2	R(0)-R(19)	VP, SDV	[39]
$\nu_1+3\nu_3$	296	C_2H_2	P(10)-R(14)	VP	[40]
$\nu_1+\nu_3$	296	O_2, N_2, CO_2	P(26)-P(22)	VP	[41]
$\nu_1+\nu_3$, $\nu_1+\nu_3+\nu_4-\nu_4$	296	C_2H_2	P(26)-P(15)	VP	[41]
ν_5	173.2	O_2	P(29)-R(29)	VP, RP	[42]
$\nu_1+3\nu_3$	296	C_2H_2, O_2, Air	P(7)-P(15), R(9), R(11)	VP	[40]
ν_2	174,134, 295	Ar	Q(1)-Q(23)	VP, RP	[43]
$\nu_4+\nu_5$	296	C_2H_2	P(22)-R(23)	VP, RP	[44]
$\nu_1+\nu_3$	195	H_2, D_2	P(26)-R(26)	VP	[45]
$\nu_1+\nu_3$	296	C_2H_2	P(15)-P(6)	VP, RP	[46]
$\nu_1+\nu_3$	213-333	N_2	P(31)-R(33)	VP, RP	[47]
$\nu_4+\nu_5$	298	CO_2	P(23)-R(23)	VP,RP,GP	[48]
$\nu_1+\nu_3$	296K	N_2	P(21),P(16),P(19),R(16),R(19),R(21)	VP,SDV,RP, GR, RGP, CR, SDR, CSDR	[49]

[a] VP: Voigt Profile, RP: Rautian Profile, SDV: Speed Dependent Voigt Profile, GP: Galatry Profile, RGP: Rautian-Galatry Profile, CR: Correlated Rautian, SDR: Speed Dependent Rautian, CSDR: Correlated Speed Dependent Profile. For line shape profiles, see section 2.2.9 to 2.2.14. For RB and ECS model, refer to ref. [27] and [29].

1.3. Deuterium Cyanide (DCN) and its Astrophysical Importance

The hydrogen cyanide (HCN) and its isotopomers have received interest from the astronomical community since its observation (interstellar region) in 1970 using a radio telescope at the National Radio Astronomy laboratories [50]. Furthermore, a study of the rotational transition from J=1 to J=2 by Penzias and Wilson [51] lead them to the discovery of DCN molecules in the Orion star-forming region.

DCN as a less abundant isotopomer of HCN has been found to be in higher concentrations than expected in the cold interstellar medium [52]. Astronomical observations carried out using the James Clerk Maxwell Telescope on Mauna Kea, Hawaii [53] enabled the detection of DCN in a comet. Astrophysicists have concluded that the D/H ratio observed indicates a kinetic temperature in the 10 to 30 K temperature range.

Due to the astrophysical importance of HCN and DCN, extensive theoretical and experimental studies have been done on these two gasses, resulting in highly precise line parameters. A brief review of DCN studies will be given in this section.

Winnewisser and Vogt [54] have measured the *l*-type doublet transitions of isotopic species of HCN including $H^{13}C^{14}N$, $H^{12}C^{15}N$, $H^{13}C^{15}N$, $D^{13}C^{14}N$, $D^{12}C^{15}N$ and $D^{13}C^{15}N$ using a Hewlett-Packard spectrometer, model 8460 MRR working in the microwave range. The authors have computed the coupling values of the ro-vibrational (rotational and vibrational) interaction in this bending mode. Preusser and Maki [55] have published ro-vibrational term values of $H^{13}C^{14}N$, $H^{12}C^{15}N$, $H^{13}C^{15}N$, $D^{13}C^{14}N$, $D^{12}C^{15}N$ and $D^{13}C^{15}N$ within the range of 138 and 483 GHz for up to v=3.

Six ro-vibrational parameters of several isotopic species of deuterium cyanide and hydrogen cyanide have been measured by Maki *et al.* [56]. A newly designed Fourier transform emission setup was used by Quapp *et al.* [57] to record the spectral hot emission of $D^{13}C^{15}N$ gas in the range of 450 to 700 cm^{-1}. The authors have studied the spectroscopic constants of bending modes belonging to $v_2 = 1$ to 12. In addition, they have reported the room temperature absorption spectroscopic values of several states of DCN, $D^{13}C^{14}N$, and $D^{12}C^{15}N$.

Möllmann *et al.* [58] have measured the spectral emission of $D^{12}C^{14}N$ and $D^{13}C^{14}N$ at 1370 K and 1520 K in the 450 to 850 cm^{-1} and 1800 to 2800 cm^{-1} region, respectively, using a high resolution Bruker IFS 120 Fourier transform spectrometer equipped with a Ge:Cu detector cooled with liquid-helium. They have investigated the ro-vibrational molecular constants for both mentioned gasses in cm^{-1} after correcting for *l*-type resonance.

In addition, several studies on Hydrogen cyanide, its isotopomers and especially on Deuterium atom have been carried out [59-63]. It is believed that the Deuterium atoms have played a remarkable role in the Big Bang event because theoretically most of the Deuterium detected in nature was created around 13.8 billion years ago during the Big Bang [64].

1.4. Carbon Monoxide As A Trace Constituent of The Interstellar Medium and Planetary Atmospheres

Carbon Monoxide (CO) is a simple diatomic molecule belonging to the $C_{\infty v}$ point group that has been the subject of a number of spectroscopic studies due to its presence as a trace constituent in the cloud mass offering clues to the evolution of galactic and extragalactic (extragalactic astronomy is related to the study of the region outside the Milky Way galaxy) astronomy. A Connes-type Fourier spectrometer located at the McDonald Observatory working at a 0.2 cm^{-1} apodized resolution has revealed the presence of carbon monoxide in the lower layer of Jupiter's atmosphere [65]. The first detection of the fundamental band (0-1) of Carbon Monoxide in the Saturn's atmosphere was done using a Fabry Perot spectrometer having 0.15 cm^{-1} resolution situated at the Astronomical Observatory on Mauna Kea, Hawaii [66]. Moreover, the observation of ro-vibrational transitions belonging to the first and second overtones of carbon monoxide (0-2 and 0-3) was performed using the James Clerk Maxwell Telescope [67]. Additionally, 115 GHz microwave of rotational transitions of this gas were observed in the Mars atmosphere [68]. In the other investigations, the presence of carbon monoxide in the Venus atmosphere was proven as well with CO mixing ratios increasing above 85 km [69]. In addition, many missions, such as the Global Atmospheric Composition Mission [GACM], the Active Sensing of CO_2 absorption over Nights, Days and Seasons [ASCENDS] and the Geostationary Coastal and Air Pollution Events [GEO-CAPE] are mapping the global CO concentrations sing spectra recorded in 2.3 micron region [70].

Furthermore, hydrogen (H_2) is known as a dominant interstellar molecule of the Milky Way covering an immense portion of the Galactic circle. Interestingly, the quadrupolar rotational transitions of this light gas (H_2) can be observed in the infrared region. Accordingly, studying the line shape spectra of carbon monoxide using high resolution spectrometers is needed to accurately retrieve the line shape spectroscopic parameters in order to model the density of molecular clouds [71].

A summary of previous studies of carbon monoxide broadened by different buffer gasses is given in the Table 1-2. More details regarding these published works are given in appendix B at the end of present document.

Table 1-2. Summary of previous studies of carbon monoxide in the first overtone band broadened by different buffer gases.

Vib. Band	Temp.(K)	Buffer Gas	Ass. Range	Line shape function	Ref.
(2-0), (3-0)	296	CO	P(21)-R(21)	LP	[72]
(2-0)	295	H_2, N_2	P(20)-R(20)	LP	[73]
(2-0)	297	CO	P(31)-R(31)	LP	[74]
(2-0)	299	N_2, O_2,H_2,HCl,NO,CO_2,CO	P(22)-R(22)	LP	[75]
(2-0)	85-298	CO	P(23)-R(23)	LP	[76]
(2-0)	296	CO, N_2, He, Kr, O_2	P(7)-R(22)	LP	[77]
(2-0)	296	CO, N_2	P(20)-R(23)	VP, LP	[78]
(1-0), (2-0)	174-296	CO, Air	P(24)-R(27)	–	[79]
(2-0)	296	CO, H_2	P(27)-R(27)	VP	[80]
(2-0)	297-301	CO	P(23)-R(24)	VP, SDV	[81]
(1-0), (2-0), (3-0)	83-302	H_2	P(20)-R(21)	–	[82]
(1-0), (2-0)	298	H_2, Air	P(26)-R(22)	LP	[83]
(2-0)	296	CO, H_2	P(24)-R(25)	VP	[84]
(2-0)	151-298	CO, Air	P(29)-R(30)	VP, SDV	[70]

1.5. Thesis Layout

Chapter 1 introduces a brief definition of laser spectroscopy and its application in the remote sensing technique. Furthermore, a review on previous studies of acetylene, deuterated hydrogen cyanide and carbon monoxide are given in this chapter.

Chapter 2 presents topics in molecular spectroscopy that are relevant to the work presented in this document. The basics of pure rotational, pure vibrational spectroscopy for linear molecules will be described in details, to facilitate an accurate description of the features observed in spectra recorded in the near infrared (NIR), infrared (IR) and far - infrared (FIR) regions of the electromagnetic spectrum. Moreover, in this chapter we will present the background knowledge necessary for spectroscopic line shape studies and for assigning transitions. We will introduce several line shape functions to account for different effects and to precisely model the molecular motion at different temperatures and pressures.

Chapter 3 presents the experimental set-ups used in the experiments described here and the software used to analyze the spectral data. We will describe the 3 channel tunable diode laser spectrometer used to study the absorption line shapes of acetylene mixed by carbon dioxide located in the Department of Physics and Astronomy at University of Lethbridge. The emission spectra of DCN were recorded at Justus Liebig University, Giessen, Germany using a Fourier Transform IFS 120 HR spectrometer and a quartz cell mounted inside an oven. The experimental details will be given in this chapter.

Chapter 4 presents the study of the v_1+v_3 combination band of acetylene perturbed by carbon dioxide using a tunable diode laser. The broadening, line pressure-shift and their temperature dependence coefficients have been found employing different line shape models that were described in details in chapter 2 compared with results from the literature are also presented.

Chapter 5 presents the study of the emission spectra of deuterium cyanide gas. The assignment of highly excited emission spectra of this hot gas has been carried out using the spectroscopic analysis software SyMath described in details in chapter 3. Finding the ro-vibrational energy levels enabled us to assign thousands of transitions. Additionally, a comparison between the present work and those published in Ref. [58] showed a good agreement in the retrieved molecular constants.

Chapter 6 will represent the spectroscopic study on pure carbon monoxide and carbon monoxide diluted in hydrogen. The self- and H_2- broadened Lorentz half-width, self- and H_2-pressure-induced shift and line mixing coefficients for CO transitions in the first overtone band was performed on spectra recorded at the National Solar Observatory on Kitt Peak, AZ.

Chapter 7 briefly describes the conclusions of spectroscopic studies presented in this thesis, as well a summary of possible improvements and directions for future work that can be carried out. A list of the references used in this research work is given at the end of the document.

2. Theoretical Perspective

2.1. Overview

In this chapter I will present the background spectroscopic knowledge needed to describe the ro-vibrational spectra for linear polyatomic molecules. At first, I will give a brief description of light and its interaction with atoms and molecules. The fundamental quantum mechanical equations that explain the pure rotational, pure vibrational and the ro-vibrational spectra will be presented. Furthermore, line shape functions that can describe the observed spectral profiles will be covered in this chapter. Finally, the quantum mechanical theory needed to understand the energy levels of DCN gas will be outlined. Unless otherwise stated, the information included in this chapter has been taken from the references [55, 85, 86].

2.2. Principles of Spectroscopy

2.2.1. Light and its interaction with matter

Light consist of electromagnetic radiation that propagates with the speed of 299792458 m/s in vacuum. The electromagnetic spectrum of light can be quantified by a range of possible frequencies of electromagnetic filed. Fig.2.1. [87] is an example of electromagnetic spectrum from gamma rays to radio wave.

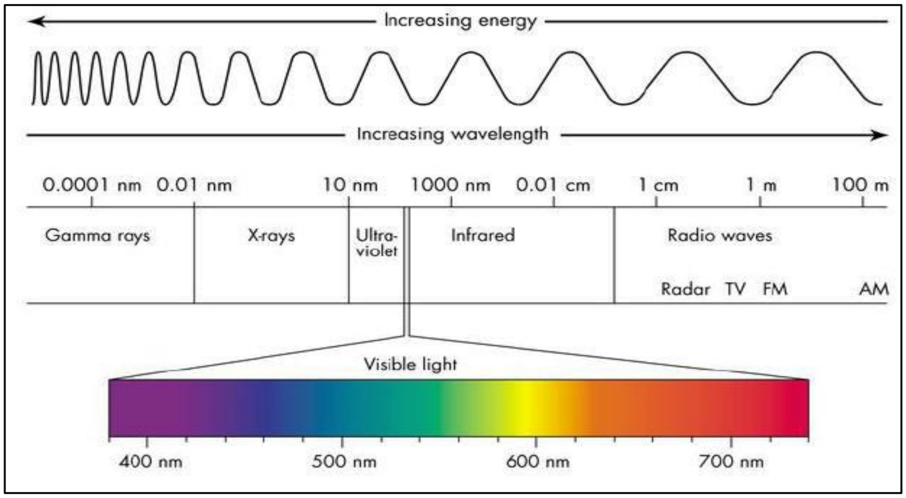

Figure 2.1. The electromagnetic spectrum of light [88].

Light consists of transverse waves such that the plane in which the electric field $\overrightarrow{E}$ and magnetic field $\overrightarrow{H}$ propagate, are perpendicular to each other and to the direction of wave propagation. A simple wave traveling along the x-axis can be written by the following equations:

$$E_y = E_{yo} \sin(2\pi\nu t - \mathrm{k}x) \quad \text{and} \tag{2.1}$$

$$H_z = E_{zo} \sin(2\pi\nu t - \mathrm{k}x) \tag{2.2}$$

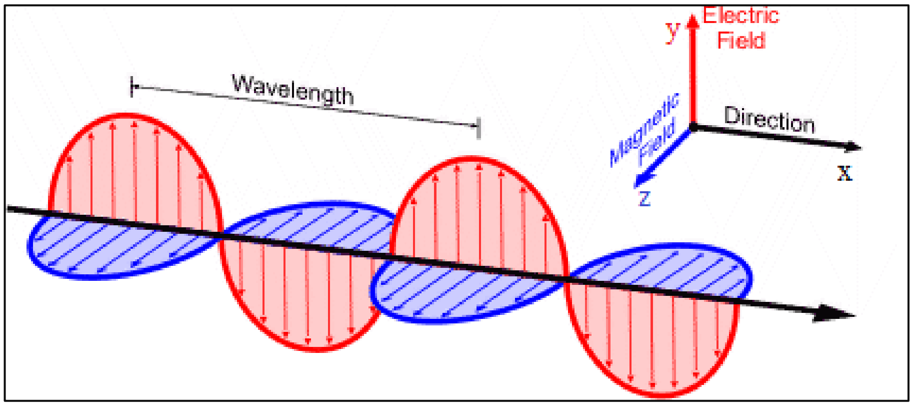

Figure 2.2. Electromagnetic propagation diagram [88].

where E_{yo} and H_{zo} are the amplitude of the electric field and magnetic field, respectively. ν is the frequency of light, k is the wave vector, *t* is time and x represents the direction of propagation. These two equations illustrate that electromagnetic wave components are made of periodic functions of sinusoidal structure both in time and space. The frequency of light can be related to different regions of spectrum as shown in Fig.2.1.

To understand the interaction of light with matter, we can assume a quantum mechanical mechanism using a set of *N* two eigenstates in a volume of 1 m^3 with upper energy E_1 and lower energy E_0. Fig.2.3. depicts three possible processes that may take place in a two-level system.

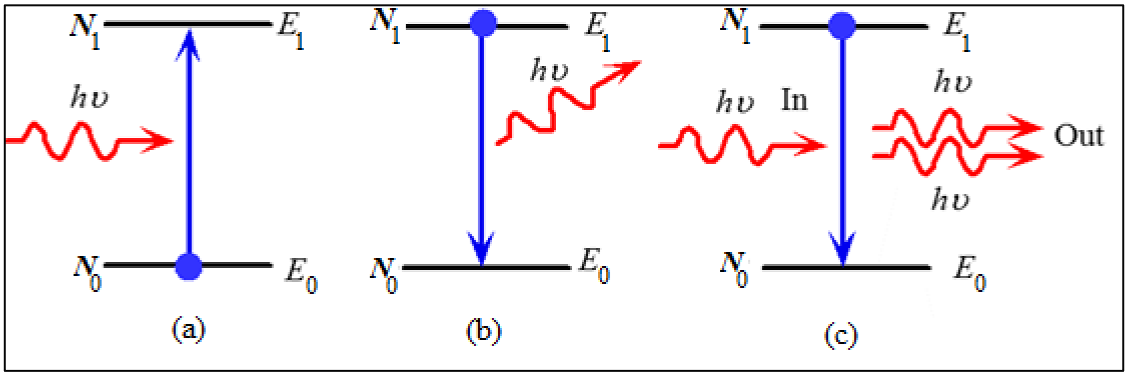

Figure 2.3. Three different possibilities that may happen to the two level-system when light interacts with matter. (a) Absorption. (b) Spontaneous emission. (c) Stimulated emission [88].

This exchange of energy between defined two-level systems can be written as:

$$\Delta E = E_1 - E_0 = h\nu \qquad (2.3)$$

where E_1 and E_0 are the corresponding upper and lower energy states, respectively, *h* is the well-known Plank’s constant (6.62607004 ×10^{-34} m^2kg/s) and ν is the frequency of the incident photon.

The three possibilities can be described as follows:

(a) *Absorption:* An incident photon is absorbed by the atom (molecule) M in the lower level E_0 causing a transition to atom M^* in the upper state E_1.

$$M + h\nu \rightarrow M^* \tag{2.4}$$

(b) *Spontaneous emission*: The energy of the system spontaneously falls down from upper to the lower level producing a photon with energy pack of $h\nu$.

$$M^* \rightarrow M + h\nu \tag{2.5}$$

(c) *Stimulated emission:* An incident photon hits an excited atom resulting in de-excitation in the energy of the system from upper to the lower level.

$$M^* + h\nu \rightarrow M + 2h\nu \tag{2.6}$$

Due to the fact that the system in Fig.2.3. is in thermal equilibrium, if we assume that the number of systems with energy of E_0 and E_1 are N_0 and N_1, respectively, then the relation between populations ($N = N_0 + N_1$) will be defined as:

$$\frac{N_1}{N_0} = e^{-h\nu/K_BT} \tag{2.7}$$

This ratio indicates the changing in the rate of population in which $\Delta E = E_1 - E_0 = h\nu$, K_B is Boltzmann constant ($1.38064852 \times 10^{-23}$ $m^2kgs^{-2}K^{-1}$) and T is the temperature.

When the emission/absorption frequency between two energy surfaces, from ground to the excited state or vice versa, is identical to the frequency of the incident photon, then any of the physical processes of absorption, spontaneous or stimulated emission will take place. The rate of change in population for an induced absorption can be expressed by:

$$\frac{dN_1}{dt} = B_{1\leftarrow 0}\rho_\nu N_0 \tag{2.8}$$

where $B_{1\leftarrow 0}$ is the "rate constant" also known as the Einstein B coefficient and ρ_ν is the universal Planck function (i.e. the radiation density):

$$\rho_{\nu}(T) = \frac{8\pi h\nu^3}{c^3}\frac{1}{e^{h\nu/K_BT}-1} \tag{2.9}$$

Similarly, an expression can be defined to explain the stimulated emission condition by:

$$\frac{dN_1}{dt} = -B_{1\rightarrow 0}\rho_{\nu}N_1 \tag{2.10}$$

The absorption and stimulated emission are opposite processes occurring at different population rates. Thus, it can be concluded that:

$$B_{1\leftarrow 0} = B_{1\rightarrow 0} \tag{2.11}$$

And finally, the expression for spontaneously emitted photons in a system is:

$$\frac{dN_1}{dt} = -A_{1\rightarrow 0}N_1 \tag{2.12}$$

In equation (2.12), the absence of ρ_{ν} implies that the process is spontaneous, and $A_{1\rightarrow 0}$ is also referred as “Einstein *A* coefficient”. Since the entire system is in equilibrium, the relationship between absorption, spontaneous and stimulated emission is as follows:

$$\frac{dN_1}{dt} = B_{1\leftarrow 0}\rho_{\nu}N_0 - B_{1\rightarrow 0}\rho_{\nu}N_1 - A_{1\rightarrow 0}N_1 = 0 \tag{2.13}$$

Equation (2.13) can be rewritten as:

$$B_{1\leftarrow 0}\rho_{\nu}N_0 = B_{1\rightarrow 0}\rho_{\nu}N_1 + A_{1\rightarrow 0}N_1 \tag{2.14}$$

By comparing equations (2.14) and (2.7), they can be written as:

$$\frac{N_1}{N_0} = \frac{B_{1\leftarrow 0}\rho_{\nu}}{A_{1\rightarrow 0} + B_{1\rightarrow 0}\rho_{\nu}} = e^{-h\nu/K_BT} \tag{2.15}$$

If equation (2.15) is solved for ρ_{ν}, then this formula changes to:

$$\rho_{\nu} = \frac{A_{1\rightarrow 0}}{B_{1\leftarrow 0}e^{h\nu/K_BT} - B_{1\rightarrow 0}} \tag{2.16}$$

By combining equation (2.16), (2.9) and (2.11), an expression between two Einstein coefficients *A* and *B* can be derived as:

$$A_{1\rightarrow 0} = \frac{8\pi h\nu^3}{c^3}B_{1\leftarrow 0} \tag{2.17}$$

in which c is the speed of light, h is Planck constant and ν is the frequency of interest. Moreover, equation (2.17) can be revised in terms of wavelength using following expression:

$$\lambda = \frac{c}{\nu} \tag{2.18}$$

where ν is the frequency and λ is the wavelength of light.

2.2.2. Schrödinger Equation

In quantum mechanics the Schrödinger equation describes the evolution of a quantum state of an atom (or molecule) with respect to time. The solution to this differential equation offers an accurate picture of the wave functions and energy eigenvalues. The time-dependent of Schrödinger is given by the following expression:

$$i\bar{h}\frac{\partial}{\partial t}\Psi(r,t) = \hat{H}\Psi(r,t) \tag{2.19}$$

where $\bar{h}$ is the reduced Plank constant ($\bar{h} = \frac{h}{2\pi}$, h is Planck constant), *i* is the imaginary number, Ψ is the wave function of the system and $\hat{H}$ is the Hamiltonian operator quantifying both the kinetic and potential energies. The general time-independent Schrödinger equation can be formed as:

$$E\Psi = \hat{H}\Psi \tag{2.20}$$

in which *E* corresponding to the energy of the state Ψ.

An atom (or molecule) consists of a combination of negatively charged electrons and positively charged nuclei. Hence, it is a challenging task to precisely predict the motion of the components of such a system (due to the Heisenberg uncertainty principle). For this reason, the overall motion of the quantum system can be split into several quantities as initially proposed by Born and Oppenheimer in 1927. The concept of this separation is simple, keeping in mind that the mass of a nucleus is 1835 times larger than the mass of an electron, therefore, electrons can move faster than the nucleus. Consequently, we can assume that dynamically they are acting independently. The whole energy of such a system can be defined by the sum of three components: electronic, vibrational, and rotational energies associated to the three types of motion.

$$E_{total} = E_{elctronic} + E_{rotation} + E_{vibration} \tag{2.21}$$

The type of spectra studied in this work correspond to ro-vibrational transitions that will be explained in further detail.

2.2.3. Pure Rotational Spectra

2.2.3.1. Rigid Rotor model

The simplest mechanical model that has been proposed to characterize the rotating diatomic molecule is known as the rigid rotor model (or dumbbell), shown schematically in Fig.2.4. [89]. This model postulates that two atoms m_1 and m_2 have been fixed in their position bond length “r” and rotate about its center of mass axis. The rotational energy of an object in classical mechanics is given by:

$$E_{rot} = \frac{1}{2} I \omega^2 \tag{2.22}$$

in which ω is the angular velocity and the I is the moment of inertia of the rotating object.

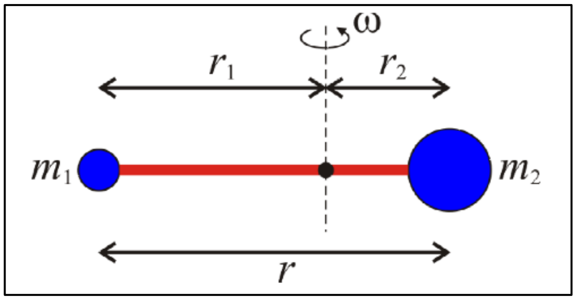

Figure 2.4. The diatomic rigid rotor model demonstrating the rotation along the axis normal to the internuclear axis.

The moment of inertia of a diatomic molecule can be described by the:

$$I = \mu r^2 \quad \text{and} \tag{2.23}$$

$$\mu = \frac{m_1 m_2}{m_1 + m_2} \tag{2.24}$$

where r is the bond length, μ is the reduced mass, and m_1 and m_2 are the masses of atoms. In the quantum mechanical approach, equation (2.22) will be converted to following equation:

$$E_{rot}(J) = \frac{h^2}{8\pi^2 I} J(J+1) \tag{2.25}$$

where J is the so-called rotational quantum number and can have the integer values of $J = 0,1,2, \ldots.$ To make equation (2.25) simpler, it can be rewritten to:

$$F(J) = \frac{E_{rot}(J)}{hc} = BJ(J+1) \quad \text{and} \tag{2.26}$$

$$B = \frac{h}{8\pi^2 cI} \tag{2.27}$$

where $F(J)$ is the rotational energy in wavenumber units and B is the rotational constant. The position (energy level) of each transition can be computed by:

$$\bar{\nu} = F(J+1) - F(J) = 2B(J+1) \tag{2.28}$$

where $\bar{\nu}$ is given in wavenumber units.

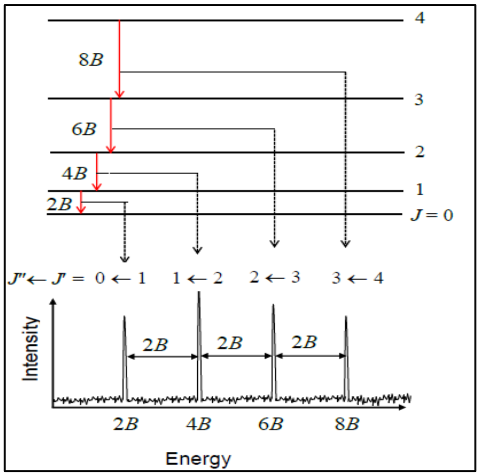

Figure 2.5. Schematic diagram of energy levels showing rotational transitions and the section of the spectrum corresponding to the transitions [90].

The intensity of a rotational transition depends on the permanent dipole moment and the population difference between the two states between which the transition occurs. So, if the total concentration of molecule is N, then the concentration of this molecule with respect to rotational quantum number J is determined by [85, 86]:

$$N_J = N(2J+1)\frac{e^{-BJ(J+1)/K_BT}}{q_r} \quad \text{and} \tag{2.29}$$

$$q_r = \sum_J (2J+1)\, e^{-BJ(J+1)/K_BT} = \frac{K_BT}{\sigma B} \tag{2.30}$$

where q_r is the rotational partition function, σ is 2 or 1 depending on if the molecule is symmetrical or non-symmetrical, respectively.

To obtain the rotational quantum number for which the maximum of population occurs, the equation (2.30) and (2.29) must be solved:

$$\frac{d(N_J/N)}{dJ} = 0 \quad \text{and following it} \tag{2.31}$$

$$J_{max} = \left(\frac{K_B}{2B}\right)^{1/2} - \frac{1}{2} \tag{2.32}$$

2.2.3.2. Non-Rigid Rotor model

To validate the rigid rotor theory, many experiments have been done in laboratories, and it has became obvious that the spacing between lines is not exactly $2B$. Due to the rotation of the molecule, the bond length will increase and thus the molecule will experience the larger moment of inertia that leads to a centrifugal distortion force. For this reason, a non-rigid rotor model has been proposed which assumes that the bond length of atoms are acting as a spring as shown in Fig.2.6.

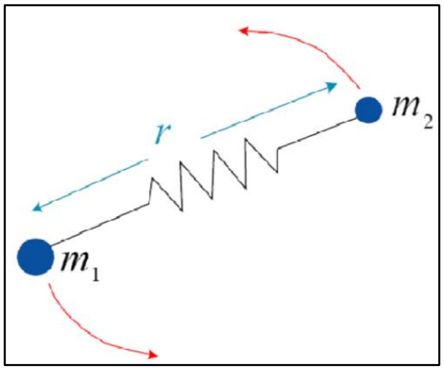

Figure 2.6. Diagram of a non-rigid rotor model of a diatomic molecule. Atoms are connected with a spring of force constant “k” that can be stretched by rotation [89].

The expression that describes the rotational energy by taking the centrifugal distortion constant into account is defined by:

$$F(J) = BJ(J+1) - D[J(J+1)]^2 \tag{2.33}$$

where D is the centrifugal distortion constant. So, now the transition wavenumber will be converted from equation (2.28) to a more accurate expression as follows:

$$\bar{\nu} = F(J+1) - F(J) = 2B(J+1) - 4D(J+1)^3 \tag{2.34}$$

Moreover, the centrifugal distortion constant can vary based upon the stiffness of the bond and of the vibrational wavenumber:

$$D = \frac{4B^3}{\omega_e{}^2} \tag{2.35}$$

where ω_e is defined as the vibrational wavenumber or the harmonic vibrational frequency.

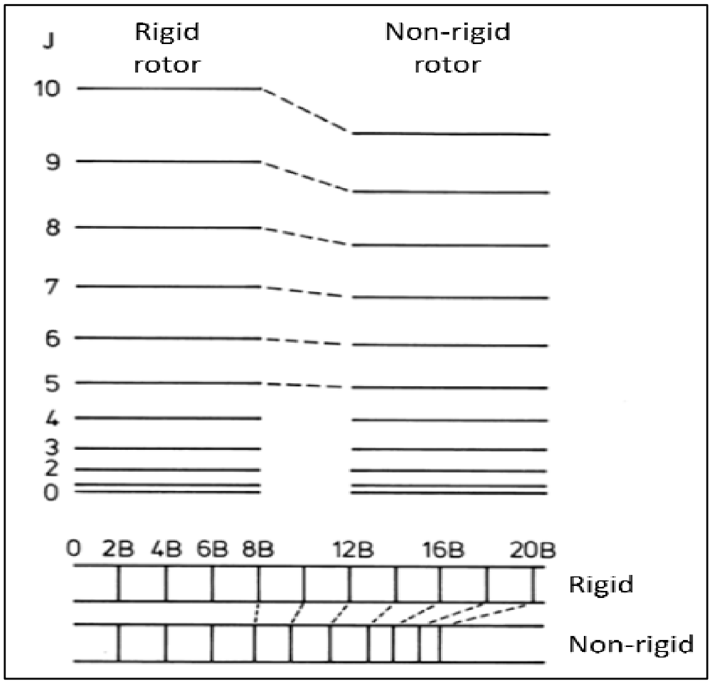

Figure 2.7. Comparison between the energy levels of a diatomic molecule considered rigid and non-rigid. As shown, after considering the centrifugal distortion effect, the distance between energy states decreases [88].

2.2.4. Pure Vibrational spectra

2.2.4.1. The Harmonic Oscillator

The Harmonic oscillator is the first approximation suggested to simulate the vibration of the diatomic molecule as shown in Fig.2.6. where the two atoms are connected by a spring. The vibrational energy eigenvalues for a simple Harmonic oscillator model after solving the SchrÖdinger equation is given by:

$$G(v) = h\omega(v + \tfrac{1}{2}) \tag{2.36}$$

in which ω is the classical vibrational wavenumber depending on the reduced mass μ and the force constant, k, h is the Planck's constant, and v is the so-called vibrational quantum number $v = 0,1,2,3, \dots$.

The classical vibrational wavenumber can be written as follows [82]:

$$\omega = \frac{1}{2\pi c}\left(\frac{k}{\mu}\right)^{1/2} \tag{2.37}$$

The selection rule for a harmonic oscillator is $\Delta v = \pm 1$. However, since $\Delta v = v_{upper} - v_{lower}$ then only the $\Delta v = +1$ transitions will be allowed to take place for given vibrational quantum numbers. A diagram of the harmonic oscillator has been drawn on Fig.2.8.

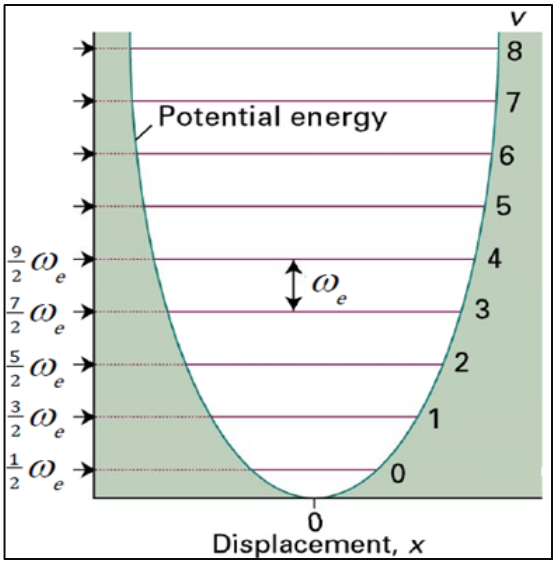

Figure 2.8. Overview of the harmonic oscillator and its distribution of energy levels [91].

Above expression (2.36) can be extended to describe a polyatomic molecules motion in a harmonic case. Therefore, the individual energies of a linear N-atoms molecule, in total 3N-5values for a harmonic oscillator in a non-degenerate case, will be the given as follows:

$$G(v, v_1, v_2, \dots) = \omega_1\left(v_1 + \frac{1}{2}\right) + \omega_2\left(v_2 + \frac{1}{2}\right) + \dots + \omega_{3N-5}\left(v_{3N-5} + \frac{1}{2}\right) \sum_{i=1}^{3N-5} \omega_i\left(v_i + \frac{1}{2}\right) \tag{2.38}$$

where the ω_i and is the vibrational wavenumber corresponding to ith mode of vibration and v_i is the vibrational quantum number. For a molecule with degenerate energy levels, it can be modified to correspond to the following expression:

$$G(v, v_1, v_2, \dots) = \sum_{i=1}^{3N-5} \omega_i\left(v_i + \frac{d_i}{2}\right) \tag{2.39}$$

in which d_i is the degeneracy of the ith mode of the vibration.

2.2.4.2. The Anharmonic Oscillator

When the molecule vibrates intensely, a harmonic oscillator model can no longer offer an accurate picture of the dynamical motion of the molecule. The harmonic oscillator assumption is true as long as the bond length of the molecule obeys Hooke's law meaning that stretched bond length (r) is not very different than the equilibrium bond length (r_e).

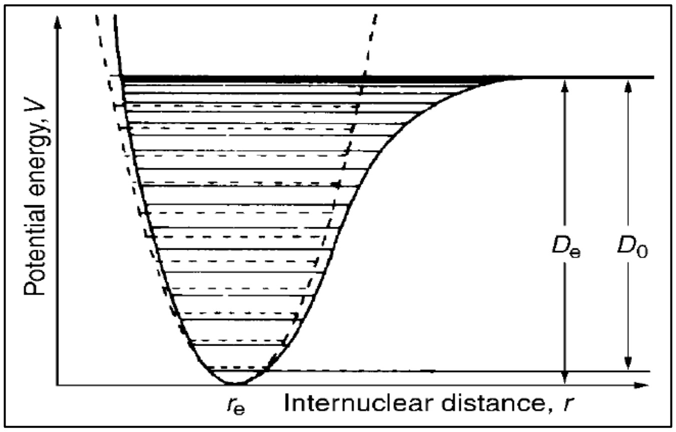

Figure 2.9. The dash lines represent the harmonic oscillator pattern. The curved solid line indicates the anharmonic model. D_e and D_o are the measured dissociation energy relative to the equilibrium potential energy and the dissociation energy relative to the real ground state states, respectively [8].

In reality, this assumption is not valid since when the molecule has a large amount of energy, then it can vibrate in a large distance, and as a result experiencing the phenomena of dissociation. This phenomena drives the molecule to form two neutral atoms far away from each other ($r \approx \infty$) causing the force constant to be equal to zero. Fig.2.9. is a good example of comparison between the anharmonic oscillator and harmonic oscillator cases.

The first effect due to this condition is the selection rule that will change from $\Delta v = \pm 1$ to $\Delta v = \pm 1, \pm 2, \pm 3, \ldots$ where $\Delta v = \pm 2, \pm 3, \ldots$ are called overtone transitions and are usually weaker than those that have $\Delta v = \pm 1$. The second effect is that the spacing will not be the same as depicted in Fig.2.8. To compensate for assumption in an anharmonic case, the following expression has been introduced (in the case of a Morse potential) for the vibrational energy eigenvalues:

$$G(v) = \omega_e \left(v + \frac{1}{2}\right) - \omega_e x_e (v + \frac{1}{2})^2 + \omega_e y_e (v + \frac{1}{2})^3 + \cdots \qquad (2.40)$$

where ω_e is the classical vibrational wavenumber, v is the vibrational quantum number $v = 0,1,2,3, \ldots$ and x_e, y_e, … are the anharmonic constants. A good approximation can be given by the expression (2.41) to approximate the dissociation energy relative to the equilibrium condition:

$$D_e \approx \frac{{\omega_e}^2}{4\omega_e x_e} \qquad (2.41)$$

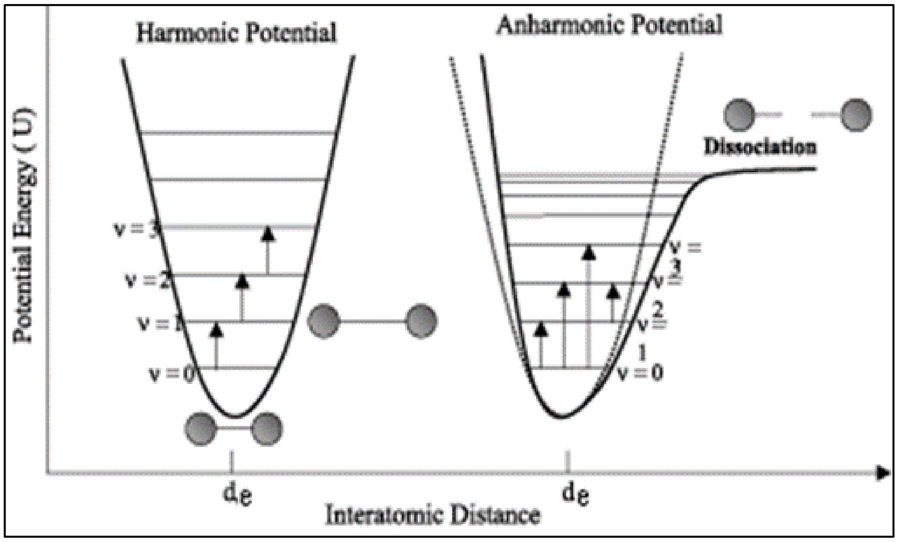

Figure 2.10.Comparison between the harmonic and anharmonic oscillator models. As it represents, in the anharmonic case the two atoms dissociate at larger distance [91].

Equation (2.40) can be expanded to develop a new expression for a polyatomic molecule in the anharmonic case like the way described in section 2.2.4.1. Consequently, an expression for a linear n-atoms molecule without any degeneracy is:

$$G(v, v_1, v_2, \dots) = \sum_{i=1}^{3N-5} \omega_i \left(v_i + \frac{1}{2}\right) + \sum_i \sum_{k \geq i} x_{ik} \left(v_i + \frac{1}{2}\right) \left(v_k + \frac{1}{2}\right) + \cdots \qquad (2.42)$$

and for a system with having degeneracy in the energy levels, d_i , it will be modified to the following expression:

$$G(v, v_1, v_2, \dots) = \sum_{i=1}^{3N-5} \omega_i \left(v_i + \frac{d_i}{2}\right) + \sum_i \sum_{k \geq i} x_{ik} \left(v_i + \frac{d_i}{2}\right) \left(v_k + \frac{d_i}{2}\right) + \cdots \qquad (2.43)$$

where x_{ik} is the anharmonic constant term.

2.2.5. Vibrational Angular Momentum

The normal vibrational mode of every N-atoms linear and nonlinear molecule can be computed by 3N-5 and 3N-6, respectively [62]. The degeneracy occurs when two bending modes orthogonal to each other vibrate with the same energy. Fig.2.11. depicts a polynomial linear molecule with two red and blue curves pointing in direction of the two planes in which the molecule vibrates. The fact that the molecule can vibrate in both planes (Y and Z) gives rise to the rotation of the nuclei about its intermolecular axis. Since the rotation can be in either the clockwise or the counter clockwise, the degeneracy of the system can be visualized in both directions.

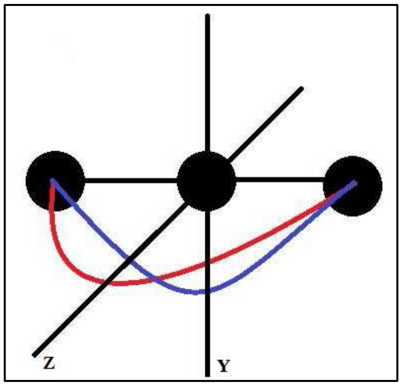

Figure 2.11. This figure illustrates the bending vibrational modes causing vibrational angular momentum [8].

The angular momentum due to vibration must be characterized first. For this purpose, the vibrational angular momentum has been introduced by $\pm l\hbar$ and $l = v_i, v_i - 2, v_i - 4, \ldots, -v_i$ and v_i is the vibrational quantum number for the normal bending mode. A labeling procedure has been designated to determine the vibrational angular momentum by: Σ for *l*=0, Π for *l*=1, Δ for *l*=2 and etc.

The total angular momentum of the system resulting from net angular momentum of vibration ($\vec{l}$) and rotation ($\vec{M}$) must be considered. Then it becomes [4]:

$$\vec{J} = \vec{l} + \vec{M} \tag{2.44}$$

The coupling of these two effects results in the splitting of rotational states, labeled *l*-type doubling, meaning that there are two likely values of ($\vec{l}$) incorporated in each value of ($\vec{M}$).

2.2.6. Selection Rules

Selection rules deal with the probability of a particular transition that can take place in a quantum mechanical molecular system. In order to be able to observe the transition between two ro-vibrational eigenstates, a molecule must have a change in the dipole moment (the dipole moment is related to the distribution of negative charges between two bonds of atom). Therefore, a change in the dipole moment orientation creates two types of rotational-vibrational bands in the case of a polynomial linear molecule, depending on whether the change in dipole moment is parallel or perpendicular to the molecular axis, named parallel and perpendicular band, respectively. Fig.2.12. is an example on how the direction of the dipole moment of a triple atomic molecule can be changed. In this figure (a), the x component of the dipole moment of the molecule (μ_x) oscillates with total frequency of $(f_v + f_r)$ and $(f_v - f_r)$ along the electrical field axis. f_v is the vibrational frequency because of the stretching mode along the dipole moment axis of the molecule (μ) and $f_r$is the rotational frequency along the y-axis. Such a change in the electrical dipole moment of the molecule yields to a group of transitions called parallel bands. Parallel bands have two spectral components: one with lower frequency and the other one with higher frequency, named P- and R-branches, respectively.

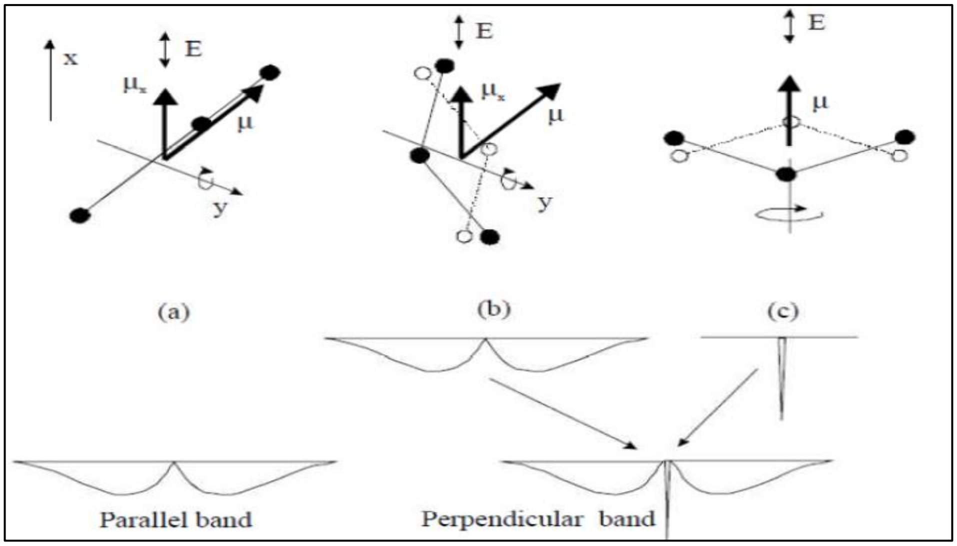

Figure 2.12. Three possible situations that may cause changes to the direction of a dipole moment of a triple atomic molecule that would lead to having parallel or perpendicular bands in the spectrum [92].

If the rotation is orthogonal to the plane in which the molecule bends as shown in Fig.2.12 (b), the same scenario will happen to the orientation of the dipole moment of the molecule causing perpendicular bands containing P- and R-branches as before. However, in Fig.2.12. (c) the molecular rotation along an axis parallel with the electrical field and the dipole moment of molecule, has no influence on the transition dipole moment. Consequently, such a displacement introduces a perpendicular band that includes spectral transitions where the rotational quantum number does not change, called the Q-branch. Fig.2.13. displays an example of the full spectrum of a molecule including all allowed transitions.

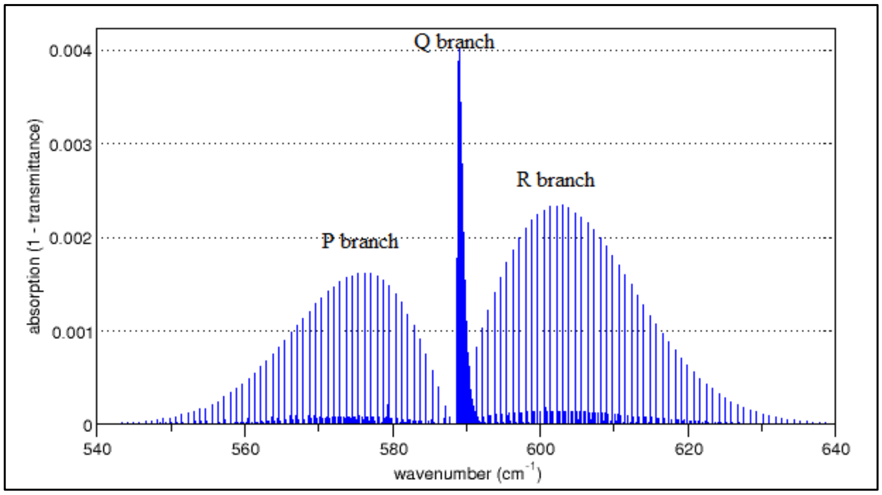

Figure 2.13. Distribution of P-, Q- and R-branches in the electromagnetic spectrum. The Q-branch has very closely spaced lines [93].

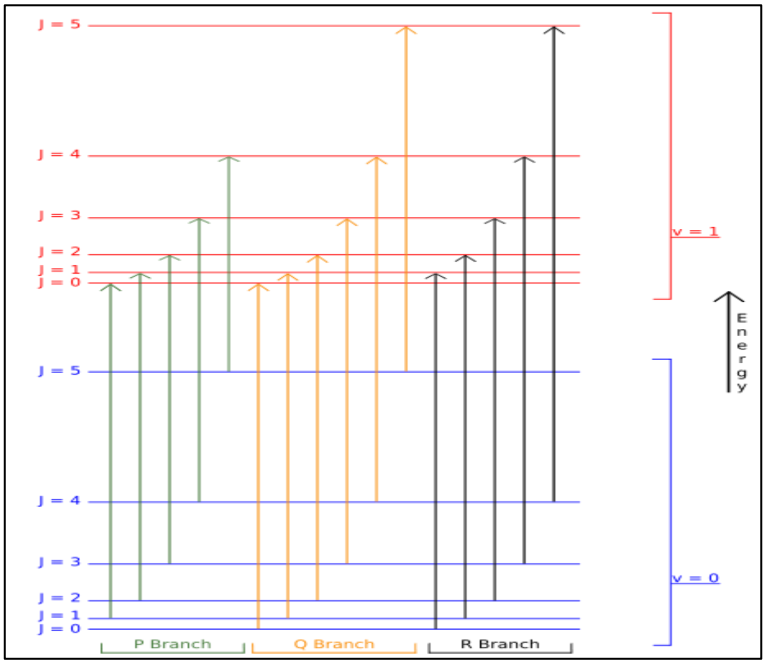

Figure 2.14. Schematic diagram of transitions between two vibrational bands $v = 1$ and $v = 2$ [93].

The transitions in the P-, Q-, R-branches of an absorption spectrum follow the rules (Fig.2.14):

a) If $J + 1 \leftarrow J$ $(\Delta J = -1)$ for P-branch transitions.

b) If $J \leftarrow J$ $(\Delta J = 0)$ for Q-branch transitions.

c) If $J+1 \leftarrow J$ ($\Delta J = 1$) for R-branch transitions.

These selection rules can be extended to more details by considering the vibrational angular momentum such as:

a) If $\Delta l = 0$ and $l = 0$, corresponding to a $\Sigma \leftarrow \Sigma$ type band, leading to a parallel band with P- and R-branches.

b) If $\Delta l = \pm 1$, corresponding to a $\Pi \leftarrow \Sigma,\ \Delta \leftarrow \Pi$ type bands and so on, resulting in forming perpendicular bands that have P-, Q-, and R-branches.

c) If $\Delta l = 0$ and $l \neq 0$, meaning that all transitions belong to parallel bands of $\Pi \leftarrow \Pi, \Delta \leftarrow \Delta$, and so on. The Q-branch transitions are very weak and cannot be visible as fundamental bands in the spectra since the molecule stays in an excited vibrational mode. Moreover, one of the important features of the eigenfunction of a molecule is the parity. If after the inversion of the molecule in the laboratory coordinate system, the sign does not change, then it is considered to be of positive parity, and if the sign changes, then it is considered to be of negative parity.

In the quantum mechanical treatment, two possible eigenvalues have assigned for positive and negative parities by +1 and -1, respectively. However, to simplify the selection rules two new labels: *e* and *f* , have been introduced instead of designating them by +1 and -1. If the parity is given by $(-1)^J$, the energy level is labelled as being of e type. If the parity is given by $-(-1)^J$ the energy level is labelled with *f*. The Fig.2.15 [52] and Table 2.1 illustrate the selection rules of molecules belonging to $C_{\infty v}$ point group [94].

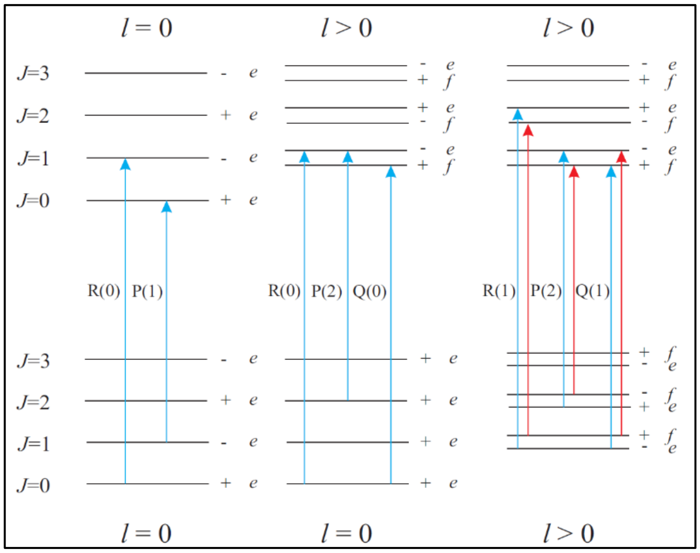

Figure 2.15. Diagram of allowed transitions for DCN gas. A summary these transitions is explained in Table 2.1. The sign of each parity will be given by $(-1)^J$ and $-(-1)^J$as described earlier [94].

Below, in Table 2.1 we present the selection rules of a linear molecule, such as DCN.

Table 2-1. A summary of allowed transition for a molecule belonging to $C_{\infty v}$ such as DCN [94].

Type of transitions	**Assigned selection rules**
$\Sigma \leftrightarrow \Sigma$	$\Delta l = 0$ with $l = 0$ and $\Delta J = \pm 1, e \leftarrow e$
$\Pi \leftrightarrow \Pi$	$\Delta l = 0$ with $l \neq 0$ and $\Delta J = \pm 1, e \leftarrow e, f \leftarrow f$
$\Pi \leftrightarrow \Sigma$	$\Delta l = \pm 1$ and $\Delta J = 0, \pm 1, e \leftarrow e, f \leftarrow f,, e \leftarrow f, f \leftarrow e$

2.2.7. Rotational and Vibrational Spectra

Now that the theoretical aspects governing the motion of an atom (or molecule) during vibration and rotation have been discussed separately, it is possible to go one step further and combine the vibrational and rotational motion of the molecule. It has been illustrated that the best assumption which is close to the reality is that the molecule acts as a non-rigid rotor and has an anharmonic behaviour. By combining the equation (2.34) and

(2.41) which describe the rotational energy levels of a non-rigid rotor ($F(J)$) and the vibrational energy levels of the anharmonic case ($G(v)$), respectively, the total energy of a diatomic molecule will be given by the following expression [85]:

$$T_{v,J} = F(J) + G(v) = B_v J(J+1) - D_v[J(J+1)]^2 + H_v[J(J+1)]^3 + L_v[J(J+1)]^4 + M_v[J(J+1)]^5 + \cdots + \omega_e\left(v+\frac{1}{2}\right) - \omega_e x_e(v+\frac{1}{2})^2 + \omega_e y_e(v+\frac{1}{2})^3 + \cdots \qquad (2.45)$$

where B_v is the rotational constant of the molecule that depends on vibration, D_v is the centrifugal distortion, H_v, L_v and M_v are the higher order terms for small corrections of centrifugal distortion, J and v are the rotational and vibrational quantum numbers, ω_e is the classical vibrational wavenumber and x_e, y_e, … are the anharmonic constants. In this case, two more approximations can be used to describe B_v and D_v terms in above equation as follows [85]:

$$B_v = B_e - \alpha\left(v+\frac{1}{2}\right) + \gamma_e(v+\frac{1}{2})^2 + \cdots \qquad (2.46)$$

$$D_v = D_e - \beta\left(v+\frac{1}{2}\right) + \cdots \qquad (2.47)$$

in which B_e and D_e are the equilibrium rotational and centrifugal distortion constants, α is a molecule specific, positive, constant and β is a correction factor. Similarly, the expression that explains the total ro-vibrational energy levels for a polynomial atomic molecule can be derived by combining equations (2.35) and (2.44).

2.2.8. Absorption Spectra

The experimental set-ups used in absorption experiments on gases include a light source, a single pass or multi-pass cell (such as White cell and Herriott cell which their function is to let light travels more than one way inside the cell by bouncing back and forth from the opposite mirrors in the cell in order to increase the total optical pass through the sample) gas absorption cell and detectors optimized for the range of wavelength of interest. After the light passes through the cell filled with gas, the transmitted radiation can be measured using the detectors. The Beer-Lambert law governs the absorption processes:

$$I_t = I_o e^{-\alpha CL} \tag{2.48}$$

in which I_o is the intensity of light before interacting with sample, I_t is the intensity of light after interacting with sample, α is the absorption coefficient, C is the concentration of gas molecules and L is the pass length of the cell.

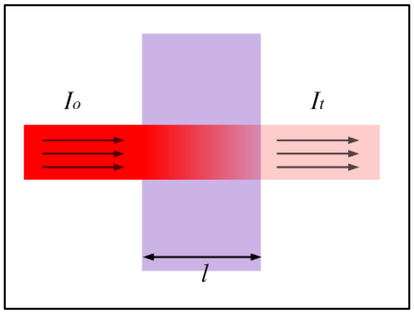

Figure 2.16. Diagram showing the absorption of incident beams of light while passing through a gas sample of pass length *l* [95].

Equation (2.49) can be further modified to new expression to define the *transmission* properties of monochromatic light as follow [8]:

$$\left(\frac{I_t}{I_o}\right) = e^{-\alpha_{\tilde{\nu}}} \tag{2.49}$$

where the $\alpha_{\tilde{\nu}}$ is the variable spectral absorbance that can be broken down into the following formula:

$$\alpha_{\tilde{\nu}} = p\chi_{abs}S(T)\varphi_{\tilde{\nu}}L \tag{2.50}$$

In the above equation, p is the pressure in atm, χ_{abs} is the mole fraction of the absorbing fraction, T is the temperature in Kelvin, S is the intensity of light in cm^{-2}atm^{-1} and $\varphi_{\tilde{v}}$ is the line shape function.

An ideal spectrometer has no influence in the observed line shapes of the spectra. However, in reality every spectrometer has an instrumental line shape (ILS) that must be determined before conducting spectroscopic line shape studies with it.

Three commonly used line shape functions are: the Lorentzian line shape that describes absorption profiles at elevated pressures when the collisional effects are dominant, the Gaussian line shape that describes line profiles when the thermal motion of the molecules is dominant, and the Voigt line shape model that is a convolution of the two processes.

A former Ph.D. student supervised by Professor Adriana Predoi-Cross, Chad Povey [8], had examined the ILS of the laser spectrometer located in the Department of Physics at the University of Lethbridge. He was able to verify that the ILS profile is a Lorentzian line function as presented in section 3.5.3 of his thesis, Ref. [4]. To account for the instrumental line shape, the following equation can be employed to describe the resultant gas absorption line shape recorded with the spectrometer:

$$\varphi_{\tilde{v}} = \varphi_n * ILS = \int_{-\infty}^{+\infty} \varphi_n(\tau) ILS(t-\tau) d\tau \qquad (2.51)$$

Here $\varphi_{\tilde{v}}$ is the final line shape function resulting from the convolution between the ILS and gas absorption line shape φ_n. The Lorentzian, Gaussian and Voigt line shape profiles along with other models will be discussed in details in the next section.

The *impact approximation* in spectroscopy is an approximation widely used in the theory of spectral line shapes. It is mostly used for gases at low densities, however, it can be extended to some more dense cases as well [96]. An isolated line shape will be detuning in the region close to line center ($|\omega-\omega_{fi}|\tau_c << 1$, $\omega=2\pi\nu$). The "*binary collision impact approximation*" assumes that (i) only two molecules collide at a time and (ii) the duration of a collision (τ_c), is much smaller than the time between collisions (τ_d), in the other words $\tau_d >> \tau_c$ [96].

2.2.9. Doppler Line Shape Function

The Doppler Effect occurs due to the fact that the molecules moving away from light and close to the detector absorb the higher frequencies of light. When light waves travel toward the detector, each consecutive wave is emitted at closer distance relative to the detector than the previous wave, which reduces the time to reach the detector. This slightly less time it takes the wave to reach the detector causes an enhancement in frequency. Conversely, if the molecules moving towards the light source and away from the detector, absorb the lower frequencies of the light. This phenomena is pretty common in nature and everybody experiences it with sound waves. Hence, this small shift in frequency must be taken into account in order to accurately extract the absorption profiles.

In general, the energy gap of two transitions can be computed from $\Delta E = E_1 - E_0 = h\upsilon_{1-0}$ only if the line center does not shift in the laboratory frame. If a molecule exhibits a translational movement with respect to the laboratory frame, then the energy gap will be [94]:

$$\Delta E = \upsilon_{1-0}(1 + \frac{\vec{v}\vec{e}}{c}) \qquad (2.52)$$

in which $\vec{v}$ and $\vec{e}$ are the velocity of the molecule and the unity vector representing the diffusional direction of light.

If a system of molecules is in the thermal equilibrium at temperature T, the energy distribution can be described by a Boltzmann distribution. The line shape function that considers this shift is called the Doppler profile (at fairly low pressure, typically p < 1 Torr) and in wavenumber unit ($I(v)_D$) can be expressed by the following Gaussian line shape model [97]:

$$I(v)_D = \frac{1}{\gamma_D}\sqrt{\frac{ln2}{\pi}}\exp[-\left(\frac{v-v_0}{\gamma_D}\right)^2 ln2] \tag{2.53}$$

in which γ_D is Doppler broadening at half width and v_0 is the line centre. The Doppler broadening retrieved from the half width measured at half maximum height of the line is expressed by:

$$\gamma_D = \sqrt{\frac{2k_B T ln2}{mc^2}}v_0 \tag{2.54}$$

where $\gamma_D$is the Doppler broadening at half width, k_B is the Boltzmann constant, T is the temperature, c is speed of light, m is the molecular mass and v_0 is the is the line centre. By substituting the constants in equation (2.55), a further simplification (commonly used) is following expression:

$$\gamma_D = 3.581 \times 10^{-7}\sqrt{\frac{T}{m}}v_0 \tag{2.55}$$

where $\gamma_D$is the Doppler broadening in cm^{-1}

.

2.2.10. Lorentzian Line Shape Function

At high pressures (several hundred Torrs), the molecules interact with one another by collisions in the intermolecular force level. In this region, the spectral line broadening due collisions dominates the Doppler effect. The Lorentzian line shape model has been proposed to take in to account the collisional broadening affected by pressure using following expression [97]:

$$I(v)_L = \frac{1}{\pi}\left[\frac{\gamma_L}{(v-v_0-\Delta)^2+{\gamma_L}^2}\right] \tag{2.56}$$

γ_L is the collisional HWHM (half width half maximum) that can be described by the relationship $\gamma_L = \gamma p$ in which γ is the broadening coefficient at pressure p and $\Delta = \delta p$ where δ is the pressure shift coefficient.

2.2.11. Voigt Line Shape Function

The Doppler and Lorentz profiles can describe the thermal motion of the molecules, and the collisional (pressure) broadening of a spectral line, respectively. However, at intermediate pressures both thermal motion and collisional effects play an important role. Thus, to account for both these effects, the Voigt profile has been proposed as the convolution of Doppler and Lorentzian line shape models expressed by the following mathematical expression [97]:

$$I(v) = \Gamma(v_0)_D\left[\frac{y}{\pi}\int_{-\infty}^{+\infty}\frac{e^{-t^2}}{y^2+(x-t)^2}\,dt\right] \tag{2.57}$$

in which the $\Gamma(v_0)_D$ is peak line center of Doppler line function and x, y and t can be defined by the following expressions:

$$x = \left(\frac{v-v_0-\Delta}{\gamma_D}\right)\sqrt{ln2}; \qquad y = \left(\frac{\gamma_L}{\gamma_D}\right)\sqrt{ln2}; \quad t = \left(\frac{\delta}{\gamma_D}\right)\sqrt{ln2} \tag{2.58}$$

The parameter δ contributes to the frequency differences of Doppler and Lorenz models during the convolution operation and $\Delta = \delta p$. The Voigt Line shape function can reasonably model both thermal motion and collisional broadening as shown in Fig. 2.17.

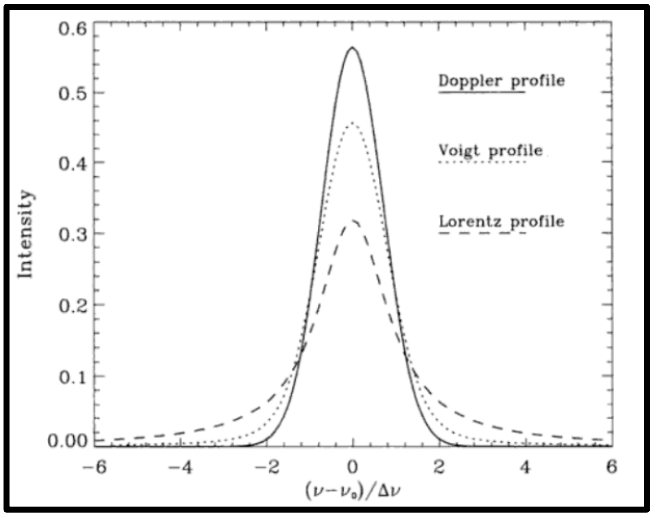

Figure 2.17. A comparison of three line shape functions as indicated on the graph. Voigt model can reasonably cover both thermal motion and molecular collisions [98].

2.2.12. Speed Dependent Voigt Profile

For decades, the Voigt model has been used in radiative transfer codes and in retrievals of gas concentrations or column gas concentration amounts from atmospheric spectra. However, the Voigt model assumes that molecules travel at the most probable speed (the most probable speed is implemented in Doppler line shape model (see page 31 of Ref.[8])).

For this reason, an improved line shape model must be introduced to observe how spectral broadening and shift will be affected by the velocity of the molecules. To account for this effect, that introduces an asymmetry in the line shape, the speed dependent Voigt profile (SDV) [99] has been proposed. The SDV line profile can be generated by the real portion of the Fourier transform of the polarization correlation function and be expressed by the following equation [99]:

$$I(v) = \frac{2}{\pi\Gamma_2} Re[e^{x+2y} \int_0^1 \exp\left[-\left(yz^2 + \frac{x+y}{z^2}\right)\right] dz] \tag{2.59}$$

where *x*, *y* and *z* can be defined by following terms:

$$x = \left(\frac{\Gamma_0}{\Gamma_2} - \frac{3}{2}\right) + i\,\frac{(v - v_0 - \Delta)}{\Gamma_2}\ ;\ y = \frac{1}{\Gamma_2^2}\frac{v_0^2 k_B T}{2mc^2};\ z = (1 + \Gamma_2 t)^{-1/2} \tag{2.60}$$

in which k_B is Boltzmann constant, T is the temperature, m is molecule's mass and c is the speed of light. Γ_0 and Γ_2 are designated to the mean relaxation rate and determination of speed dependence of the relaxation, respectively.

2.2.13. The Soft Collision Profile

The Galatry line shape model or the soft collision model has been introduced [100] to take into account the phenomenon of Dicke narrowing. The Dicke narrowing effect happens if the wavelength of incident beam becomes the same or less than the average distance traveled by the molecules. The Galatry profile or the soft collision profile is expressed using the following line shape function [101]:

$$G(x, y, z) = \frac{1}{\sqrt{\pi}} Re\left(\int_0^{+\infty} \exp\{-(ix + y)\tau + \frac{1}{2z^2}[1 - z\tau - e^{-z\tau}]\} d\tau\right) \tag{2.61}$$

where *x*, *y*, *z* and τ can be written using the following expressions:

$$x = \frac{v - v_0 - \Delta}{\gamma_D}\sqrt{ln2};\ y = \frac{p\gamma}{\gamma_D}\sqrt{ln2};\ z = \frac{p\beta}{\gamma_D}\sqrt{ln2} \tag{2.62}$$

in which γ_D is the Doppler half width explained in 2.3.1. Beta β stands for the narrowing parameter, p is the pressure of sample, and $\Delta = \delta p$.

To accurately predict line shapes that take into account the Dicke narrowing, two types of collisional regimes have been proposed, namely the soft collision and hard collision regimes. The choice of profile can give a better approximation about the line shape, depending on the mass of the absorber (M_1) and the mass of the pertuber (M_2). If the mass of the absorber is very heavy compared to the mass of the pertuber ($M_1 \gg M_2$), the motion of the molecules is represented by soft collisions, resulting in the Galatry line shape model. Conversely, if the mass of the pertuber is very heavy compared to the mass of the radiator ($M_1 \ll M_2$), the motion of the molecules is represented by hard collisions, leading to a hard collision profile which will be discussed in next section.

2.2.14. The Hard Collision profile

Dicke narrowing effects take place usually at the intermediate pressures [8] (few kPa pressure) if the wavelength of the light probing the molecule becomes equal or less than the mean free path of the molecule. The collisions between absorber and the pertuber can be either soft or hard depending on the molecular masses as explained in the previous section. In the case of the hard collision approximation, a new model is proposed by Rautian-Sobelman [102] and Nelkin-Ghatak [103]. The Nelkin-Ghatak model is fundamentally the same as the Rautian-Sobelman model and can reproduce well a line shape by taking into account for the narrowing effect. The hard collision profile can be given by the following form [49]:

$$I(R) = A\ Re[\frac{W(x,y+z)}{1-\sqrt{\pi}zW(x,y+z)}] \tag{2.63}$$

The terms A, x, y and z can be written as follows:

$$A = \frac{S\sqrt{ln2}}{\gamma_D\sqrt{\pi}};\ x = \sqrt{ln2}\ \frac{v-v_0}{\gamma_D};\ y = \sqrt{ln2}\frac{\gamma_C}{\gamma_D};\ z = \sqrt{ln2}\frac{\beta_C}{\gamma_D} \tag{2.64}$$

where γ_C is the collisional half-width, β_C is the narrowing parameter and S is the line intensity. $W(x,y)$ is the complex probability function and for this particular case and can be given by:

$$W(x,y) = \frac{i}{\pi}\int_{-\infty}^{+\infty}\frac{e^{-t^2}}{x+iy-t}dt \tag{2.65}$$

2.2.15. Line Mixing Effects In Spectra Recorded At Elevated Pressures

Another effect that causes asymmetries in spectral line shapes is an interference effect known as line mixing [8]. The line mixing interference phenomena occur in spectra recorded at elevated pressures in the overlapping regions of neighboring transitions. This effect can take place either in any of the P-, Q- or R-branch regions of any molecule. Typically, line mixing can happen easier in the Q-branches which have high densities of spectral lines, as presented in Fig.2.13 [4].

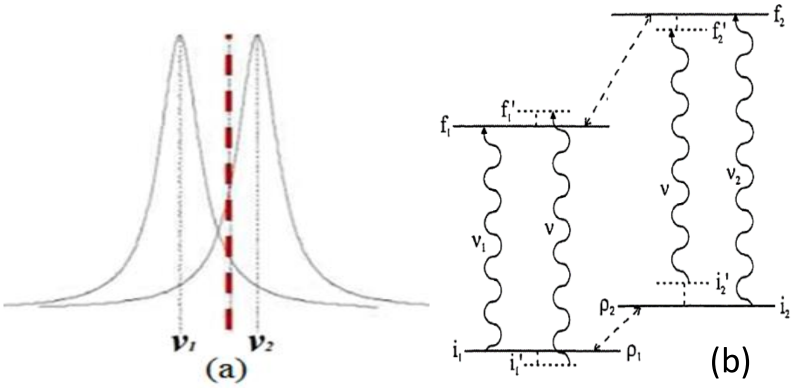

Figure 2.18. An illustration of line mixing effect for two adjacent spectral lines. (a) This diagram shows that in the overlapping range of the two transitions, the absorption can be due to either transition. (b) Schematic diagram of the “two transition model” for line mixing. Individual energy levels are marked by straight lines. Parallel with them, the dashed lines represent molecular energy levels. The collisional coupling between energy levels is illustrated using dashed two sided arrows (Courtesy of Dr. Richard Berman).

Line mixing effect should be taken into account to accurately predict the line shapes. The line mixing effect can be considered in the above mentioned line shape functions (sections 2.2.9 to 2.2.14).

2.3. Spectroscopic Assignments in Deuterated Hydrogen Cyanide (DCN)

DCN is linear molecule which has 4 vibrational modes. They have been named as symmetric CD stretching ν_1, doubly degenerate bending ν_2, and the asymmetric CN stretching ν_3 modes [50]. Fig. 2.19 represents an example of possible vibrational modes of DCN.

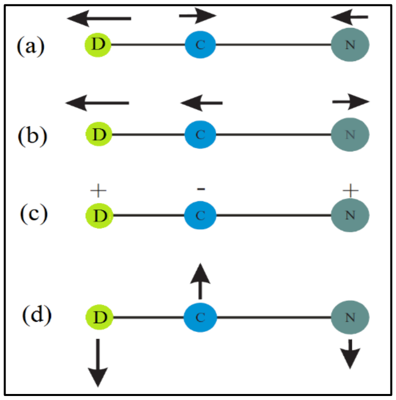

Figure 2.19 (a) CD stretching mode, (b) CN stretching mode, (c) and (d) two fold degenerate bending mode [94].

The process by which we identify the sets of quantum numbers associated with every observed spectroscopic transition is referred to as “assignment”. The observed spectroscopic transitions fulfill the fundamental laws described in section 2.2. The theoretical aspects of the DCN molecules follow the discussion in Ref [58]. We have employed the principles outlined in section 2.2 to obtain the kinetic and potential energies corresponding to the Hamiltonian operator and to predict the ro-vibrational molecular motion by solving the Schrödinger equation for this molecule.

The line positions of the observed transitions fulfill the following equation:

$$\nu_{\text{obs}} = T'(v, l, J, e\,/\,f) - T''(v, l, J, e/f) \tag{2.66}$$

In the quantum mechanical formalism, it is preferred to use the double prime and prime to refer to the lower and upper ro-vibrational states corresponding to the molecular transition. In this thesis the same approach has been followed. For data analysis we have used the spectroscopic software SyMath (described in detail in chapter 3) developed by Dr. Georg Mellau at Justus Liebig University of Giessen, Germany. This is an interactive software running on a Mathematica platform that allows the user to find solutions for customized Hamiltonian operators and optimize the molecular parameters to fit the observed line positions for molecular transitions.

The effect of l-type resonances that appear in linear triatomic molecules has been taken into account by the software. The diagonal matrix elements for ro-vibrational term values are [58]:

$$T(v,l,J,e/f) = \langle v,l,J|H|v,l,J\rangle = G(v,l) + B_v[J(J+1) - l^2] - D_v[J(J+1) - l^2]^2 + H_v[J(J+1) - l^2]^3 \tag{2.67}$$

The off-diagonal matrix elements can be given as:

$$\langle v,l,J|H|v,l\pm 2,J\rangle = \frac{1}{4}\left\{q_v - q_{vJ}J(J+1) + q_{vJJ}J^2(J+1)^2 + q_l(l\pm 1)^2\right\} \times \{(v_2 \mp l)(v_2 \mp l + 2)[J(J+1) - l(l\pm 1)][J(J+1) - l(l\pm 1)(l\pm 2)]\}^{\frac{1}{2}} \tag{2.68}$$

and

$$\langle v,l,J|H|v,l\pm 4,J\rangle = \frac{\rho_v}{16}\{(v_2 \mp l)(v_2 \pm l + 2)(v_2 \mp l - 2)(v_2 \pm l + 4) \times [J(J+1) - l(l\pm 1)][J(J+1) - (l\pm 1)(l\pm 2)] \times [J(J+1) - (l\pm 2)(l\pm 3)] \times [J(J+1) - (l\pm 3)(l\pm 4)]\}^{\frac{1}{2}} \tag{2.69}$$

In the equations (2.67) to (2.69) the B_v, D_v and H_v are molecular constants discussed in section 2.2 and q_v, q_{vJ}, q_{vJJ}, q_l and ρ_v are the ro-vibrational constants for the correction of the l-type resonance of DCN molecule. As usual, J and v are the rotational and vibrational quantum numbers, respectively, and l is the vibrational angular momentum.

The vibrational energy levels measured relative to the ground energy levels, i.e.

$$G\_0\ (v,l) = G(v,l) - G(0,0) \tag{2.70}$$

are needed to calculate the values for band centers. The expression needed to calculate the band centers is given by the following equation:

$$\nu_c = G_c'(v,l) - G_c''(v,l) \tag{2.71}$$

in which $G_0(v,l)$ is expressed by:

$$G_c(v,l) = G_0(v,l) - B_v l^2 - D_v l^4 - H_v l^6 \tag{2.72}$$

We can obtain a simplified expression for the band center by substituting equation (2.72) in the equation (2.71). It follows that we have:

$$\nu_c = G_0'(v,l) - B_v' l'^2 - D_v' l'^4 - H_v' l'^6 - G_0''(v,l) + B_v'' l''^2 + D_v'' l''^4 + H_v'' l''^6 \tag{2.73}$$

in which the meaning of double prime and prime were discussed earlier.

The expression for $G(v, l)$ can be assigned by aggregate of the following eigenvalues and replaced in the Hamiltonian matrices [58]:

$$G(v,l) = \sum \omega_i (v_i + \tfrac{d_i}{2}) + \sum\sum x_{ij} \left(v_i + \tfrac{d_i}{2}\right)\left(v_j + \tfrac{d_j}{2}\right) + g_{22} l^2 + \sum\sum\sum y_{ijk} \left(v_i + \tfrac{d_i}{2}\right)\left(v_j + \tfrac{d_j}{2}\right)\left(v_k + \tfrac{d_k}{2}\right) + \sum y_{ill} \left(v_i + \tfrac{d_i}{2}\right) l^2 + \sum\sum\sum\sum z_{ijkh} \left(v_i + \tfrac{d_i}{2}\right)\left(v_j + \tfrac{d_j}{2}\right)\left(v_k + \tfrac{d_k}{2}\right)\left(v_h + \tfrac{d_h}{2}\right) + \sum\sum z_{ijll} \left(v_i + \tfrac{d_i}{2}\right)\left(v_j + \tfrac{d_j}{2}\right) l^2 + z_{llll} l^4 + z_{22222}(v_2 + 1)^5 + z_{222ll}(v_2 + 1) l^4 + z_{222ll}(v_2 + 1)^3 l^2 \tag{2.74}$$

In the above expression, term d is the degeneracy of energy levelsl.

To obtain the rotational constant B_v (see section 2.2.7. for an in-depth expression) similar expansion were derived and written by the following form:

$$B_v = B_e - \sum \alpha_i \left(v_i + \frac{d_i}{2}\right) + \sum\sum \gamma_{ij} \left(v_i + \frac{d_i}{2}\right)\left(v_j + \frac{d_j}{2}\right) + \gamma_{ll} l^2 + \sum\sum\sum \gamma_{ijk} \left(v_i + \frac{d_i}{2}\right)\left(v_j + \frac{d_j}{2}\right)\left(v_k + \frac{d_k}{2}\right) + \sum \gamma_{ill} \left(v_i + \frac{d_i}{2}\right) l^2 + \gamma_{2233} (v_2 + 1)^2 \left(v_3 + \frac{1}{2}\right)^2 + \gamma_{12ll} \left(v_1 + \frac{1}{2}\right)(v_2 + 1) l^2 + \gamma_{22ll} (v_2 + 1)^2 l^2 \quad (2.75)$$

where the constants $\alpha_i, \gamma_{ij}, \gamma_{ll}, \ldots$ are the ro-vibrational values for the correction of the higher terms. Likewise, the centrifugal distortion constant D_v (see 2.2.3.2 section) were computed using the following formula:

$$D_v = D_e - \sum \beta_i \left(v_i + \frac{d_i}{2}\right) + \beta_{ll} l^2 + \beta_{2ll} (v_2 + 1) l^2 \quad (2.76)$$

And H_v which is the correction term for centrifugal distortion (see 2.2.7. section) is supposed to be calculated as follow:

$$H_v = H_e + \sum \epsilon_i \left(v_i + \frac{d_i}{2}\right) + \epsilon_{ll} l^2 \quad (2.77)$$

The *l*-type resonance constant, q_v, and its higher order terms q_{vJ} and q_{vJJ} are given by the following equations:

$$q_v = q_e + \sum \pi_i \left(v_i + \frac{d_i}{2}\right) + \sum\sum \pi_i \left(v_i + \frac{d_i}{2}\right)\left(v_j + \frac{d_j}{2}\right) \quad (2.78)$$

and

$$q_{vJ} = q_{eJ} + \sum \pi_{iJ} \left(v_i + \frac{d_i}{2}\right) + \pi_{22J} (v_2 + 1)^2 \quad (2.79)$$

$$q_{vJJ} = q^*{}_{JJ} + \pi_{1JJ} \left(v_1 + \frac{1}{2}\right) + \pi_{2JJ} (v_2 + 1) \quad (2.80)$$

The equations mentioned in this section have been implemented into the SyMath software. The values for the power series constants given in the expressions above, such as $\pi_{1JJ}, \pi_i, \beta_{2ll}, \ldots$ and so on, were taken from Ref. [58] and considered as initial guesses to predict theoretically the line positions for DCN transitions. Using this method, the experimental line positions corresponding for each transition can be detected in the spectra. This procedure assists the user to fit the spectra using SyMath and determine all the ro-vibrational parameters. The SyMath software and its features will be discussed in more details in the next chapter.

3. Experimental Setups

3.1. Overview

To precisely describe different line shape models or to obtain fingerprint frequencies of various gasses, there is an essential need in advancement of the techniques to record reliable spectra. Better information is demanded to elaborately develop new line shape functions or to examine already proposed models to study the atmosphere of Earth or other planets.

This chapter will discuss the two experimental setups that have been used to record the spectra analyzed in this study. First, we present the description of tunable diode laser spectrometer (TDLS) located at the Department of Physics at the University of Lethbridge. The TDL spectrometer was used to record the spectra of acetylene pressurized by carbon dioxide over the different range of temperatures and pressures. Afterwards, the experimental setup that has been used to measure the spectral emission of DCN gas situated at the Justus Liebig University of Giessen, Germany will be given. Furthermore, the procedure and features of spectral fitting program called SyMath developed by Dr. Georg Mellau that has been applied to do the assignment of DCN gas will be described in details. Finally, a brief explanation about using the multispectrum non-linear least squares fitting technique for pure carbon monoxide and carbon monoxide broadened by hydrogen.

3.2. Tunable Diode Laser Spectrometer (TDLS)

3.2.1. Schematic of the 3-Channel TDLS

An overview of the TDLS located at the University of Lethbridge, Lethbridge, AB, composed of three channels is depicted in Fig. 3.1. Channel one contains the pressure and temperature controlled cell with 1.54 m (cell 1) fixed path length. The second channel (cell 2) consists of a room temperature reference cell having the same path length as the cell located on channel one. The reference cell is designed to work at pressures of a few Torr (less than 10 Torrs), while the gas cell in channel one can go up to hundreds of Torr. The third channel (D3) contains the detector that measures the background signal. The remaining components of this spectrometer are described in Fig.3.1 and presented below:

1. Vacuum pumps shown by thick black lines connected to the cell 1 and 2.

2. The NesLab ULT 80 thermal bath connected by blue lines to cell 1.

3. The gas sample.

4 & 5. The Fabry-Perot interferometer (needed to improve the wavelength measurement).

6. Pre-amps (needed to amplify the signal) of detectors and power supplies.

7. WA-1500 EXFO wavemeter (measures wavelengths of the incoming beams).

8. Tunable diode laser head (New Focus Veloctiy laser to produce the infrared light in the range of 6369 to 6666 cm^{-1})

9. TLB-6300 Velocity tunable laser controller (used to operate the tunable diode laser head. It can be done by sweeping the frequency modulation of the piezoelectric transducer (PZT) from -3 to +2.7 V which corresponds to the laser frequency within the range of -30 to +30 GHz).

10. MKS Baratron pressure gauges (used to measures the pressure of gas in cell 1 and 2).

Moreover, L1, L2, L3 are convergent lenses: M1, M2 are mirrors that re-direct the laser beam; D1, D2 D3 are detectors that measure the spectrum coming out from cell 1, 2 and the background of laser, respectively. C1, C2, C3, C4 are collimators whose function is to adjust the diameter of the light beam as needed. S1, S2, S3, S4 are optical beam splitters that can split the beam intensity into two different branches: 30% and 70%, depending on the application as shown in Fig.3.1 [92].

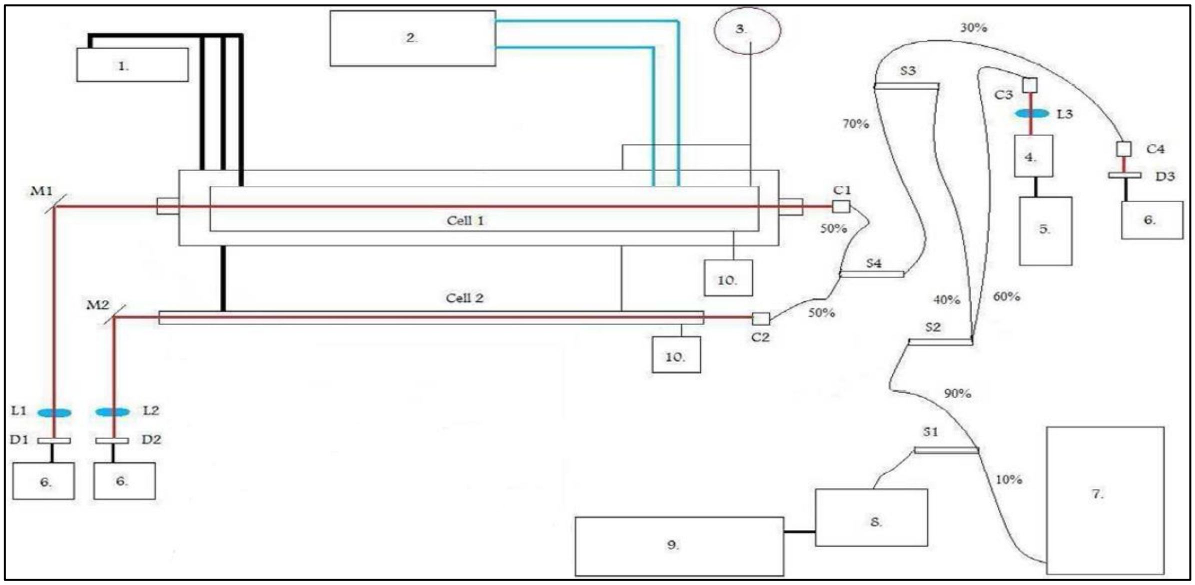

Figure 3.1. A general diagram of 3-channel TDL spectrometer located in our lab. A brief description regarding to different parts of this system is given above [8].

Fig.3.8. exhibits a recent photo of our laser system with all its optical components which all the parts are comparable with Fig.3.1.

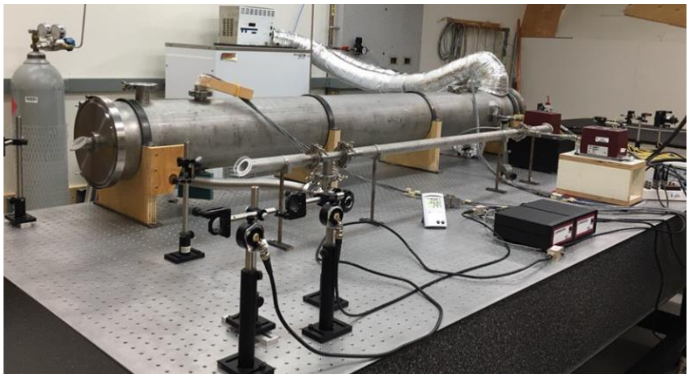

Figure 3.2. A recent photo of the tunable diode laser spectrometer located in our lab.

3.2.2. The Controlled Temperature and Pressure Gas Cell

Fig.3.2. represents a three dimensional view of the controlled temperature and pressure gas cell containing two cells, inner cell and outer cell. The inner cell is the absorption gas chamber of 1.54 m path length and 10.15 cm diameter. This cell is centered inside the outer cell, under vacuum conditions. The vacuum jacket minimizes the thermal losses to the environment and prevents ice from forming on the cell windows.

Several inlets and outlets have been located along both the inner and outer chambers as shown in Fig.3.2. Each end of the inner cell is manufactured to have inlet ports for temperature and pressure sensors as well as gas inlets and outlets. Five platinum resistor thermometers attached to the flange of inner cell are installed on rods at 15.25 cm, 45.70 cm and 76.2 cm locations. The layout of temperature sensors enables us to accurately monitor the temperature gradient along the length of chamber as depicted in Fig.3.3.

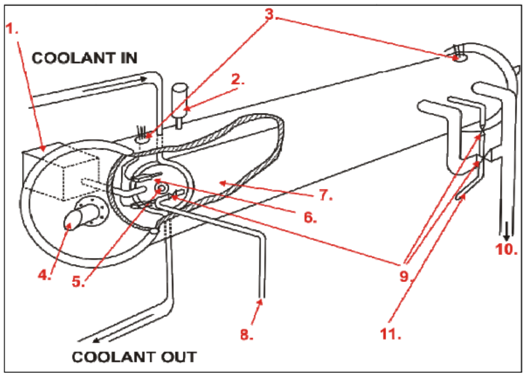

Figure 3.3. Three dimensional layout of the variable temperature pressure cell. 1. MKS Baratron pressure gauge 2. Enhanced pirani pressure gauge 3. Vacuum field throughs 4. CaF_2 windows mounted at Brewster angle 5. CaF_2 windows of the inner cell 6. Platinum resistor sensors. 7. Inner cell body 8. Gas inlet 9. Vacuum valves 10. Gas outlet 11. De-pressuring port for the vacuum jacket [8].

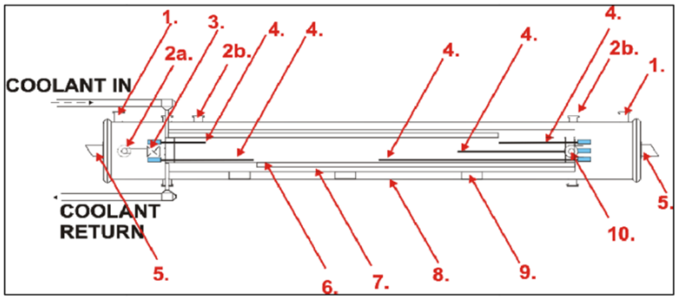

Figure 3.4. Side view of above variable temperature pressure cell figure. 1. Vacuum port 2a. Gas inlet 2b. Vacuum field-through for platinum resistor thermometers 3. Vacuum valve 4. Platinum temperature sensors 5. CaF_2 windows installed at Brewster angle 6. Designed fins for conducting the coolant fluid within the inner cell 7. Coolant jacket 8. Outer chamber body 9. Cell base support 10. De-pressuring valve for of the outer chamber [8].

The outer chamber is equipped with two removable flanges, sealed to the cell with viton O-rings. This provides access to the thermocouples, gas valves as well as to the inlet and outlet for the coolant fluid circulated by the NesLab ULT-80 unit. Four CaF_2 windows have been mounted the ends of the chambers. The windows on the outer cell were positioned at Brewster angle. The Brewster angle or polarization angle is the angle at which the incident beam is completely transmitted via the surface without reflection [8]. Figs.3.2. and 3.3. [8] present the components of the controlled temperature and pressure gas cell.

3.2.3. The NesLab ULT-80 bath circulation

The Thermo Neslab ULT-80 bath circulator [104] has the ability to cool down or heat up the reservoir from -80 to +80 $^{\circ}$C with a temperature stability of ± 0.03°C. This unit is being used in our lab to control the temperature of the sample in the gas cell 1. Methanol or ethanol have been used as coolant in the thermal bath of the chiller. The entire inner chamber body is in contact with the coolant fluid circulated by the unit around the cell body. Using methanol and ethanol only allow us to adjust the temperature to maximum +60 $^{\circ}$C and +75 $^{\circ}$C due to the fact that the boiling points of methanol and ethanol are about +64 $^{\circ}$C and +78 $^{\circ}$C, respectively.

Additionally, a small temperature gradient along the chamber is observed if the temperature is set to higher than +60 $^{\circ}$C due to the thermal lost to the environment. [105].

Monitoring the NesLab ULT-80 can be done either manually through the front panel mounted on the chiller or remotely through the communication software called NEScom 4.0. This software allows the user to control the chiller settings and monitor its performance. The configuration COM port connects the chiller to the computer using the following protocol: a RS-232 communication cable, and a NC protocol: 9600 Baud, 8 data bits, 1 stop bit, no parity [106]. Fig.3.4. is an example of NEScom 4.0 windows as well as the digital virtual panel. Panel (a) shows the first window of the NEScom software that communicates with the NesLab ULT-80 unit. After the connection is established, the color of the icon will convert to green implying that the connection is confirmed and ready to be used (Fig.3.4.(b)). A virtual displaying function just like the one is mounted on the chiller will allow the user to adjust the settings on the chiller (Fig.3.4. (c)).

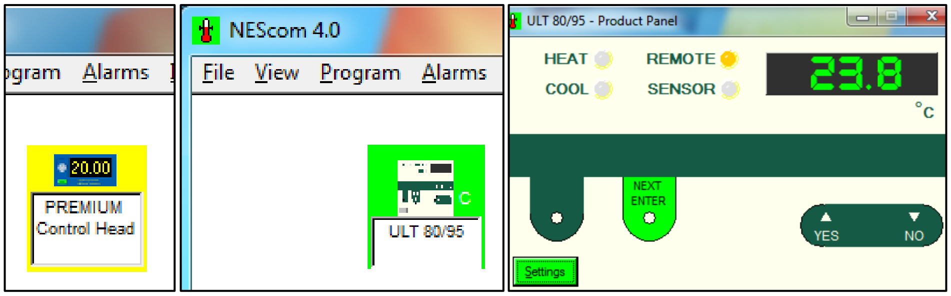

(a) (b) (c)

Figure 3.5. Three different panels of the NEScom 4.0 program from the start time until the virtual display setting window appears.

3.2.4. Resistance Thermometer Detectors

The measurement principle behind all resistance thermometer detectors (RTDs) is the change in resistance of the wire as the temperature fluctuates. Platinum resistance thermometer detectors (PRTDs) are type of sensitive temperature sensors used widely to accurately measure temperature.

A variety of PRTDs have been designed depending on their applications, such as thin film PRT, wire wound PRT, coil element PRT [107]. In our lab, wire wound PRTs have been used to monitor the temperature at different depths inside the main cell as shown in Fig.3.3. For this type of detector the relation between the variation in temperature and resistance is fairly linear. PT100 is the most common type among all of the PRTDs. This type has a resistance of 138.4 Ohms (Ω) and 100 ohms (Ω) at 100 °C and at 0 °C, respectively, and the resistance typically can shift by almost 0.4 Ohms per degree Celsius [108]. PRTDs can cover a wide range of temperature from -200 °C to +1000 °C with significant accuracy. The schematic diagram of a platinum resistance temperature detector is plotted in Fig.3.5.

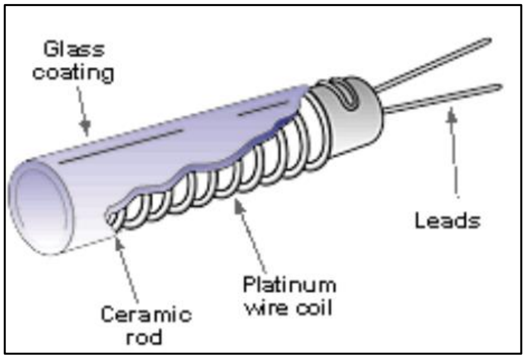

Figure 3.6. Three dimensional view of the wire wound PRT [109].

All five thermometers have been connected via a four-lead connection technique to the multi-channel Lakeshore 218 temperature controller unit to display and monitor the temperature using LabVIEW. The four-lead connection technique uses a Wheatstone bridge to remove the influence of lead resistance on temperature.

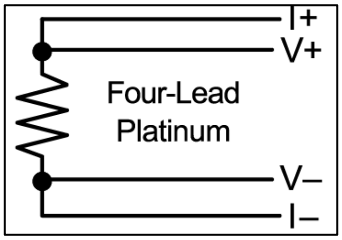

Figure 3.7. Four-lead connection layout [110].

3.2.5. Laser and Light Detection System

A tunable diode laser head operating in the range of 1500 to 1570 nm wavelength connected to a New Focus 6300 Velocity tunable laser controller was used to scan the 1500 to 1640 nm spectral range. Three Indium Gallium Arsenide (InGaAs) photodiode detectors running at room temperature connected to preamplifiers and power control boxes were used to detect the optical signals passed through the gas cells on channels 1&2 and the laser background on channel 3. A combination of Thorlabs SA200-14A

Fabry Perot interferometer with a free spectral range (FSR) of 1.5 GHz (0.05cm^{-1}) and a wavemeter WA-1500 EXFO allowed us to accurately calibrate the absorption spectra. All devices were connected to a PC computer using a general purpose interface bus (GPIB) communication port shown in Fig.3.7. [92] (violet lines), serial RS-232 connections (green lines), a NI-DAQ card (red lines) and custom designed multifunctional pin cables (black lines).

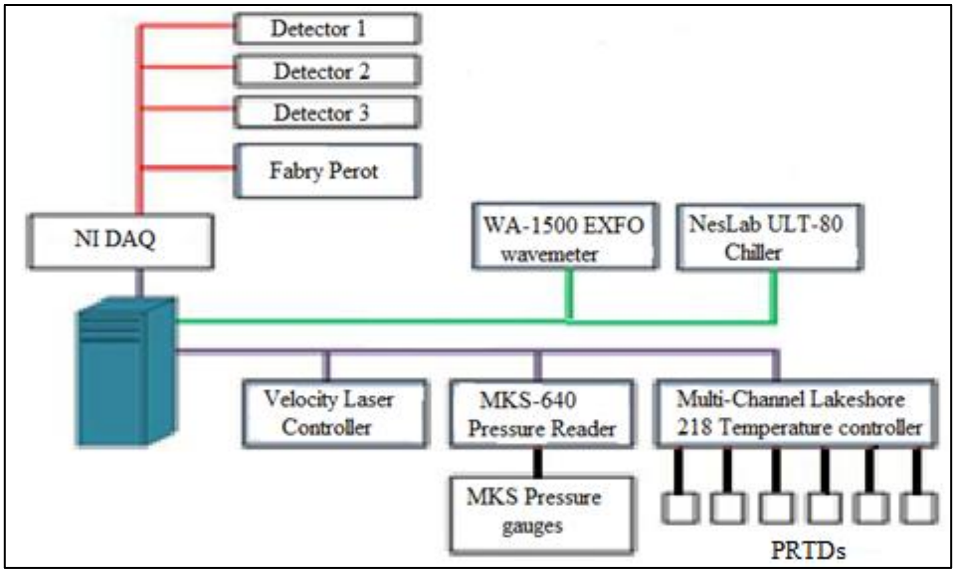

Figure 3.8. Schematic diagram of cable connections between all instruments and the TDL spectrometer.

Software written in Labview was used to monitor and control the laser system. The scanning of the laser occurs when the central frequency of the laser is set on the wavelength corresponding to the transition of interest. At that time the NI-DAQ card starts sending signals to the piezoelectric device assembled inside the laser controller to ramp the voltage from -3 to 2.7 V with increments of 0.001 V allowing the system to perform at high resolution. All optical components as well as the absorption cells were mounted on a Kinetic Systems 5100H series optical table to isolate the spectrometer from any mechanical vibration noise [8].

3.2.6. Data Processing

To create the transmission files and start analyzing them, the raw data must be processed carefully. To accomplish this task, the data has to be calibrated using information from the wavemeter and Fabry Perot interferometer (see 4.4.2. section of ref [8]). The first resonance peak of the FP (Fabry Perot interfrometer) is detected by the wavemeter. The remaining peaks locations can be found using the characteristic of the current FP (the distance between each successive peak is 0.05 cm^{-1}). The resolution of the spectra from 3 channels (channel 1, 2 and background) was estimated by dividing the number of data points between each successive resonance to 0.05 cm^{-1}. This way, we can assign the wavenumber of each signal.

The baseline of spectra recorded by channel 1&2 (CH1&2) must be compared to those of measured as signal of background (BG) by channel 3 (CH3). Fig.3.9 depicts the 4 steps need to create the transmission files. It is obvious from Fig.3.9 (a) that due to the power difference in laser intensity, CH1 and CH3 have different signals (red belongs to the CH3 and starts at -9 while white belongs to CH1 and starts at -10). One of the reason as shown in Fig 3.1. is the usage of fiber optic splitter in the experiment. To account for this effect, first the spectral features (any absorption) of CH1 (or CH2) should be subtracted with the CH3 using the following process [39]:

$$Resdiual = Channel\ 1\ baseline\ (and\ 2) - Channel\ 3\ background \tag{3.1}$$

Afterwards, the residual will be fitted with the appropriate degree of Chebyshev polynomial approximation using the following equation:

$$Cheb\ Poly + \ Channel\ 3\ background = Corrected\ baseline \tag{3.2}$$

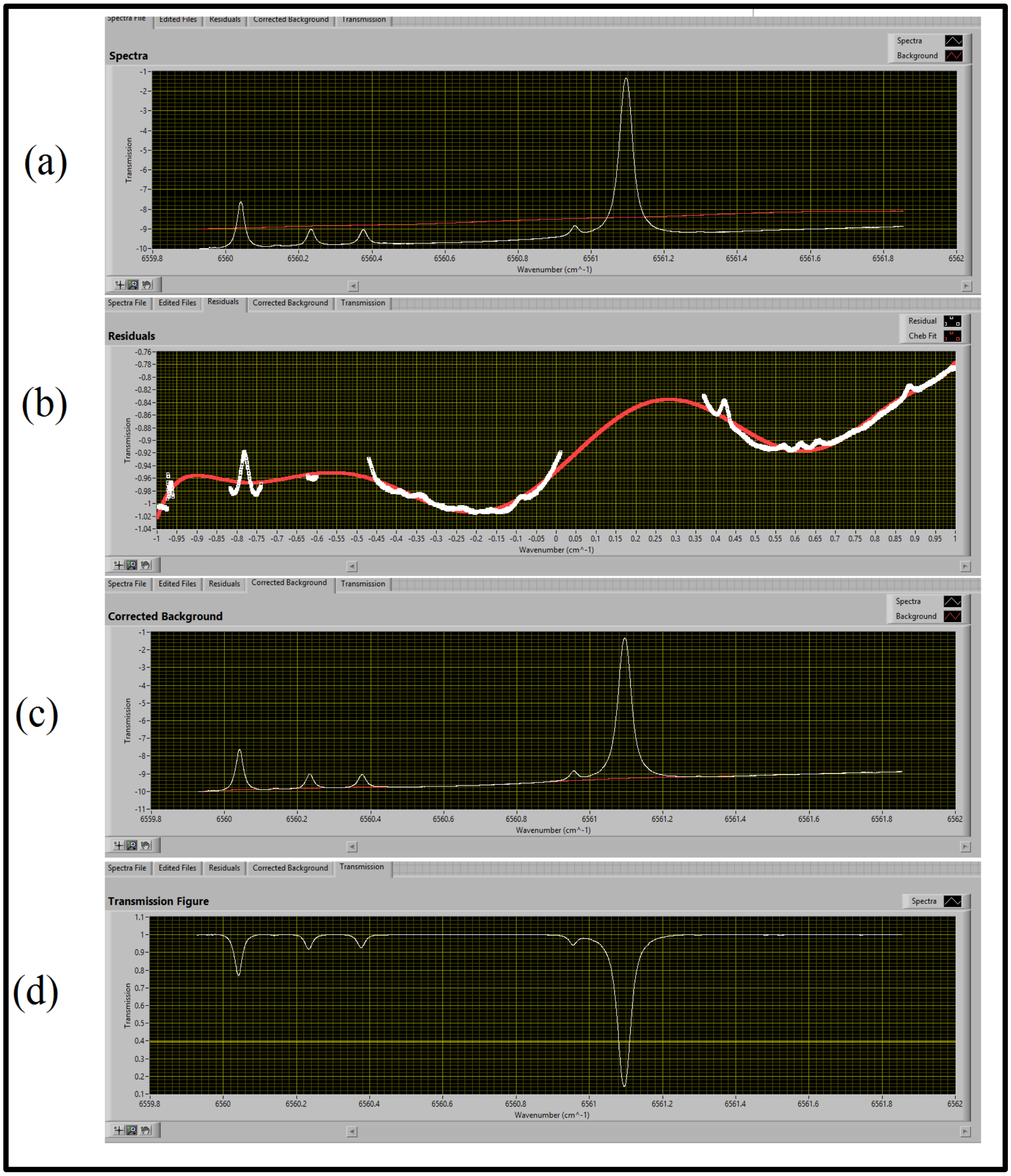

Figure 3.9. Front panel LabVIEW for creating the transmission file. This spectrum belongs to the R1 at pressure 50 Torr and temperature 296 K. (a) Red line belongs to the channel 3 background of laser (BG), white line belongs to the line R1 absorption. (b) This panel represents the residual by subtracting the channel 1 from channel 3 (see equation 3.1) (c) This panel displays the residual fitted by Chebyshev polynomial to best order (here 10th order), then obtaining the corrected base line using equation (3.2). (d) This panel depicts the transmission file.

Fig.3.9 (b) depicts the residual is fitted by the Chebyshev polynomials (appropriate degree is needed to be found) and the wavenumber scale, however, must be converted to the polynomial interpolation between [-1, 1]. Fig.3.9 (c) displays the spectra of CH1 (or CH2) while fitting for the Chebyshev polynomial to allow the user to compare the overlap of trace for CH1 (or CH2) with CH3 while having the converted wavenumber scale. Finally, with this corrected baseline we are then able to divide the signal corresponding to channel 1 or 2 spectra by the background to get a transmission spectral file, as shown in Fig.3.9 (d).

3.3. High Resolution Fourier Transform Spectrometer

The emission spectra of DCN were recorded using the Bruker IFS 120 HR Fourier transform spectrometer located at the Justus Liebig University, Giessen, Germany. In this section we present a summary of this experimental setup and its components. A custom chamber made of a quartz tube with length of one meter and diameter of 5 cm was used as an emission cell.

Potassium Bromide (KBr) windows sealed with Viton O-rings have been mounted on each end of this cell. Moreover, windows were kept at room temperature during the experiment using a water cooling circulation unit. The quartz gas cell was mounted inside an electrical commercial furnace (RoK/A 6/60, Heraeus, Hanau) used to heat the cell up to 1500 K. A Ge:Cu photodiode detector cooled with liquid-helium was used in the measurements. An entrance cavity was designed and manufactured to optimize the alignment by focusing the spectral radiation to the input port of the interferometer via transfer optics that were evacuated. In addition, an adjustable iris port kept at room temperature was installed at the rear of the exit window to narrow the radiative field of view. Furthermore, a He-Ne laser system was applied to enable the user to accurately align the path of light via a sets of optical components in order to transfer the emitted radiation along the optical axis of the interferometer.

To prevent the interaction between the emitted spectra and trace gasses in the ambient air, such as water or carbon dioxide, the transfer optics chamber located between the cell and the detector was constantly evacuated.

The emitted spectra were affected by black body background radiation emitted by the hot cell. This extra radiation added to the data had to be removed, and this can be accomplished by subtracting of the data recorded with the heated, empty cell is empty. Additionally, using various interference bandpass filters mounted in front of the detector allows us to limit the unwanted black body radiation. In this way, an S/N of 3000:1 to 10000:1 can be obtained depending on the intensities of lines. A view of the diagram of the Bruker IFS 120 HR Fourier transform spectrometer is depicted on Fig.3.9 [94].

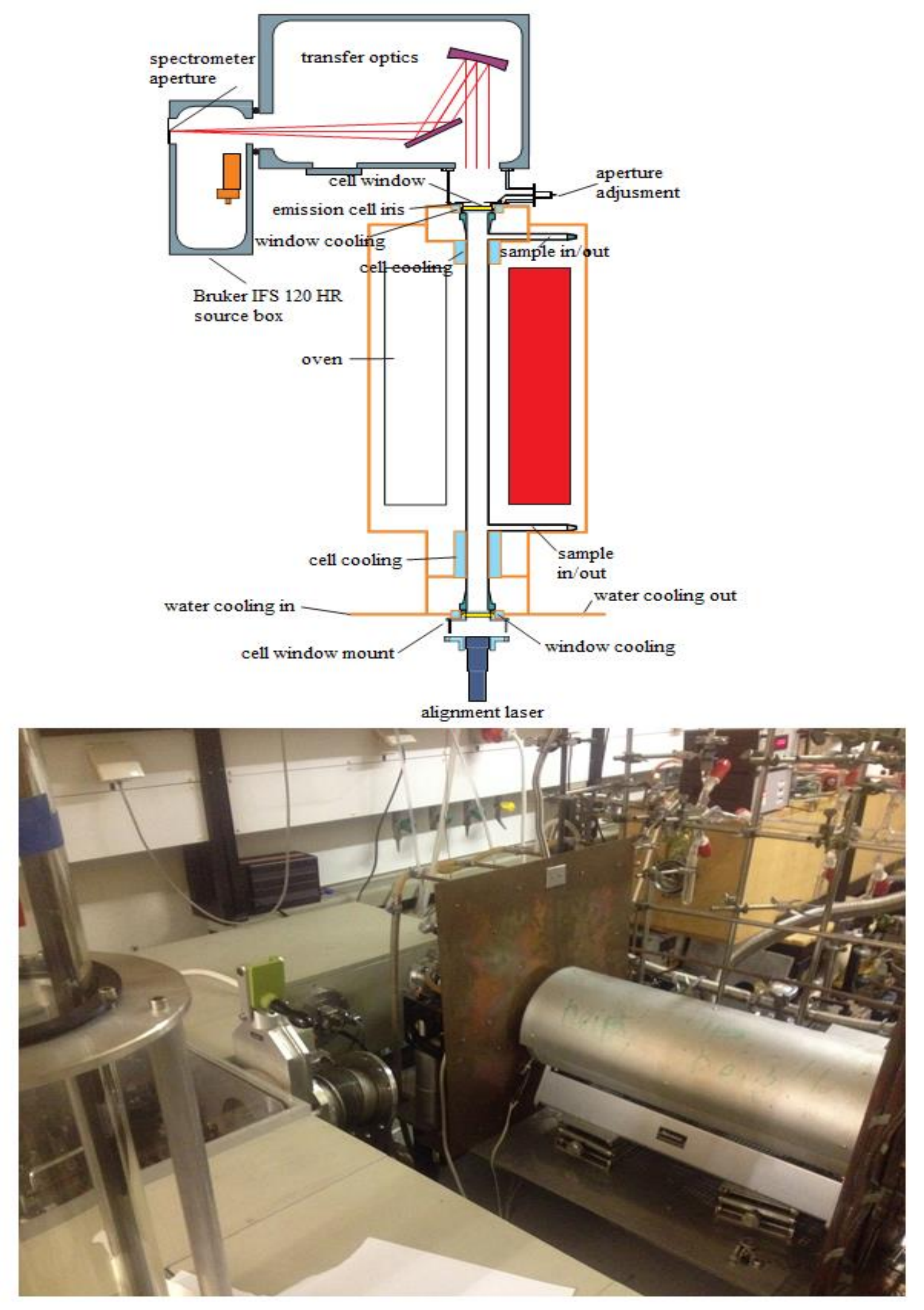

Figure 3.10. Two dimensional and photo views of the Infrared Fourier Spectrometer. A comparison can be made by going from the bottom to the top of the two dimensional layout and from the right to the left of the real image (taken from [94]).

3.4. SyMath

To carry out the data analysis we used the SyMath software developed by Dr. Georg Mellau written in Mathematica. This user friendly spectroscopic analysis software provides features needed to accurately obtain the line positions and intensities of any gas. However, since every molecule has its own properties and reacts differently depending on its mass, structure, and polarity, the theoretical calculations must be performed for different gasses in Mathematica algebraic language and then imported to SyMath. In our study, the theoretical calculations needed to predict the spectrum of DCN and HCN were implemented in this software. SyMath is composed of two main components named "Mole file" (needed for every trace gas present in the spectrum), "Pek file" needed to undertake the theoretical and experimental tasks of the study. To link between these two components, the user has to create a "Band search" window. In this section, different parts of this software and the method used to do the assignment of DCN gas will be discussed in details.

3.4.1. The "Molecule" Menu

The "Mole File" known also as the "Molecule Window" includes all the molecular parameters needed to predict the motion of the molecule in order to acquire the ro-vibrational parameters. An overview of the top part of this window is shown in Fig.3.11.

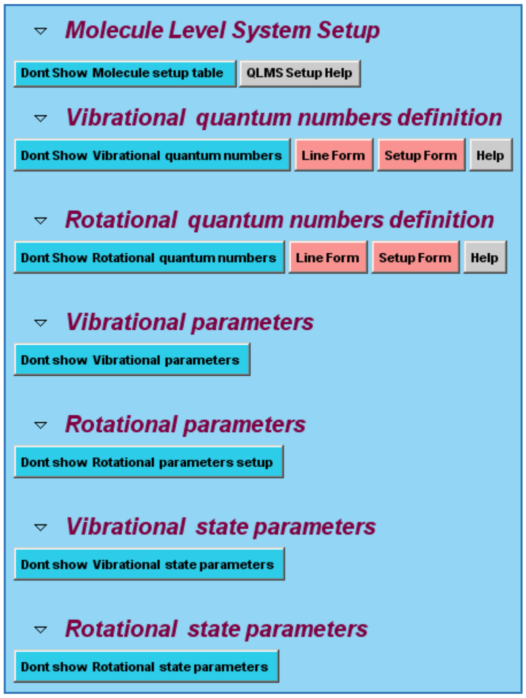

Figure 3.11. View of the molecule window of the SyMath software.

The users of SyMath can load information on the physical state of the molecule, such as its molecular mass, abundance, orbital identity and point group. By clicking on the buttons available in the “Molecule Window” the user can switch to a new window that allows modifications in the entered parameters. Moreover, a list of all possible atoms available in the periodic table is available to the users.

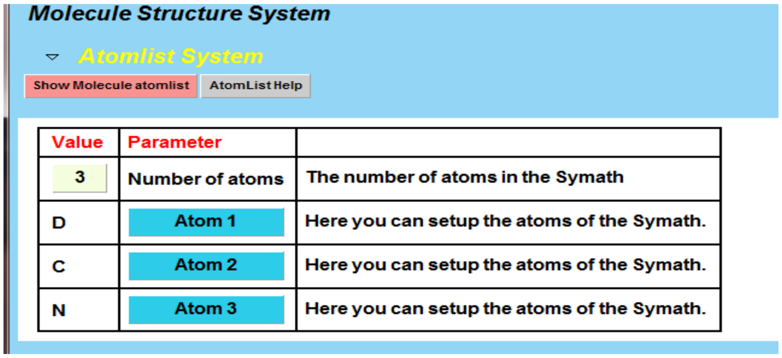

Value	Parameter	
3	Number of atoms	The number of atoms in the Symath
D	Atom 1	Here you can setup the atoms of the Symath.
C	Atom 2	Here you can setup the atoms of the Symath.
N	Atom 3	Here you can setup the atoms of the Symath.

Figure 3.12. View of the molecule structure system option.

Users can use the “Vibrational quantum numbers definition” feature to modify the selection rules regarding the molecule of interest. The vibrational quantum number, angular momentum, their notations, the degeneracy of energy levels and the type of vibrational mode, are all defined in this section. Similarly, the “Rotational quantum numbers definition” feature allows the user to select the rotational quantum numbers as well as to determine the P-, Q- and R- branches. Moreover, the user can set the threshold level beyond which the spectrum is considered to be at noise level.

The “Vibrational Parameters” and “Rotational Parameters” menu options contain all the power series constants from equations (2.74) to (2.80). These constants can be obtained either experimentally or theoretically. However, SyMath does have the ability to calculate these power series constants experimentally. Thus, to speed-up the DCN assignment study presented here, all of the constants were taken from Ref [58]. Fig.3.12 represents a schematic view of the Vibrational and Rotational Parameters features in the “Molecule” Window of SyMath.

The equations (2.67) to (2.69) have to be linked with the “Vibrational State Parameters” and “Rotational State Parameters”, features in the Symath menu. In this way, SyMath can retrieve all the ro-vibrational parameters including B_v, D_v, H_v, q_v, q_{vJ}, q_{vJJ}, q_l and ρ_v in addition to the vibrational energy levels, $G(v, l)$.

The “Vibrational States List” option equips the user by having access to all the ro-vibrational parameters as well as to the vibrational energy levels mentioned in the previous section. Additionally, one can make necessary changes by switching on the “Edit” button, and recalculating the optimized parameters.

(a)

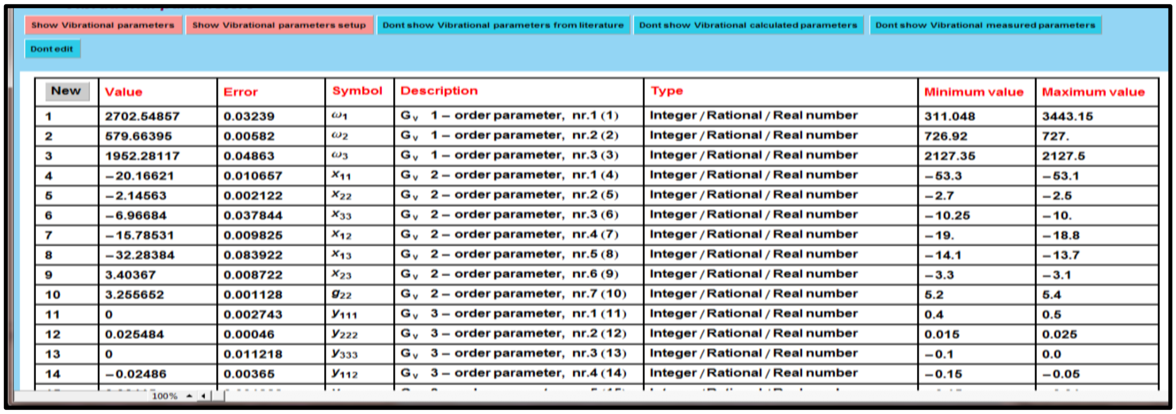

New	Value	Error	Symbol	Description	Type	Minimum value	Maximum value
1	2702.54857	0.03239	ω_1	G_v 1 − order parameter, nr.1 (1)	Integer / Rational / Real number	311.048	3443.15
2	579.66395	0.00582	ω_2	G_v 1 − order parameter, nr.2 (2)	Integer / Rational / Real number	726.92	727.
3	1952.28117	0.04863	ω_3	G_v 1 − order parameter, nr.3 (3)	Integer / Rational / Real number	2127.35	2127.5
4	−20.16621	0.010657	x_{11}	G_v 2 − order parameter, nr.1 (4)	Integer / Rational / Real number	−53.3	−53.1
5	−2.14563	0.002122	x_{22}	G_v 2 − order parameter, nr.2 (5)	Integer / Rational / Real number	−2.7	−2.5
6	−6.96684	0.037844	x_{33}	G_v 2 − order parameter, nr.3 (6)	Integer / Rational / Real number	−10.25	−10.
7	−15.78531	0.009825	x_{12}	G_v 2 − order parameter, nr.4 (7)	Integer / Rational / Real number	−19.	−18.8
8	−32.28384	0.083922	x_{13}	G_v 2 − order parameter, nr.5 (8)	Integer / Rational / Real number	−14.1	−13.7
9	3.40367	0.008722	x_{23}	G_v 2 − order parameter, nr.6 (9)	Integer / Rational / Real number	−3.3	−3.1
10	3.255652	0.001128	g_{22}	G_v 2 − order parameter, nr.7 (10)	Integer / Rational / Real number	5.2	5.4
11	0	0.002743	y_{111}	G_v 3 − order parameter, nr.1 (11)	Integer / Rational / Real number	0.4	0.5
12	0.025484	0.00046	y_{222}	G_v 3 − order parameter, nr.2 (12)	Integer / Rational / Real number	0.015	0.025
13	0	0.011218	y_{333}	G_v 3 − order parameter, nr.3 (13)	Integer / Rational / Real number	−0.1	0.0
14	−0.02486	0.00365	y_{112}	G_v 3 − order parameter, nr.4 (14)	Integer / Rational / Real number	−0.15	−0.05

(b)

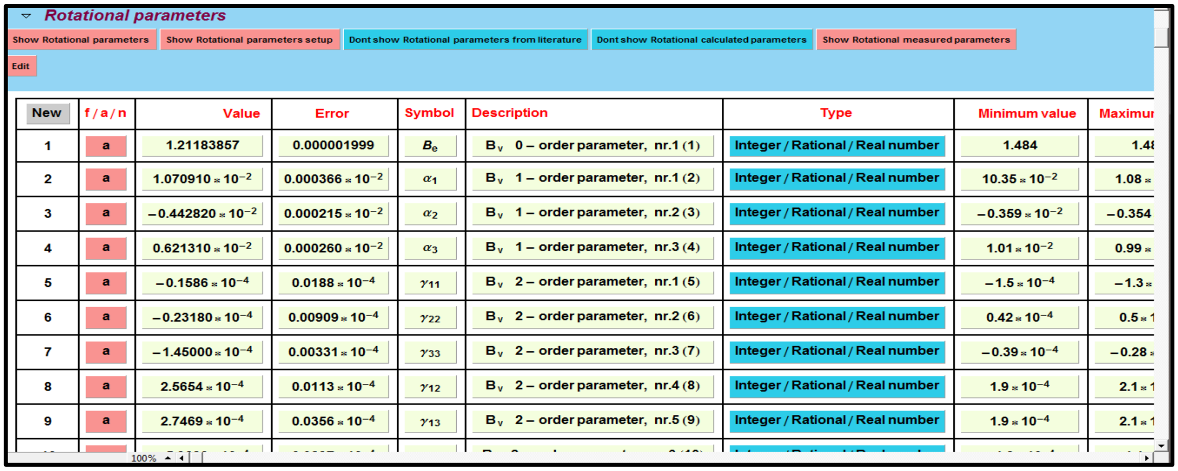

New	f / a / n	Value	Error	Symbol	Description	Type	Minimum value	Maximur
1	a	1.21183857	0.000001999	B_e	B_v 0 − order parameter, nr.1 (1)	Integer / Rational / Real number	1.484	1.48
2	a	1.070910×10^{-2}	0.000366×10^{-2}	α_1	B_v 1 − order parameter, nr.1 (2)	Integer / Rational / Real number	10.35×10^{-2}	1.08 ×
3	a	-0.442820×10^{-2}	0.000215×10^{-2}	α_2	B_v 1 − order parameter, nr.2 (3)	Integer / Rational / Real number	-0.359×10^{-2}	−0.354
4	a	0.621310×10^{-2}	0.000260×10^{-2}	α_3	B_v 1 − order parameter, nr.3 (4)	Integer / Rational / Real number	1.01×10^{-2}	0.99 ×
5	a	-0.1586×10^{-4}	0.0188×10^{-4}	γ_{11}	B_v 2 − order parameter, nr.1 (5)	Integer / Rational / Real number	-1.5×10^{-4}	−1.3 ×
6	a	-0.23180×10^{-4}	0.00909×10^{-4}	γ_{22}	B_v 2 − order parameter, nr.2 (6)	Integer / Rational / Real number	0.42×10^{-4}	0.5 × 1
7	a	-1.45000×10^{-4}	0.00331×10^{-4}	γ_{33}	B_v 2 − order parameter, nr.3 (7)	Integer / Rational / Real number	-0.39×10^{-4}	−0.28 ×
8	a	2.5654×10^{-4}	0.0113×10^{-4}	γ_{12}	B_v 2 − order parameter, nr.4 (8)	Integer / Rational / Real number	1.9×10^{-4}	2.1 × 1
9	a	2.7469×10^{-4}	0.0356×10^{-4}	γ_{13}	B_v 2 − order parameter, nr.5 (9)	Integer / Rational / Real number	1.9×10^{-4}	2.1 × 1

Figure 3.13. (a) The “Vibrational Parameters” menu in SyMath; (b) The “Rotational Parameters” menu in SyMath.

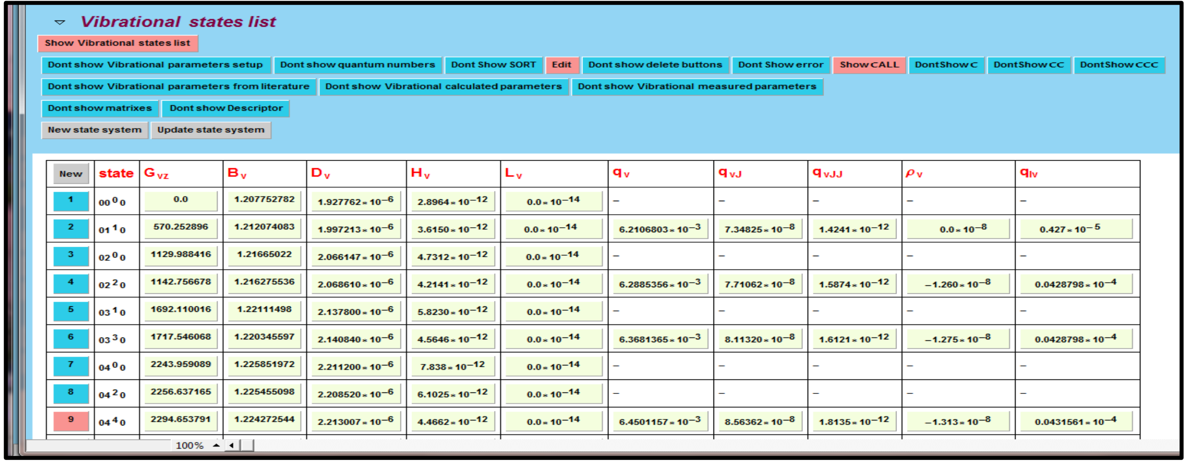

New	state	G_{vz}	B_v	D_v	H_v	L_v	q_v	q_{vJ}	q_{vJJ}	ρ_v	q_{lv}
1	$00^0 0$	0.0	1.207752782	1.927762×10^{-6}	2.8964×10^{-12}	0.0×10^{-14}	–	–	–	–	–
2	$01^1 0$	570.252896	1.212074083	1.997213×10^{-6}	3.6150×10^{-12}	0.0×10^{-14}	6.2106803×10^{-3}	7.34825×10^{-8}	1.4241×10^{-12}	0.0×10^{-8}	0.427×10^{-5}
3	$02^0 0$	1129.988416	1.21665022	2.066147×10^{-6}	4.7312×10^{-12}	0.0×10^{-14}	–	–	–	–	–
4	$02^2 0$	1142.756678	1.216275536	2.068610×10^{-6}	4.2141×10^{-12}	0.0×10^{-14}	6.2885356×10^{-3}	7.71062×10^{-8}	1.5874×10^{-12}	-1.260×10^{-8}	0.0428798×10^{-4}
5	$03^1 0$	1692.110016	1.22111498	2.137800×10^{-6}	5.8230×10^{-12}	0.0×10^{-14}	–	–	–	–	–
6	$03^3 0$	1717.546068	1.220345597	2.140840×10^{-6}	4.5646×10^{-12}	0.0×10^{-14}	6.3681365×10^{-3}	8.11320×10^{-8}	1.6121×10^{-12}	-1.275×10^{-8}	0.0428798×10^{-4}
7	$04^0 0$	2243.959089	1.225851972	2.211200×10^{-6}	7.838×10^{-12}	0.0×10^{-14}	–	–	–	–	–
8	$04^2 0$	2256.637165	1.225455098	2.208520×10^{-6}	6.1025×10^{-12}	0.0×10^{-14}	–	–	–	–	–
9	$04^4 0$	2294.653791	1.224272544	2.213007×10^{-6}	4.4662×10^{-12}	0.0×10^{-14}	6.4501157×10^{-3}	8.56362×10^{-8}	1.8135×10^{-12}	-1.313×10^{-8}	0.0431561×10^{-4}

Figure 3.14. View of “Rotational and Vibrational States List” window. State number nine of “Vibrational States List” is only on.

Based on the selection rules, the user can determine how many states are involved in the on-going assignment tasks, and can confirm that those states are included in the fit. On the other hand, the “Rotational States List” feature gives the user access to the energy levels for each transition via the “E_{JZ}” button.

The “Vibrational Transitions” feature combines all the spectroscopic information regarding individual molecular states. Consequently, it is possible for the user to select only the vibrational states that contain transitions of interest. Similarly, the “Rotational Transitions” option contains all the rotational transitions associated with a vibrational state. Moreover, the list of rotational transitions contains all the possible transitions or can be limited to any of the P-, Q- or R-branches to enable a faster parameter fit. All the equations related to the diagonal and off-diagonal matrix elements for ro-vibrational term values must be set-up in this section. If the user requires to add more matrix elements into this system, it can be performed by using the “New” button.

3.4.2. The “Band Search” menu

The “Band search” window contains all the necessary information regarding a vibrational band of interest, such as all possible transitions as well as their line positions and intensities, a plot window and a computation section for calculating the required parameters. One of the most important features of this section in SyMath is the plot window. The plot window allows the user to fit wide features in the emission spectrum based upon the theoretical assignments and guesses on how many lines may be underneath a spectral profile. Additional options available to the user are: using different colors for various line contours in the plot window, switching off/on for some options, zoom in/out, an add/delete for the list of transitions within the plot area of the selected band and so on. Fig.3.13 is a screen shot of the list of transitions in the band search window.

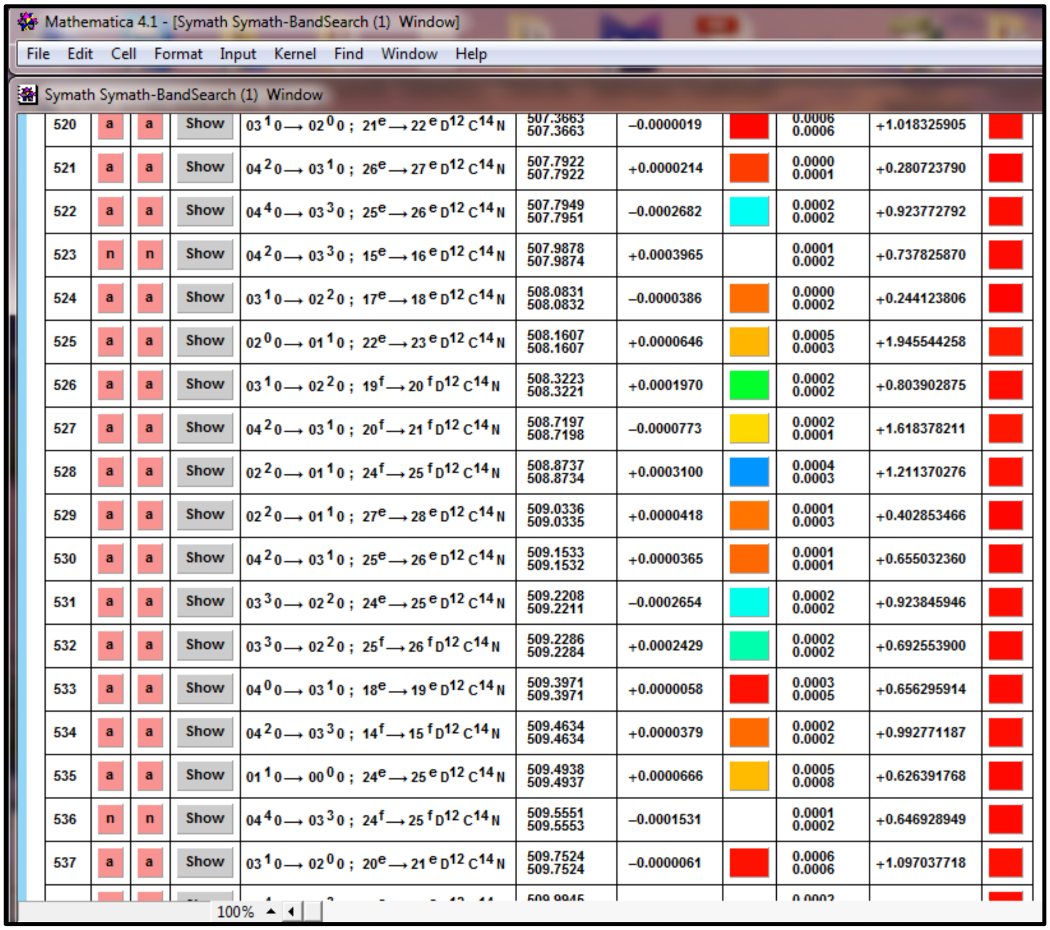

520	a	a	Show	$03^{1}0 \longrightarrow 02^{0}0\ ;\ 21^{e} \longrightarrow 22^{e}\ D^{12}C^{14}N$	507.3663 507.3663	–0.0000019	🟥	0.0006 0.0006	+1.018325905	🟥
521	a	a	Show	$04^{2}0 \longrightarrow 03^{1}0\ ;\ 26^{e} \longrightarrow 27^{e}\ D^{12}C^{14}N$	507.7922 507.7922	+0.0000214	🟧	0.0000 0.0001	+0.280723790	🟥
522	a	a	Show	$04^{4}0 \longrightarrow 03^{3}0\ ;\ 25^{e} \longrightarrow 26^{e}\ D^{12}C^{14}N$	507.7949 507.7951	–0.0002682	🟦	0.0002 0.0002	+0.923772792	🟥
523	n	n	Show	$04^{2}0 \longrightarrow 03^{3}0\ ;\ 15^{e} \longrightarrow 16^{e}\ D^{12}C^{14}N$	507.9878 507.9874	+0.0003965		0.0001 0.0002	+0.737825870	🟥
524	a	a	Show	$03^{1}0 \longrightarrow 02^{2}0\ ;\ 17^{e} \longrightarrow 18^{e}\ D^{12}C^{14}N$	508.0831 508.0832	–0.0000386	🟧	0.0000 0.0002	+0.244123806	🟥
525	a	a	Show	$02^{0}0 \longrightarrow 01^{1}0\ ;\ 22^{e} \longrightarrow 23^{e}\ D^{12}C^{14}N$	508.1607 508.1607	+0.0000646	🟨	0.0005 0.0003	+1.945544258	🟥
526	a	a	Show	$03^{1}0 \longrightarrow 02^{2}0\ ;\ 19^{f} \longrightarrow 20^{f}\ D^{12}C^{14}N$	508.3223 508.3221	+0.0001970	🟩	0.0002 0.0002	+0.803902875	🟥
527	a	a	Show	$04^{2}0 \longrightarrow 03^{1}0\ ;\ 20^{f} \longrightarrow 21^{f}\ D^{12}C^{14}N$	508.7197 508.7198	–0.0000773	🟨	0.0002 0.0001	+1.618378211	🟥
528	a	a	Show	$02^{2}0 \longrightarrow 01^{1}0\ ;\ 24^{f} \longrightarrow 25^{f}\ D^{12}C^{14}N$	508.8737 508.8734	+0.0003100	🟦	0.0004 0.0003	+1.211370276	🟥
529	a	a	Show	$02^{2}0 \longrightarrow 01^{1}0\ ;\ 27^{e} \longrightarrow 28^{e}\ D^{12}C^{14}N$	509.0336 509.0335	+0.0000418	🟧	0.0001 0.0003	+0.402853466	🟥
530	a	a	Show	$04^{2}0 \longrightarrow 03^{1}0\ ;\ 25^{e} \longrightarrow 26^{e}\ D^{12}C^{14}N$	509.1533 509.1532	+0.0000365	🟧	0.0001 0.0001	+0.655032360	🟥
531	a	a	Show	$03^{3}0 \longrightarrow 02^{2}0\ ;\ 24^{e} \longrightarrow 25^{e}\ D^{12}C^{14}N$	509.2208 509.2211	–0.0002654	🟦	0.0002 0.0002	+0.923845946	🟥
532	a	a	Show	$03^{3}0 \longrightarrow 02^{2}0\ ;\ 25^{f} \longrightarrow 26^{f}\ D^{12}C^{14}N$	509.2286 509.2284	+0.0002429	🟩	0.0002 0.0002	+0.692553900	🟥
533	a	a	Show	$04^{0}0 \longrightarrow 03^{1}0\ ;\ 18^{e} \longrightarrow 19^{e}\ D^{12}C^{14}N$	509.3971 509.3971	+0.0000058	🟥	0.0003 0.0005	+0.656295914	🟥
534	a	a	Show	$04^{2}0 \longrightarrow 03^{3}0\ ;\ 14^{f} \longrightarrow 15^{f}\ D^{12}C^{14}N$	509.4634 509.4634	+0.0000379	🟧	0.0002 0.0002	+0.992771187	🟥
535	a	a	Show	$01^{1}0 \longrightarrow 00^{0}0\ ;\ 24^{e} \longrightarrow 25^{e}\ D^{12}C^{14}N$	509.4938 509.4937	+0.0000666	🟨	0.0005 0.0008	+0.626391768	🟥
536	n	n	Show	$04^{4}0 \longrightarrow 03^{3}0\ ;\ 24^{f} \longrightarrow 25^{f}\ D^{12}C^{14}N$	509.5551 509.5553	–0.0001531		0.0001 0.0002	+0.646928949	🟥
537	a	a	Show	$03^{1}0 \longrightarrow 02^{0}0\ ;\ 20^{e} \longrightarrow 21^{e}\ D^{12}C^{14}N$	509.7524 509.7524	–0.0000061	🟥	0.0006 0.0006	+1.097037718	🟥

Figure 3.15. View of transition list in the band search window, showing the differences between experimental and theoretical line positions.

3.5. LabFit

The analysis of spectral absorption of the acetylene diluted by carbon dioxide was carried out using the multispectrum non-linear least squares fitting technique developed by Dr. Chris Benner *et al*. [100]. Employing this software provides the user with many advantages to accurately determine the spectral parameters. One of the advantages is that user can fit both data measured by Fourier transform and tunable diode laser spectrometers simultaneously. In the other words, it is conceivable to fit the spectra recorded at various resolutions, particularly data with high resolution is needed at low pressure to detect closely spaced lines while low resolution may be enough for high pressure because Lorentzian broadening removes the tiny details. Moreover, all the spectral conditions including the pass length, pressure, temperature, instrumental line shape, calibration factors and so on can be defined for each set of data. In addition, the user can fit all the recorded spectra at different pressures and temperatures simultaneously. So, this method of fitting all spectra together not only enables us to determine more reliable parameters but also helps up to save more time on analyzing data [111]. Some of the possible parameters that can be characterized by this software are pressure induce shifts and broadening as well as their temperature dependence coefficients and so on for different line shape profiles described in Chapter 2. All the required expressions for determining the broadening and pressure shifts parameters and their temperature dependency will be given in Chapter 3.

Probing the speed dependence of the molecular collision can be investigated by the following expression implemented in the Labfit software [112-115]:

$$\gamma^0(v) = \gamma^0\left\{1 + S\left[\left(\frac{v}{v_P}\right)^2 - c\right]\right\} \tag{3.3}$$

In the above expression, γ^0 is the mean pressure broadening value, v_{p} is the most probable speed at the temperature T ($v_P = \sqrt{\frac{2k_BT}{m}}$), v is the absolute active molecular velocity in the collision (c = 1.5) and S is the speed dependence coefficient. If the speed dependence coefficient is fixed to zero, then such equation leads to a non-speed-dependent model. Similar approach can be accomplished to obtain the speed dependence of the shift. For the case of the SDV, the real (K_s) and imaginary (L_s) parts of the line shape function can be obtained by inserting the speed dependence expression in the Voigt profile and integrating over all parameters (private communication with Dr. Chris Benner *et al*. [100]):

$$K_s(x,y,S) = \frac{2}{\pi}\int_{-\infty}^{\infty} e^{-v^2}\, v \tan^{-1}\left\{\left[\frac{v+x}{y(S\{v^2-c\}+1)}\right]^2\right\} dv \tag{3.4}$$

$$L_s(x,y,S) = \frac{1}{\pi}\int_{-\infty}^{\infty} e^{-v^2}\, v \ln\left\{\left[\frac{v+x}{y(S\{v^2-c\}+1)}\right]^2 + 1\right\} dv \tag{3.5}$$

In the above expression, *x* and *y* are the terms described in section 2.2.11.

4. Line Shape Study of Acetylene Diluted by Carbon Dioxide in the ν_1+ν_3 Band

4.1. Introduction

In this chapter, we will discuss the experimental study on acetylene (C_2H_2) diluted by carbon dioxide (CO_2) in the combination vibrational band ν_1+ν_3 covering 6471- 6617 cm^{-1} region. This section corresponds with the R-branch of the ν_1+ν_3 band. 22 ro-vibrational transitions were analyzed. The data collection was carried out using the TDL spectrometer in the *Molecular Spectroscopy* research lab at University of Lethbridge. The absorption spectra were recorded over a range of pressures from 50 to 500 Torr (50, 100, 200, 300, 400 and 500 Torr) and temperatures from 216 to 333 K (with a step of 20 K). Lean mixtures of acetylene and carbon dioxide (3% ~ 7% C_2H_2) were used in the experiments.

Four scans of each individual line were measured (it has been estimated that 4 scans are enough to get highest SNR ~ 2500 using the current TDLS). The objective of this project was to retrieve CO_2-broadened half-widths and collisional induced line shifts (CO_2 used as the foreign broadener and C_2H_2 lines were the subject of studying) along with their temperature dependencies employing a conventional Voigt line shape function. We did not find it necessary to take into account the line mixing and narrowing effects in our data analysis.

4.2. Results and Discussion

To perform the data analysis, initial values for line parameters were taken from the HITRAN database [4]. We note here that the HITRAN database provides the air-broadened line parameters and they were used in the absence of the CO_2-broadened ones. The line positions from HITRAN were used to improve the calibration of the spectra beyond what can be obtained with the wavemeter and the Fabry-Perot interferometer. The calibration procedure was described in Ref. [48].

The purpose of this step was to calibrate the absorption spectra that were shifted from their real positions. A line by line analysis procedure using the Wprofit [48 and references therein] software was used to obtain the collisional pressure shift and Lorentzian half width broadening coefficients from the following expressions:

$$\gamma(p,T) = p\left[\gamma^0_{CO2}(p_0,T_0) \times (1-\chi) \times \left[\frac{T_0}{T}\right]^{n_1} + \gamma^0_{self}(p_0,T_0) \times \chi \times \left[\frac{T_0}{T}\right]^{n_2}\right] \qquad (4.1)$$

$$v(T) = v_0 + p \times \left[\delta^0_{CO2}(T) \times (1-\chi) + \delta^0_{self}(T) \times \chi\right] \qquad (4.2)$$

In these equations, $\gamma^0$and δ^0 are the retrieved collisional pressure shift and Lorentzian half width broadening parameters in $cm^{-1}atm^{-1}$ at the reference temperature (296K) and pressure (1 atm), (p_0 and T_0) respectively. $\gamma(p,T)$ in cm^{-1} is the Lorentzian half width of the line at the total pressure p ($p = p_{C2H2} + p_{CO2}$) and temperature T. χ is the ratio of p_{self} over total p and n_1 and n_2 stand for the temperature dependence exponential coefficients.

Also, v represents the line center at pressure p and temperature T. An overview of the R16 line profiles at different pressures including the fit residuals are plotted in the Fig.4.1. after they are shifted to their expected line position. All the results obtained using the equations (4.1) and (4.2) are listed in the Tables 4.1 and 4.2. The indices m are equal to J+1 for R-branch transitions. The expressions for retrievals of the temperature dependence exponents for CO_2 pressure induce shift and CO_2-broadening parameters are given as follows:

$$\gamma(p,T) = p\gamma^{o}_{CO2}(p_0,T_0)\left[\frac{T_0}{T}\right]^n \tag{4.3}$$

$$\delta^0_{CO2}(T) = \delta^0_{CO2}(T_0) + \delta'_{CO2} \times (T - T_0) \tag{4.4}$$

in which, $\gamma^0$and δ^0 are the parameters described before, δ' indicates the temperature dependence of the collisional shift value. All the retrieved line parameters are given in Table 4.3.

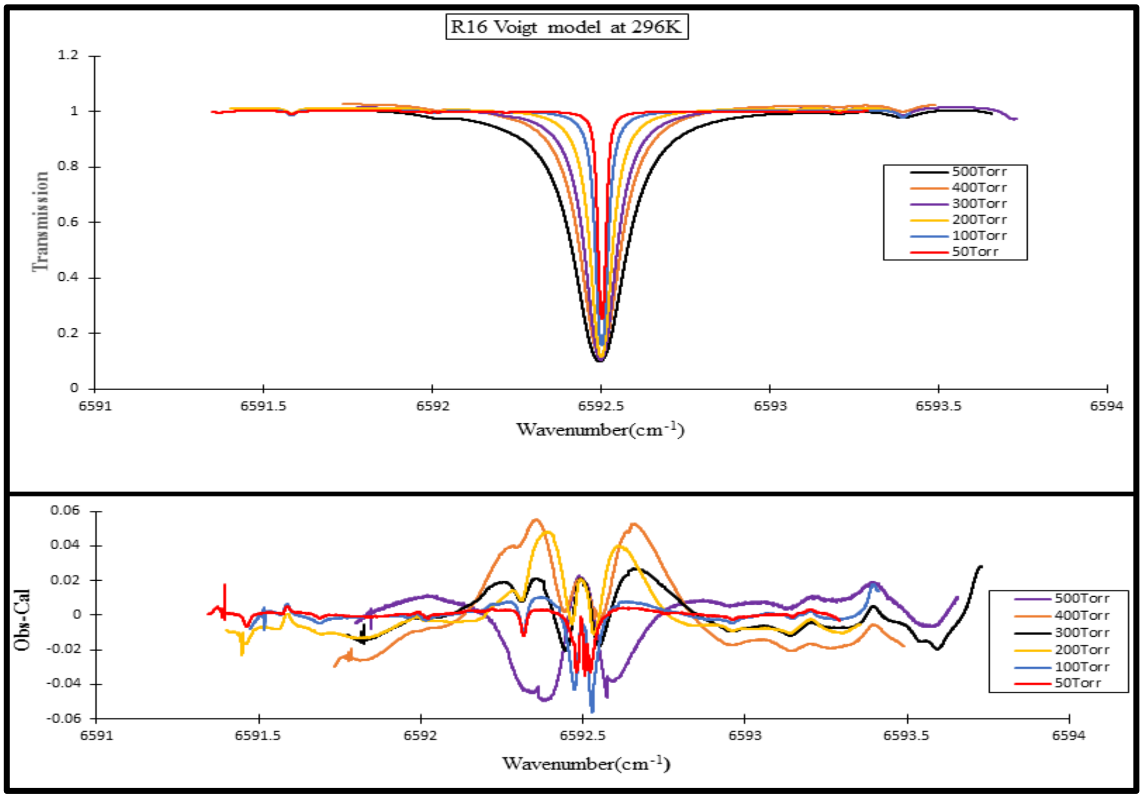

Figure 4.1. Plots of the R(16) transition as a function of wavenumber at six different pressures. The lower panel depicts the observed minus calculated (residuals) obtained using the Voigt model.

The collisional effect arises from the energy exchanges between the absorbers and perturbers involved in rotational, vibrational, and translational motions. These exchange of energy can be written in the form of $\gamma \approx 1/\tau_0$ [96] in which the γ is the collisional half width at half maximum (HWHM) and the τ_0 is the so-called free flight of duration of the absorber. This time can be approximated within the gas kinetic theory and expressed by the following expression [96]:

$$\tau_0 \approx \frac{l_0}{v_r} = \frac{k_B T/\sqrt{2}\pi d^2 P}{\sqrt{8k_B T/\pi\mu}} \tag{4.5}$$

where l_0 and v_r are the mean free path and the average relative speed, respectively. T is temperature, P is the pressure, d is the diameter of the molecule and μ is the reduced mass. Moreover, based upon the Boltzmann factor, increasing the temperature spreads out the population within a larger number of states (it is also worth noting to mention that for an ideal gas, the number of pertuber at a given P reduces by enhancing of T). Therefore, these two factors cause the broadening tends to be smaller with increasing the temperature at the given pressure as it is illustrated by Fig.4.2.

Martin *et al*. [48] performed the only similar study for the C_2H_2 diluted by CO_2 in the v_4+v_5 combination band. This study was performed at room temperature (298 K) using the Voigt profile. Since the CO_2-broadening coefficients do not depend on the vibrational band, a comparison between two studies is presented in the Fig. 4.6. In this figure all lines belonging to the R-branch reported in this paper are plotted only to display the trend. However, only a few lines are identical as the present study: R(4), R(6), R(10), R(14), R(16), and R(26). A fairly good agreement was observed between the two studies especially for higher J values.

Comparison of room temperature foreign broadening coefficients for R-branch transitions in the v_1+v_3 combination band of C_2H_2 diluted by CO_2 (present work) and with noble gases as well as , H_2, D_2, N_2 and air published by Ref. [48] are shown in Figs. 4.4 and 4.5. Instead of plotting the results in the X-axis by J (rotational quantum number), it is conventional to tag them as an index “m”. “m” is equal to *J*+1 for the *R* branch and -*J* for the *P* branch.

Table 4-1. Retrieved CO_2-broadening coefficients in (cm^{-1} atm^{-1}) obtained using the Voigt line shape model. The errors listed in parentheses correspond to one standard deviation.

		Temperature (K)						
Line	**m**	**216K**	**236K**	**256K**	**276K**	**296K**	**316K**	**333K**
R(1)	2	0.1551(3)	0.15390(2)	0.13000(2)	0.13110(2)	0.13990(2)	0.13340(4)	0.14060(3)
R(2)	3	0.1504(2)	0.14830(1)	—	—	0.11780(1)	0.11700(2)	—
R(4)	5	0.1339(2)	0.13690(2)	0.11570(1)	0.13100(1)	0.12130(2)	0.10250(1)	0.10710(2)
R(6)	7	0.1221(3)	0.12550(2)	0.09770(1)	0.10860(2)	0.09920(1)	0.09190(1)	0.08980(1)
R(8)	9	0.1145(2)	0.11900(1)	—	0.11230(1)	0.09910(2)	0.09240(1)	0.09300(1)
R(10)	11	0.0948(2)	0.11180(1)	0.08990(2)	0.08470(2)	0.08520(2)	0.07960(1)	0.08690(1)
R(12)	13	0.0960(1)	0.09060(2)	0.08690(1)	0.08120(1)	0.08620(1)	0.07600(1)	0.08430(2)
R(14)	15	0.0937(8)	0.08670(1)	0.08175(9)	0.08526(9)	0.07930(1)	0.07060(1)	0.06990(1)
R(16)	17	0.0933(7)	0.08798(7)	0.08329(7)	0.08238(7)	0.07641(8)	0.06775(5)	0.07045(4)
R(18)	19	0.0911(4)	0.08569(6)	0.07888(5)	0.07810(6)	0.07111(8)	0.06523(5)	0.06220(4)
R(20)	21	0.0889(4)	0.08203(4)	0.07807(4)	0.07607(4)	0.06935(6)	0.06491(3)	0.06360(3)
R(21)	22	0.0771(7)	0.07439(10)	0.06927(9)	0.06890(1)	0.06560(1)	0.05426(9)	0.05590(7)
R(22)	23	0.0820(4)	0.07823(3)	0.07292(5)	0.07327(5)	0.06958(4)	0.06186(3)	0.06210(4)
R(23)	24	0.0842(3)	0.07665(5)	0.07176(5)	0.07092(4)	0.06152(6)	0.05820(6)	0.05740(5)
R(24)	25	0.0851(5)	0.07629(5)	0.07285(5)	0.06787(4)	0.06351(5)	0.05888(3)	0.05630(3)
R(25)	26	0.0772(5)	0.07249(5)	0.06849(5)	0.06385(5)	0.06042(5)	0.05598(4)	0.05130(5)
R(26)	27	0.0797(8)	0.06967(5)	0.06650(5)	0.06359(5)	0.06187(5)	0.05697(8)	0.05390(6)
R(27)	28	0.0779(3)	0.06916(5)	0.06673(4)	0.06555(3)	0.05913(4)	0.05657(3)	0.05020(4)
R(28)	29	0.0755(8)	0.07237(8)	0.06137(9)	0.06349(7)	0.05502(5)	0.05045(4)	0.04970(5)
R(29)	30	0.0767(5)	0.07627(6)	0.06661(7)	0.06434(5)	0.05741(4)	0.05599(3)	0.05220(3)
R(30)	31	—	—	0.06560(3)	0.06050(2)	0.05426(9)	0.04995(8)	0.04830(8)
R(31)	32	—	—	—	0.06253(4)	—	0.05824(9)	0.05350(6)

Table 4-2. Retrieved CO_2- Pressure induced shifting Parameters in (cm^{-1} atm^{-1}) using Voigt model line shape. Errors listed in parentheses correspond to one standard deviation.

		Temperature (K)						
Line	**m**	**216K**	**236K**	**256K**	**276K**	**296K**	**316K**	**333K**
R(1)	2	-0.00320(1)	-0.0016(1)	-0.00350(1)	-0.0044(1)	-0.00270(1)	-0.0061(2)	-0.00190(2)
R(2)	3	–	-0.00134(9)	–	–	-0.0030(1)	-0.0064(1)	–
R(4)	5	-0.00490(1)	-0.00184(15)	-0.00188(10)	-0.00252(8)	-0.00290(1)	-0.00597(10)	-0.00370(2)
R(6)	7	-0.00520(1)	-0.00380(1)	-0.00629(3)	-0.00572(9)	-0.00350(1)	-0.00703(7)	-0.00610(1)
R(8)	9	-0.01338(9)	-0.01092(7)	-0.00808(0)	-0.01007(9)	-0.00450(1)	-0.00559(7)	–
R(10)	11	-0.01047(9)	-0.00860(2)	-0.00743(8)	-0.00899(9)	-0.00660(1)	-0.00755(7)	-0.00940(1)
R(12)	13	-0.01387(7)	-0.01322(9)	-0.00852(7)	-0.01143(5)	-0.00930(1)	-0.01036(6)	-0.01130(1)
R(14)	15	-0.01634(4)	-0.01272(6)	-0.01208(5)	-0.01039(5)	-0.00970(1)	-0.00895(5)	-0.00990(1)
R(16)	17	-0.01676(4)	-0.01457(5)	-0.01343(5)	-0.01416(5)	-0.01217(5)	-0.01067(3)	-0.01065(3)
R(18)	19	-0.01975(3)	-0.01858(4)	-0.01752(4)	-0.01664(4)	-0.01530(1)	-0.01581(3)	-0.01463(3)
R(20)	21	-0.01890(3)	-0.01798(3)	-0.01628(3)	-0.01798(3)	-0.01422(4)	-0.01317(2)	-0.01295(2)
R(21)	22	-0.01856(4)	-0.01973(6)	-0.01677(6)	-0.01715(8)	-0.01510(1)	-0.01391(5)	-0.01300(4)
R(22)	23	-0.02150(3)	-0.02019(2)	-0.01911(4)	-0.01891(3)	-0.01641(3)	-0.01617(2)	-0.01435(3)
R(23)	24	-0.02149(2)	-0.02042(4)	-0.01796(3)	-0.01812(3)	-0.01619(4)	-0.01547(4)	-0.01466(3)
R(24)	25	-0.02255(3)	-0.02077(3)	-0.01916(3)	-0.01905(3)	-0.01671(3)	-0.01632(2)	-0.01559(2)
R(25)	26	-0.02415(4)	-0.02271(3)	-0.02116(4)	-0.02009(4)	-0.01872(4)	-0.01723(3)	-0.01678(3)
R(26)	27	-0.02570(5)	-0.02359(3)	-0.02197(3)	-0.01998(3)	-0.01827(3)	-0.01748(5)	-0.01640(4)
R(27)	28	-0.02452(2)	-0.02339(3)	-0.02200(3)	-0.02061(2)	-0.01932(3)	-0.01859(2)	-0.01718(3)
R(28)	29	-0.03020(5)	-0.02544(6)	-0.02540(6)	-0.02216(5)	-0.02034(3)	-0.01902(3)	-0.01837(3)
R(29)	30	-0.02564(3)	-0.02513(5)	-0.02370(5)	-0.02193(3)	-0.02129(2)	-0.02079(2)	-0.02007(2)
R(30)	31	–	–	-0.02270(2)	-0.02105(13)	-0.02068(11)	-0.02044(6)	-0.02007(6)
R(31)	32	–	–	–	-0.02324(3)	–	-0.02073(6)	-0.01968(8)

Another comparison is presented in Figures 4.5. and 4.6. These two figures represent the CO_2-broadening and CO_2-pressure induce shift of C_2H_2 perturbed by gases other than CO_2 in the $\nu_1+\nu_3$ vibrational bands [34]. This is a room temperature study where the Voigt line model was used to describe the line profiles.

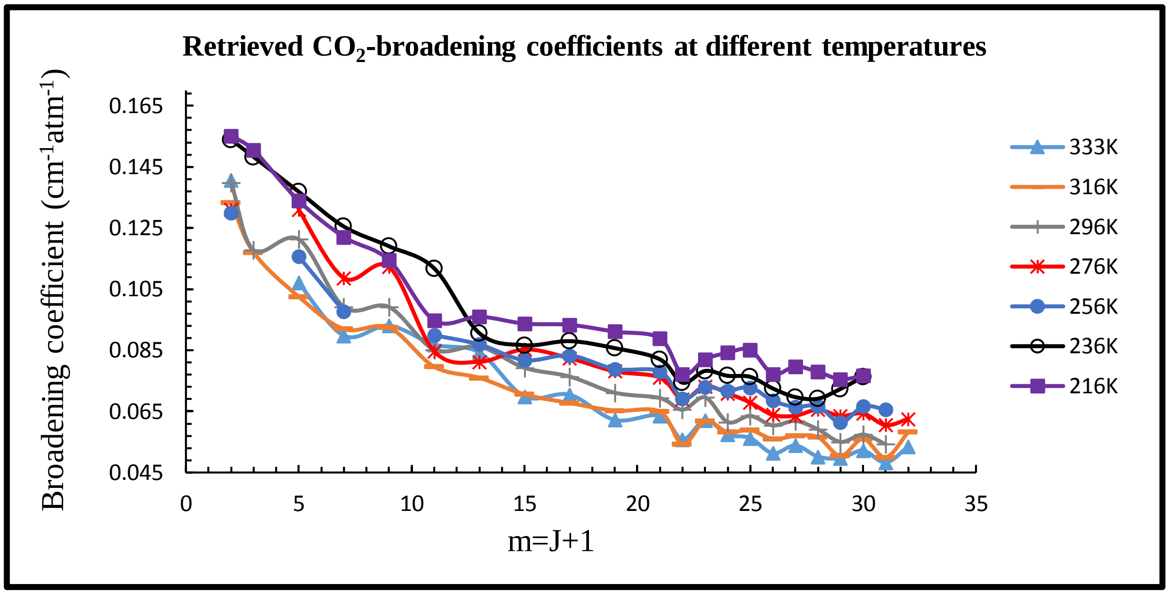

Figure 4.2. CO_2-broadening parameters in ($cm^{-1}atm^{-1}$) at different temperatures retrieved with the Voigt profile for 22 transitions in the R-branch of the $\nu_1+\nu_3$ band of C_2H_2.

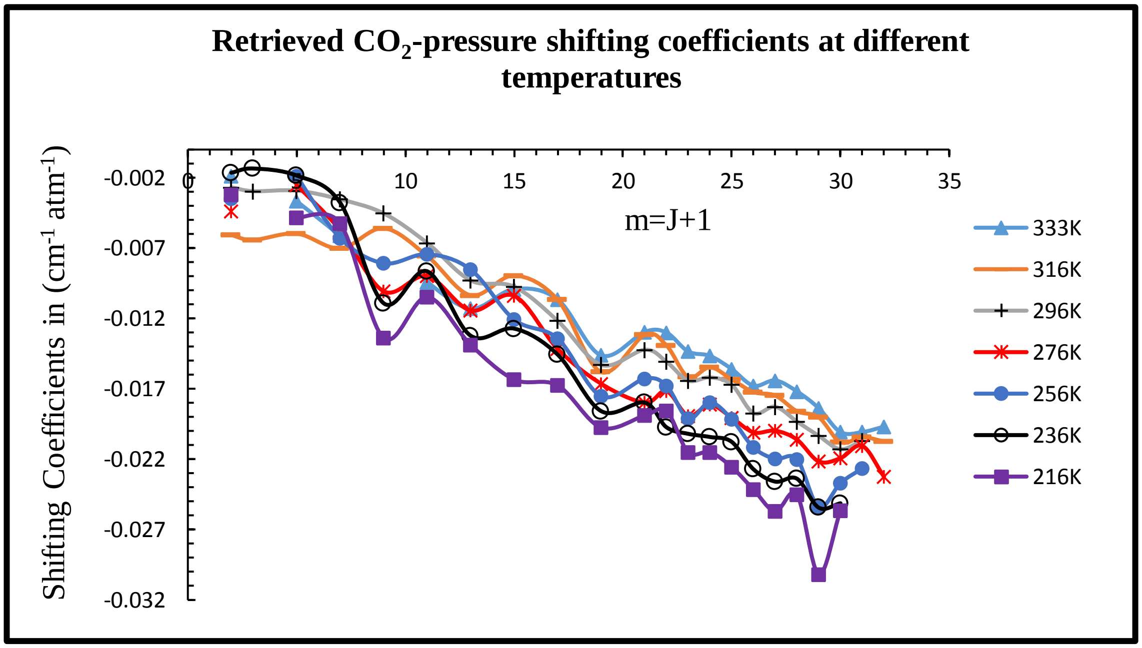

Figure 4.3. CO_2-pressure shifting coefficients ($cm^{-1}atm^{-1}$) at different temperatures retrieved with the Voigt profile for 22 transitions in the R-branch of the $\nu_1+\nu_3$ band of C_2H_2.

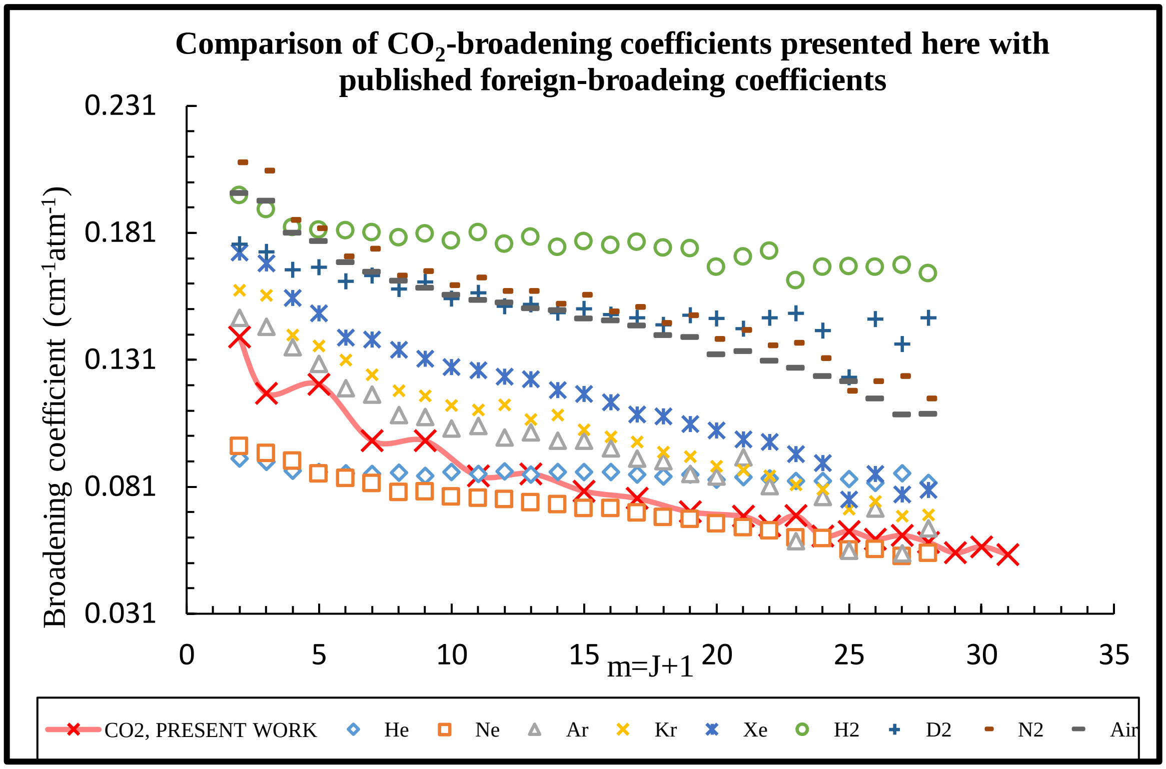

Figure 4.4. Comparison of room temperature foreign broadening coefficients for R-branch transitions in the v_1+v_3 combination band of C_2H_2 perturbed by CO_2 (present work) and with other gases [48].

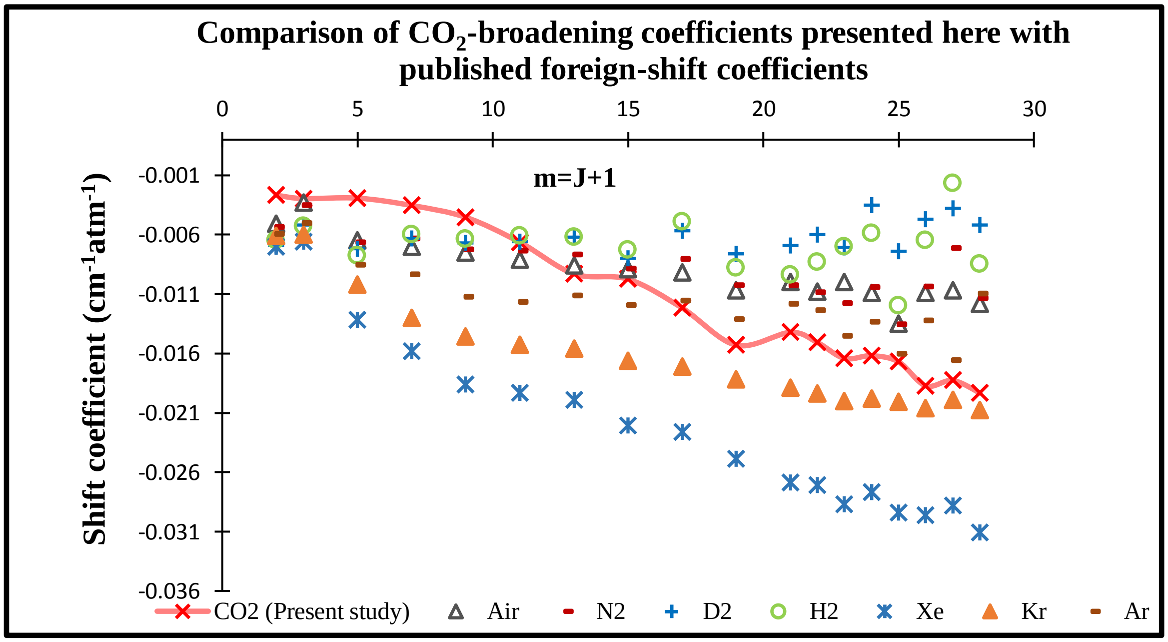

Figure 4.5. Comparison of room temperature foreign pressure-shift coefficients for R-branch transitions in the v_1+v_3 combination band of C_2H_2 perturbed by CO_2 (present work) and with other gases [48].

Table 4-3. Temperature dependence exponents of the pressure-induced shift and Lorentz half widths of the C_2H_2 perturbed by CO_2. The errors listed in parentheses correspond to one standard deviation.

Line	**m**	**Line Positions** [a]	**Broadening Temperature Dependency Exponents *10^{-1} (n_1)**	**Shifting Temperature Dependency Exponents*10^{-5} (δ')**
R(1)	2	6561.094106	2.712 (4)	-0.810 (7)
R(2)	3	6563.370066	7.532 (7)	-2.46 (2)
R(4)	5	6567.844393	5.840 (2)	-1.05 (1)
R(6)	7	6572.215019	7.544 (2)	-1.16 (2)
R(8)	9	6576.481658	5.930(9)	9.81 (3)
R(10)	11	6580.644023	4.990 (9)	1.16 (3)
R(12)	13	6584.701858	3.831(2)	2.34 (1)
R(14)	15	6588.654889	6.450(1)	5.33 (5)
R(16)	17	6592.502871	7.143 (9)	4.98 (1)
R(18)	19	6596.245545	8.772(2)	4.20 (3)
R(20)	21	6599.882800	7.830(4)	5.36 (4)
R(21)	22	6601.661700	8.058(4)	5.44 (5)
R(22)	23	6603.414100	6.611(1)	5.84 (1)
R(23)	24	6605.140100	9.140(10)	5.85 (1)
R(24)	25	6606.839500	9.338(1)	5.86 (1)
R(25)	26	6608.512400	9.130(3)	6.46 (4)
R(26)	27	6610.158700	8.140(4)	7.97 (1)
R(27)	28	6611.778400	8.981(1)	6.22 (2)
R(28)	29	6613.371500	10.27(5)	9.71 (3)
R(29)	30	6614.938000	9.435(1)	5.05 (2)
R(30)	31	6616.477800	12.23(5)	—
R(31)	32	6617.991000	—	—

[a] Line positions are taken from Ref. [4].

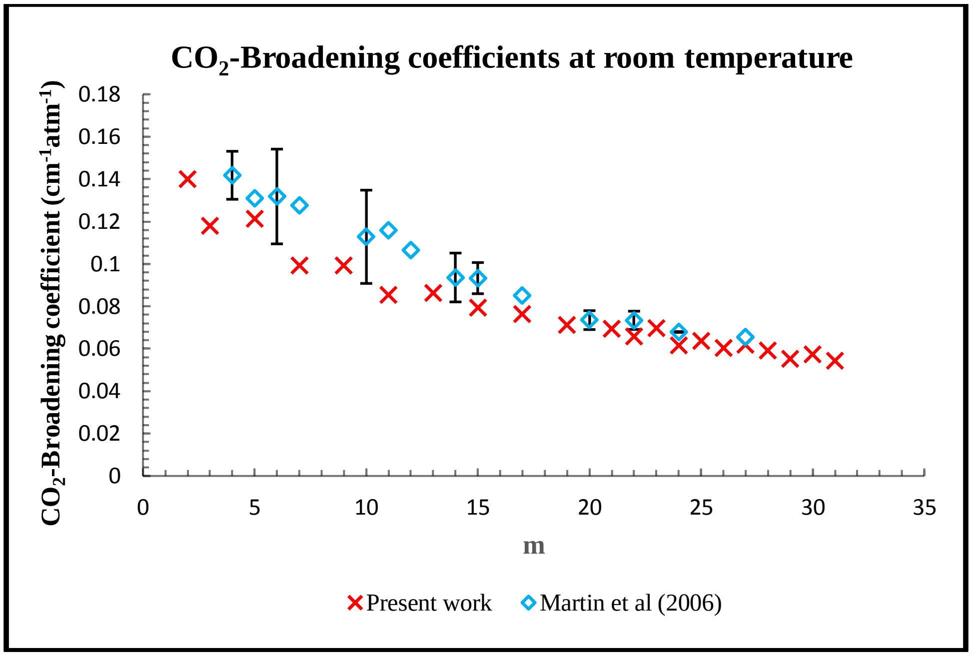

Figure 4.6. This graph presents broadening half width comparison between present work (v_1+v_3) and Martin et al.[48] (v_4+v_5). All the lines belonging to R branch of Martin *et al.*[48] study are plotted here. Note that only the transitions with error bars are common in the present study and Martin *et al.* [48].

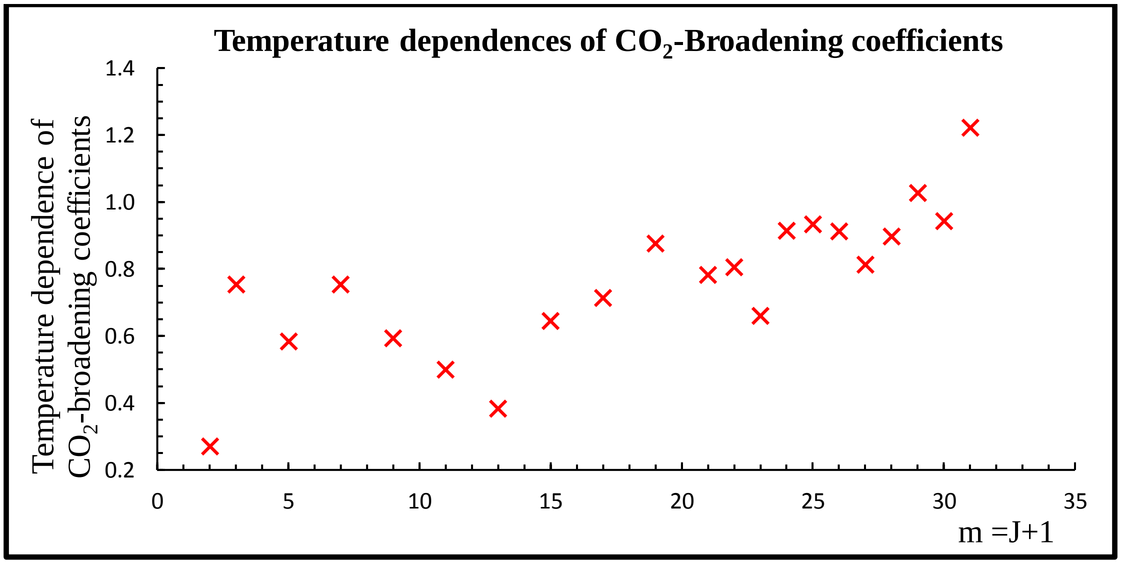

Figure 4.7. The temperature dependence exponents of CO$_2$-broadening of C_2H_2 transitions over a range of temperatures between 216 and 333 K.

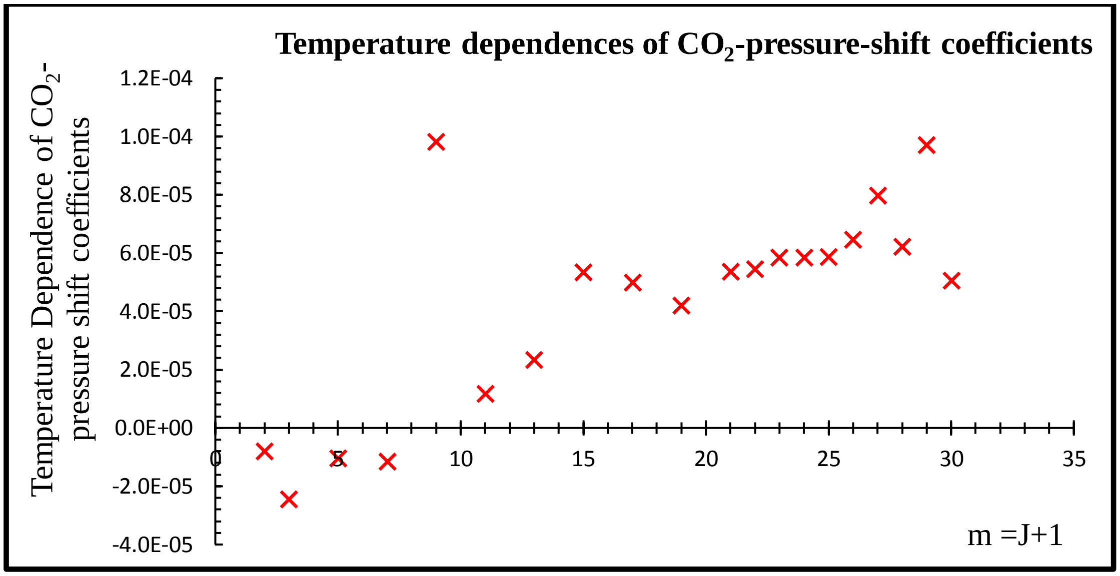

Figure 4.8. The temperature dependence coefficients of CO_2- pressure shifts for C_2H_2 transitions over a range of 216K to 333K.

In conclusion, the CO_2-Lorentz half width and collisional pressure shift coefficients belonging to the v_1+v_3 vibrational bands of C_2H_2 as well their temperature dependencies have been retrieved. A good agreement between presented broadening results and those published by Ref.[48] at room temperature is achieved.

5. Ro-Vibrational Emission Spectra of $D^{12}C^{14}N$

5.1. Introduction

In this chapter, we will report an experimental study on ro-vibrational energy states of $D^{12}C^{14}N$ in the region of 450 to 850 cm^{-1} recorded at 1370 K. The spectrum included excited vibrational states up to a vibrational level v=5. An overview of infrared emission spectra of Deuterium Cyanide (DCN) is presented in Fig.5.1. Hydrogen Cyanide (HCN) was present as an impurity in the sample.

The spectra were recorded with 0.005 cm^{-1} resolution using the experimental set-up described in section 3.3 that is available at the Justus-Liebig Universität, Giessen, Germany. The spectrum analysis software SyMath (see section 3.4.) was used to analyze the spectra and obtain improved spectroscopic constants. The DCN spectra were found to have traces of HCN. The HCN transitions [59, 116, 117] were used in the self-calibration of the wavenumber scale. In addition, the intensities [117] were calibrated by ensuring that the calculated intensities for strong HCN transitions matched the corresponding experimental intensities.

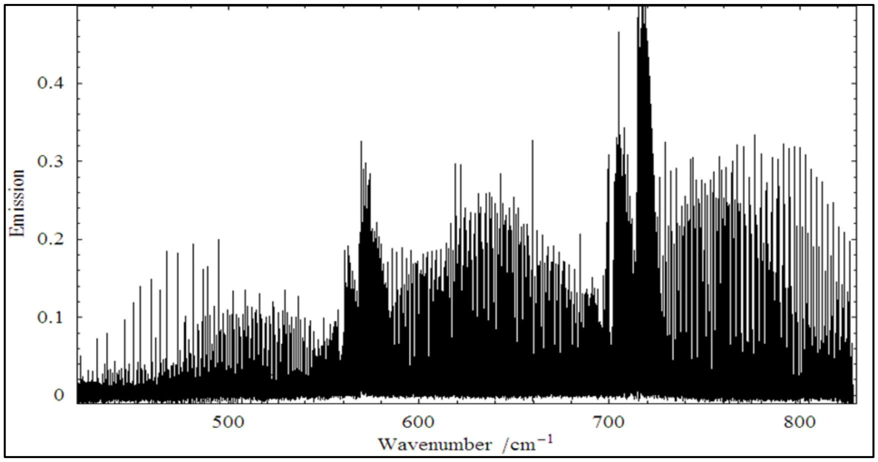

Figure 5.1. Overview of the recorded emission spectra recorded at 1370 K.

5.2. Results and comparison

The assignments have been carried out in a sequence starting from the most intense band, and gradually moving one by one towards the less intense bands. All together we have analyzed 15 bands. Each time we encountered overlapping spectral features, we used the deconvolution feature described above. This feature of the software allowed us to measure accurately the individual line positions for a large number of transitions hidden under broad features in the spectra. During the analysis, the molecular constants are continuously fine-tuned using the spectroscopic information from both weak and intense assigned transitions.

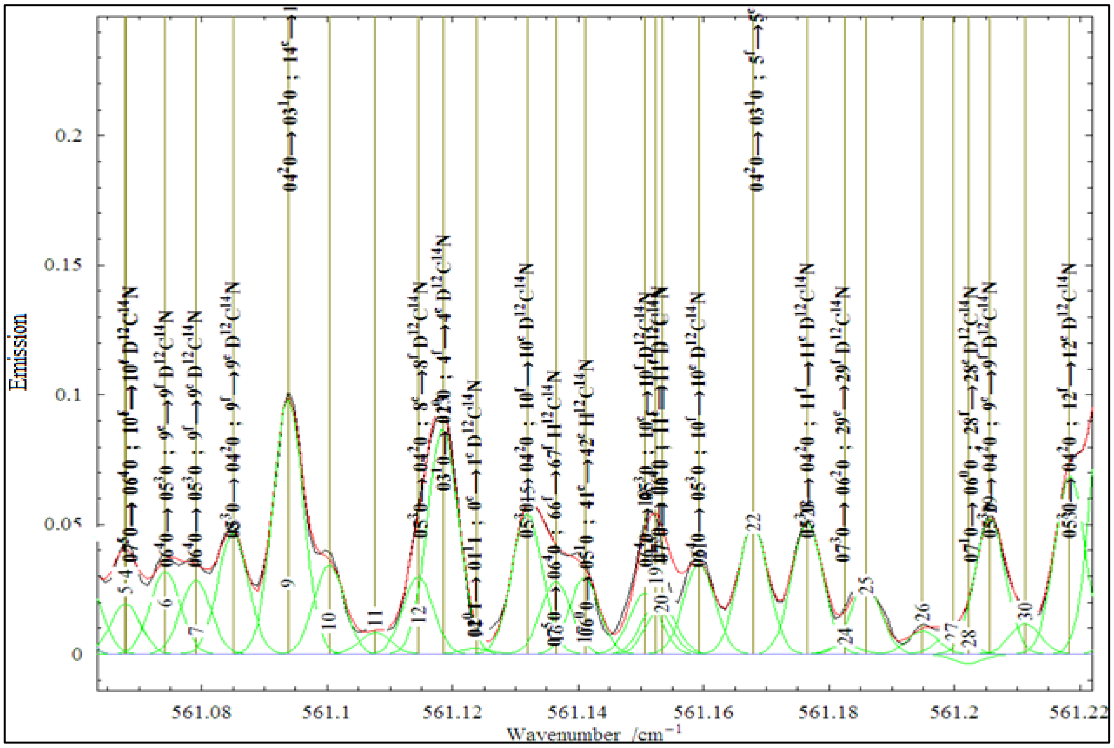

Figure 5.2. Zoomed-in view of a plot window for the analysis method enabled by SyMath that combines a line shape analysis with spectroscopic assignments. Color code: black - recorded spectra; green - line shape of each transition modeled by a Doppler profile; blue - spectral modeled all transitions that share the same set of effective Hamiltonian matrices, red - summation of neighbouring green lines. The overlapping transition labels on the plot can be removed if needed.

In Fig.5.2 we present a section of the emission spectrum where all assigned transitions are labelled. We have assumed that at the low pressures of DCN used in our study, the effects due to pressure-induced shifts are negligible and only therefore the effects due to molecular thermal motion have to be taken into account. All profiles were assumed to be Doppler broadened and they were modelled in our spectra using the well-known Doppler profile (see section 2.2.9).

Table 5-1. Band Centers (in cm^{-1}) for $D^{12}C^{14}N$ bands analyzed in this study. All errors represent two standard deviations.

Transition	Band Center (v_c)
0110-0000	569.0408231(19)
0200-0000	1129.988388(20)
0220-0000	1137.891569(16)
0200-0110	560.94756490(3)
0220-0110	568.85074590(4)
0310-0110	562.11714660(3)
0330-0110	565.02255610(5)
0310-0200	560.90049610(3)
0310-0220	552.99731520(3)
0330-0220	568.67138180(5)
0400-0200	1113.970730(16)
0420-0220	1113.8437440(6)
0400-0310	553.0702339(20)
0420-0310	560.84642890(3)
0440-0330	568.5024858(10)
0510-0310	1106.190388(10)
0530-0330	1105.957353(13)
0510-0400	553.12015420(9)
0510-0420	545.34395910(7)
0530-0420	560.7849903(12)
0550-0440	568.34361310(1)

The initial values for the molecular constants in the Eq. (2.66-2.80) are taken from Ref. [58]. In this way we were able to extend our knowledge to retrieve the parameters of interest by climbing up the vibrational bending levels of $D^{12}C^{14}N$. The retrieved results for the molecular parameters are listed in Tables 5.2 and 5.3. In the same table we present the experimental results from Ref. [58]. As can be seen, our molecular constants agree well with the corresponding constants reported in Ref. [58]. The errors given in Tables 5.1 to 5.3 represent two standard deviations, illustrating improved results compared with those of the previous study [58]. To obtain the band centers reported in Table 5.1, Eq. (2.73) was used. The ro-vibrational parameters of dense $D^{12}C^{14}N$ spectra were analyzed using the SyMath software. Spectra includes high excited vibrational states up to vibrational bands equal to 11, however, only the results obtained for states up to v=5 are presented in this chapter. The next step is the determination of the line intensities for all assigned transitions. In the assignment of this study, it was tried to fit the spectra until we reached to the noise level. Moreover, J_{max} of present study is larger than the compared one as it is shown in table 5-2.

Table 5-2. Ro-vibrational Parameters (in cm^{-1}) for $D^{12}C^{14}N$ after correction for *l*-type resonance from this study and Mollmann *et al*.

$v_1\ v_2\ l\ v_3$	$G_0(v, l)^a$	$G_0(v, l)^b$	B_v [a]	B_v [b]	$D_v \times 10^{6\ a}$	$D_v \times 10^{6\ b}$	$H_v \times 10^{12\ a}$	$H_v \times 10^{12\ b}$	J_{max}^a	J_{max}^b
0 0 0 0	0	0	1.20775241(36)	1.207750950(16)	1.927277(4)	1.92684(18)	2.7410(11)	2.773(75)	70	65
0 1 1 0	570.2528968(32)	570.252855(18)	1.21207374(34)	1.212072630(41)	1.996800(4)	1.99667(19)	3.4860(11)	3.572(73)	70	69
0 2 0 0	1129.988388(43)	1129.988301(25)	1.21665041(41)	1.216649344(84)	2.066468(6)	2.06616(22)	5.1400(26)	4.807(83)	70	62
0 2 2 0	1142.756670(38)	1142.756661(22)	1.21627526(32)	1.216274045(62)	2.068459(3)	2.06816(19)	4.1301(10)	4.218(72)	70	62
0 3 1 0	1692.109999(42)	1692.109974(25)	1.22111486(33)	1.221113751(78)	2.137530(3)	2.13776(86)	5.8050(11)	5.909(77)	60	58
0 3 3 0	1717.546059(44)	1717.545947(49)	1.22034536(33)	1.22034431(16)	2.140760(4)	2.14027(84)	4.5000(11)	4.498(84)	60	59
0 4 0 0	2243.959118(50)	2243.959237(96)	1.22585176(38)	1.22584916(83)	2.210811(4)	2.2093(22)	7.8460(15)	7.62(48)	60	58
0 4 2 0	2256.637133(45)	2256.63704(12)	1.22545498(33)	1.22545447(65)	2.208171(3)	2.2096(12)	6.0470(10)	6.69(31)	60	57
0 4 4 0	2294.653790(53)	2294.65357(15)	1.22427209(35)	1.22427126(74)	2.212756(4)	2.2118(18)	4.2920(12)	3.88(36)	60	50
0 5 1 0	2798.309743(51)	2798.30926(17)	1.23047085(38)	1.23047101(96)	2.281331(5)	2.2821(29)	7.9870(19)	8.37(65)	60	58
0 5 3 0	2823.587251(54)	2823.58699(27)	1.22966085(36)	1.22965949(13)	2.279684(4)	2.2784(16)	6.0120(14)	5.88(48)	60	57
0 5 5 0	2874.110248(67)	2874.10995(25)	1.22804793(50)	1.22804637(13)	2.289681(8)	2.2881(32)	5.1780(39)	4.95(60)	60	51

[a] Molecular constants from the present study in cm^{-1} units.

[b] Molecular constants from Mollman *et al*. in cm^{-1} units.

Table 5-3. *l*- Type Resonance Parameters for $D^{12}C^{14}N$ given in cm^{-1} from this study and Ref. [58].

$q_v \times 10^{3\,a}$	$q_v \times 10^{3\,b}$	$q_{vJ} \times 10^{8\,a}$	$q_{vJ} \times 10^{8\,b}$	$q_{vJJ} \times 10^{12\,a}$	$q_{vJJ} \times 10^{12\,b}$	$\rho_v \times 10^{8\,a}$	$\rho_v \times 10^{8\,b}$	$q_l \times 10^{4\,a}$	$q_l \times 10^{4\,b}$
6.2106170 (11)	6.2106573(8)	7.34106(16)	7.3443(8)	1.4043(5)	1.421(9)				
6.2892510 (20)	6.2885010(32)	7.68253(39)	7.7327(70)	1.5082(19)	1.575(28)	[-1.290]	[-1.260]	[0.04288]	[0.0427]^{C}
6.3681233 (5)	6.3682480(23)	8.09253(9)	8.1432(60)	1.5449(36)	1.728(25)	[-1.285]	-1.275(54)	0.0435157(9)	[0.0427]
6.4500934 (5)	6.4500190(245)	8.55120(9)	8.5550(38)	1.7859(32)	1.881(139)	[-1.323]	-1.313(56)	0.0437801(6)	[0.0427]
6.5343264(6)	6.5344000(15)	9.01230(13)	9.0210(37)	1.8660(58)	1.913(184)	[-1.342]	-1.338(57)	0.0423340(6)	[0.0427]

[a] Molecular constants from the present study in cm^{-1} units.
[b] Molecular constants from Ref. [58] (Mollman *et al.*) in cm^{-1} unit.
[c] Parameters are fixed to the values in the bracket.

This chapter reports the experimental ro-vibrational coefficients of $D^{12}C^{14}N$ gas within the range of 450 to 850 cm^{-1} up to v=5. These coefficients can be exploited to achieve the line position of transitions up to maximum the J_{max} presented in this chapter. Furthermore, the band center values of spectra located in this region are calculated and presented in table 5-1. Self-calibrating the spectra using the line positions provided by Refs. [59, 116, 117] and the Symath software improved the errors compared to Ref. [58].

6. Spectroscopy Line Shape Study of $^{12}C^{16}O$ Broadened by CO and H_2 in the First Overtone Band

6.1. Introduction

In this chapter, we reported an experimental study on pure carbon monoxide and carbon monoxide diluted in hydrogen. The self- and foreign- Lorentz half width, collisional pressure shift parameters as well as other coefficients in the first overtone (2-0) vibrational region of CO have been studied and the results also are presented in this chapter (term “self” refers to the study of pure CO and term “foreign or buffer” used for the H_2 as the perturber. However, in both case the CO lines were the subject of study).

Table 6-1. Summary of experimental conditions of the measured spectra using pure CO and CO-H_2 mixture.

Gas	Temperatures (+/- 0.5K)	Cell Pressures (Torr ~ 0.2%)	Gas Mixture Ratio	Path Length (m)
Pure CO	298.30	3.15	1.000	0.1000
Pure CO	297.90	4.47	1.000	0.1000
Pure CO	298.20	9.40	1.000	0.1000
Pure CO	298.15	123.85	1.000	0.1000
Pure CO	298.15	279.90	1.000	0.1000
Pure CO	298.20	507.00	1.000	0.1000
Pure CO	298.05	329.50	1.000	0.0205
Pure CO	298.05	148.30	1.000	0.0205
Pure CO	298.05	97.26	1.000	0.0205
Pure CO	298.15	1.36	1.000	1.5000
CO-H_2	298.20	155.15	0.183	0.1000
CO-H_2	298.05	315.65	0.203	0.1000
CO-H_2	297.85	474.65	0.240	0.1000

We implemented two line shape functions namely the Voigt and speed dependent Voigt profiles, including the line mixing effects. The data collection was carried out using the high resolution FTS (Fourier transform spectrometer described in Ref. [84]) at the McMath-Pierce facility of the National Solar Observatory on Kitt Peak, AZ. A brief table of experimental conditions is given in Table 6.1.

6.2. Spectroscopic results

A similar analysis procedure to the one described in section 4.2 has been used in this study with initial values taken from HITRAN [5]. The expressions (4.1) and (4.2) have been employed in the Labfit software (see section 3.5) to acquire the spectroscopic line parameters. Forty six ro-vibrational P- and R-branch transitions of carbon monoxide were fitted simultaneously. As shown in Table 6.1, most of the spectra were recorded in 298 K (the average temperature is 298.1 K). Hence, there was no need to include the temperature dependences in the data analysis process. Figures 6.1, 6.2 and 6.3 show the multi-spectrum fit regions 4146 to 4332 cm^{-1} for the P(23) to R(23) transitions in the 2-0 band of CO. Applying the speed dependent Voigt model instead of Voigt model, leads us to have better residuals for the band of interest.

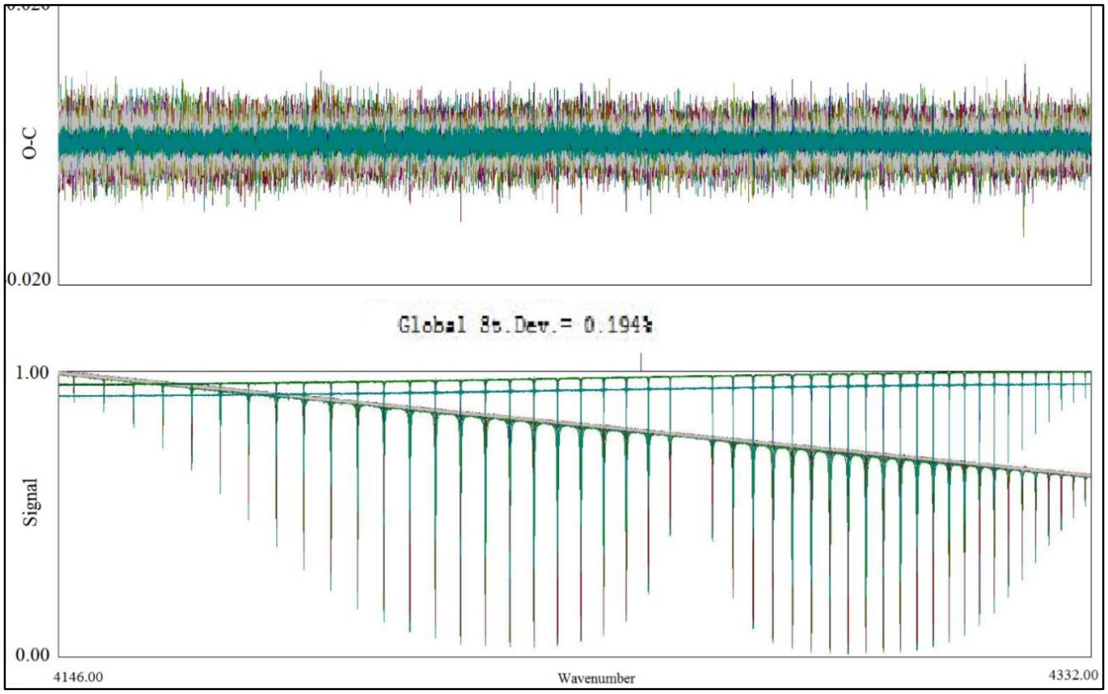

Figure 6.1. Lower panel: over 10 spectra of pure CO analyzed in this work using the Voigt Profile. The standard deviation is shown to be 0.194%. Upper Panel: fit residuals.

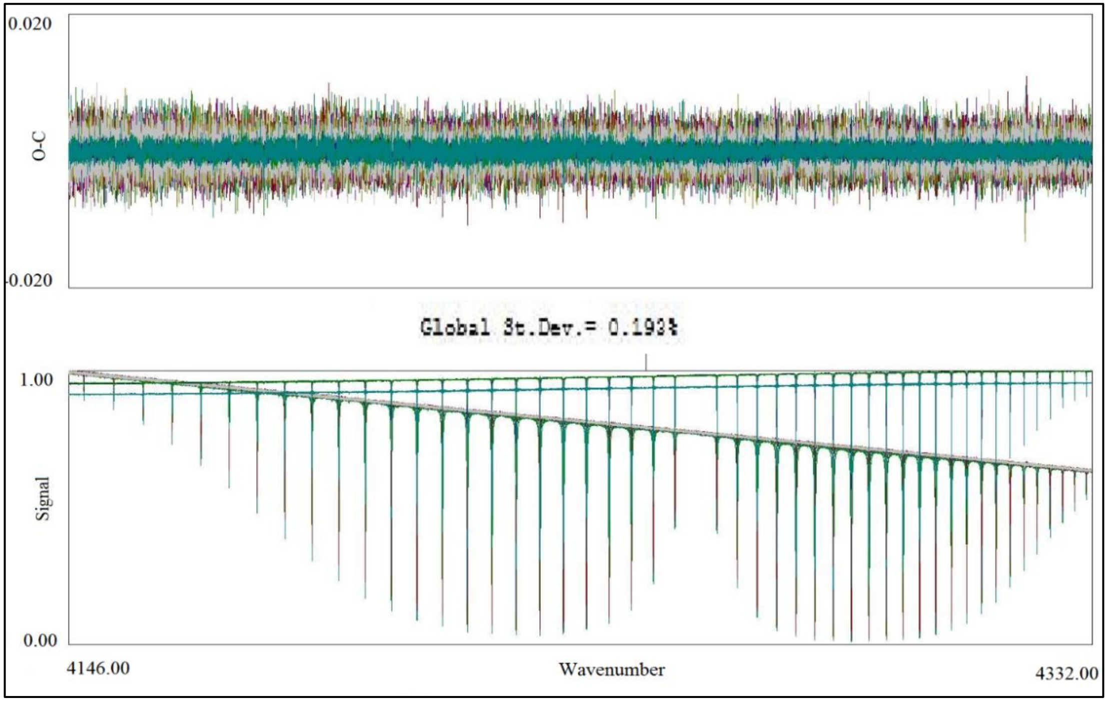

Figure 6.2. Lower panel: over 10 spectra of pure CO analyzed in this work using the speed dependent Voigt Profile. The standard deviation is shown to be 0.193%. Upper Panel: fit residuals.

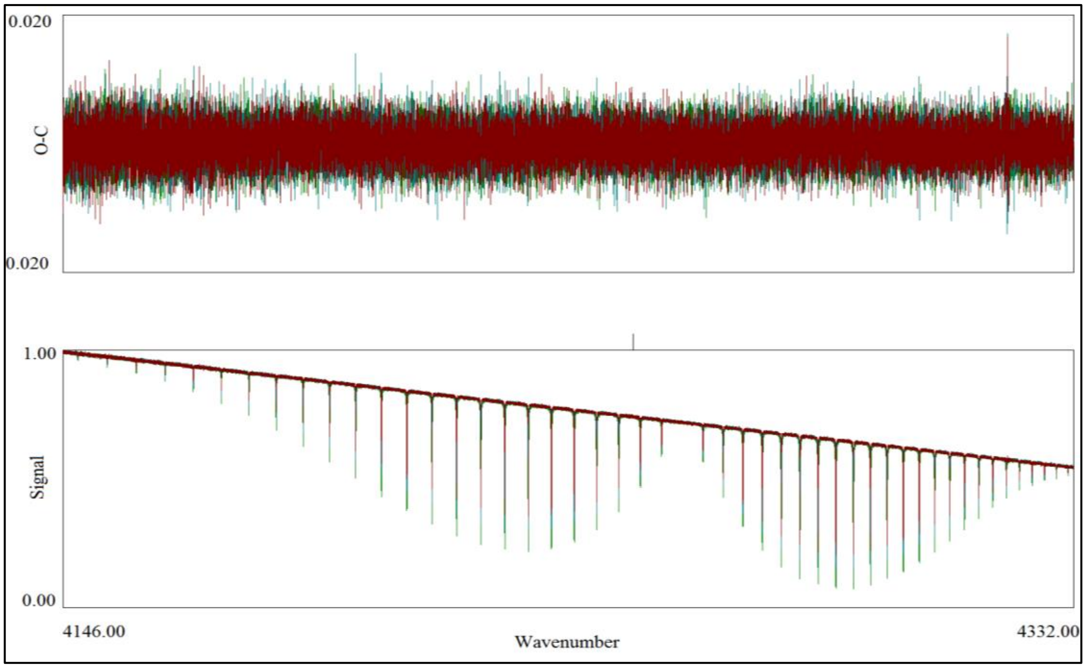

Figure 6.3. Lower panel: over plotted 3 spectra of CO mixed by H_2 analyzed in this study using the Voigt profile. Upper Panel: fit residuals.

The retrieved line centers (cm^{-1}), line intensities (cm^{-1}/ (molecule cm^{-2})), self- and foreign-Lorentz half widths and pressure induced line shift (all in cm^{-1} atm^{-1}) and line mixing coefficients (atm^{-1}) for CO-CO and CO-H_2 parameters are listed in the Tables 6.2 to 6.5. In these tables, the term "*m*" is known as an index for the rotational quantum number. It is equal to *–J* and *J+1* for the P-branch and R-branch, respectively.

In the fitting of 10 spectra (see Table 6.1) of CO-CO study, we tried to fit the spectra to noise level in a way to float all the reported five parameters. Comparisons are made in Figures 6.4 to 6.6 and 6.10 of the present study and similar published results. In this case (CO-CO study), the self-Lorentz half width, pressure induced shift and line mixing coefficients are produced by floating the line centers and intensities.

The analysis process was repeated until the spectra were fitted to the noise level. In section 1.5.2 we presented the status of knowledge on CO-CO and CO-H_2. The most recent study of CO was been performed by V.M. Devi *et al.* in 2012 [70]. The authors simultaneously analyzed the CO-CO and CO-air spectra at several temperatures (accessing to more spectra) using the same fitting software. As it is shown (see Fig 6.4 to 6.6 and 6.10), their results are in good agreements with similar studies. The errors listed in parentheses correspond to one standard deviation in this chapter. Two line shape functions namely, Voigt and Speed Dependent Voigt models were employed to determine the spectroscopic parameters.

In the case of CO-H_2, we were not able to accomplish the same fitting technique that described for CO-CO case. To overcome this challenge, all the line positions in the P branch as well as some lines in the R branch (R19 to R23) were fixed to the line positions reported by Ref [70] while rest of the parameters were obtained by floating them and fitting until we can reach the noise level. So far, no published works were able to characterize the line mixing coefficients of CO-H_2 (line mixing via Rosenkranz's first-order approximation [118]). Fig.6.7. depicts weak coupled Rosenkranz's line mixing of CO-H_2 obtained in the present study (PS) using the Voigt model. Due to a lower signal-to-noise ratios in the CO-H_2 spectra, the speed dependence of H_2-broadened half widths could not be quantified.

Within the impact approximation, the line shape of the spectra is simply constructed by a sets of elements called the Relaxation Matrix in this impact limit. The diagonal elements of this matrix are complex quantities such that the real part defines the broadening coefficients while the imaginary part describes the line shift parameters as follows:

$$W_{kk} = \gamma_k + i\delta_k \tag{6.1}$$

Table 6-2. Retrieved experimental parameters in the P-branch of CO-CO (2-0) spectra applying Voigt and SDV models. In this table, “a” is measured in [cm^{-1}/ (molecule cm^{-2})], “b, c” are coefficients measured in [cm^{-1} atm^{-1}] and “d”is in atm^{-1} at 296K.

		Retrieved parameters using Voigt model					Retrieved parameters using SDV model				
Line	m	Line Position(cm^{-1})	Intensity ($*10^{-21}$)^a	Broadening ^{b}	Shift ^{c}	Line Mixing ^{d}	Line Position(cm^{-1})	Intensity ($*10^{-21}$)^a	Broadening ^{b}	Shift ^{c}	Line Mixing ^{d}
P24	-24	4148.797701(3)	0.05562(5)	0.04936(6)	-0.00568(9)	—	4148.797954(3)	0.056428(6)	0.05320(2)	-0.00712(7)	—
P23	-23	4154.212515(2)	0.08296(5)	0.05127(5)	-0.00708(7)	0.00500(11)	4154.212570(2)	0.082687(5)	0.05051(7)	-0.00715(7)	0.0036.(10)
P22	-22	4159.560349(1)	0.12169(5)	0.05154(3)	-0.00510(5)	—	4159.560339(1)	0.12169(5)	0.05259(7)	-0.00508(4)	—
P21	-21	4164.841591(1)	0.17561(5)	0.05229(3)	-0.00631(4)	—	4164.841592(1)	0.17519(6)	0.05165(4)	-0.00632(3)	—
P20	-20	4170.055957(7)	0.24942(6)	0.05410(2)	-0.00559(3)	0.00400(4)	4170.055978(8)	0.24948(6)	0.05464(4)	-0.00562(2)	0.00326(2)
P19	-19	4175.203242(6)	0.34661(6)	0.05540(2)	-0.00588(2)	—	4175.203232(6)	0.34762(7)	0.05622(3)	-0.00552(2)	—
P18	-18	4180.283294(4)	0.47176(7)	0.05665(1)	-0.00523(2)	-0.00290(2)	4180.283311(5)	0.47487(8)	0.05864(3)	-0.00529(1)	-0.0029.(1)
P17	-17	4185.295948(4)	0.62358(7)	0.05727(1)	-0.00509(1)	-0.00120(2)	4185.295930(4)	0.62520(8)	0.05814(2)	-0.00502(1)	-0.00142(1)
P16	-16	4190.241177(3)	0.80694(8)	0.05823(1)	-0.00519(1)	-0.00030(1)	4190.241178(3)	0.80700(8)	0.05839(2)	-0.00521(1)	-0.00021(1)
P15	-15	4195.118770(3)	1.02600(9)	0.05945(1)	-0.00539(1)	0.00160(1)	4195.118804(3)	1.0262(10)	0.05948(1)	-0.00551(1)	0.00192(1)
P14	-14	4199.928473(2)	1.2680(10)	0.06030(1)	-0.00509(1)	0.00180(1)	4199.928482(3)	1.2696(11)	0.06065(1)	-0.00511(1)	0.00183(1)
P13	-13	4204.670247(2)	1.5421(12)	0.06194(1)	-0.00504(1)	0.00426(8)	4204.670258(2)	1.5439(13)	0.06222(1)	-0.00510(1)	0.00435(1)
P12	-12	4209.343926(2)	1.8218(14)	0.06294(1)	-0.00476(1)	0.00237(7)	4209.343933(2)	1.8249(15)	0.06328(1)	-0.00479(1)	0.00246(1)
P11	-11	4213.949398(2)	2.0992(16)	0.06419(1)	-0.00489(1)	0.00134(7)	4213.949409(2)	2.1039(17)	0.06477(1)	-0.00494(1)	0.00148(1)
P10	-10	4218.486418(2)	2.3506(18)	0.06514(1)	-0.00478(1)	-0.00008(6)	4218.486422(2)	2.3570(19)	0.06578(1)	-0.00482(1)	0.00001(1)
P9	-9	4222.954930(2)	2.5565(20)	0.06612(1)	-0.00471(1)	-0.00024(6)	4222.954944(2)	2.5626(21)	0.06667(1)	-0.00478(1)	0.00011(1)
P8	-8	4227.354735(2)	2.7074(21)	0.06701(1)	-0.00445(1)	-0.00062(6)	4227.354739(2)	2.7115(22)	0.06733(1)	-0.00447(1)	-0.00055(1)
P7	-7	4231.685712(2)	2.7574(21)	0.06847(1)	-0.00426(1)	-0.00124(6)	4231.685720(2)	2.7622(22)	0.06883(1)	-0.00428(1)	-0.00132(4)
P6	-6	4235.947732(2)	2.7110(20)	0.07006(1)	-0.00417(1)	-0.00101(6)	4235.947738(2)	2.7160(22)	0.07051(1)	-0.00421(1)	-0.00091(1)
P5	-5	4240.140616(2)	2.5388(19)	0.07237(1)	-0.00435(1)	0.00125(6)	4240.140622(2)	2.5428(20)	0.07275(1)	-0.00443(1)	0.00164(1)
P4	-4	4244.264210(2)	2.2484(17)	0.07481(1)	-0.00352(1)	-0.00157(7)	4244.264221(2)	2.2502(18)	0.07497(1)	-0.00357(1)	-0.00166(1)
P3	-3	4248.318375(2)	1.8338(14)	0.07770(1)	-0.00302(1)	-0.00506(9)	4248.318385(2)	1.8372(15)	0.07831(2)	-0.00304(1)	-0.00511(1)
P2	-2	4252.303020(3)	1.3035(11)	0.08117(1)	-0.00303(1)	-0.00470(1)	4252.303043(3)	1.3068(13)	0.08220(2)	-0.00313(1)	-0.00448(1)
P1	-1	4256.217921(4)	0.68228(9)	0.08682(2)	-0.00316(2)	-0.00200(2)	4256.217924(5)	0.68368(11)	0.08752(4)	-0.00320(2)	-0.00166(1)

Table 6-3. Retrieved experimental parameters in R-branch of CO-CO (2-0) spectra applying Voigt and SDV models. In this table, “a” is measured in [cm^{-1}/ (molecule cm^{-2})], “b, c” are coefficients measured in [cm^{-1} atm^{-1}] and “d”is in atm^{-1} at 296K.

		Retrieved parameters using Voigt model					Retrieved parameters using SDV model				
Line	m	Line Position(cm^{-1})	Intensity (*10^{-21})^a	Broadening ^{b}	Shift ^{c}	Line Mixing ^{d}	Line Position(cm^{-1})	Intensity (*10^{-21})^a	Broadening ^{b}	Shift ^{c}	Line Mixing ^{d}
R0	1	4263.837933(4)	0.70067(10)	0.08651(2)	-0.00297(2)	0.01010(2)	4263.837953(5)	0.70335(11)	0.08804(4)	-0.00300(2)	0.00969(1)
R1	2	4267.542850(2)	1.3858(12)	0.08198(1)	-0.00332(1)	0.00440(1)	4267.542862(3)	1.3894(14)	0.08305(2)	-0.00338(1)	0.00461(1)
R2	3	4271.177398(2)	2.0073(16)	0.07807(1)	-0.00332(1)	0.00296(8)	4271.177414(2)	2.0110(17)	0.07865(2)	-0.00337(1)	0.00306(0)
R3	4	4274.741512(2)	2.5353(20)	0.07537(1)	-0.00371(1)	0.00330(7)	4274.741519(2)	2.5406(21)	0.07602(1)	-0.00375(1)	0.00329(1)
R4	5	4278.235033(2)	2.9516(23)	0.07250(1)	-0.00371(1)	0.00204(6)	4278.235039(2)	2.9577(24)	0.07311(1)	-0.00374(1)	0.00215(0)
R5	6	4281.657811(2)	3.2489(26)	0.07021(1)	-0.00388(1)	0.00104(6)	4281.657821(2)	3.2551(27)	0.07076(1)	-0.00391(1)	0.00095(1)
R6	7	4285.009688(2)	3.4028(27)	0.06830(1)	-0.00401(1)	0.00096(5)	4285.009697(2)	3.4075(28)	0.06876(1)	-0.00407(1)	0.00094(1)
R7	8	4288.290550(1)	3.4359(28)	0.06693(1)	-0.00406(1)	0.00029(5)	4288.290557(2)	3.4415(29)	0.06746(1)	-0.00410(1)	0.00023(1)
R8	9	4291.500200(2)	3.3490(28)	0.06591(1)	-0.00392(1)	-0.00143(5)	4291.500209(2)	3.3555(28)	0.06662(1)	-0.00396(1)	-0.00131(1)
R9	10	4294.638542(2)	3.1766(26)	0.06491(1)	-0.00412(1)	-0.00094(6)	4294.638541(2)	3.1823(27)	0.06551(1)	-0.00412(1)	-0.00100(5)
R10	11	4297.705401(2)	2.9196(25)	0.06383(1)	-0.00406(1)	-0.00120(6)	4297.705416(2)	2.9236(26)	0.06424(1)	-0.00413(1)	-0.00110(1)
R11	12	4300.700641(2)	2.6153(22)	0.06276(1)	-0.00426(1)	-0.00275(7)	4300.700652(2)	2.6193(24)	0.06315(1)	-0.00432(1)	-0.00278(1)
R12	13	4303.624098(2)	2.2884(20)	0.06173(1)	-0.00437(1)	-0.00158(8)	4303.624100(2)	2.2919(21)	0.06214(1)	-0.00442(1)	-0.00148(1)
R13	14	4306.475682(2)	1.9495(18)	0.06072(1)	-0.00419(1)	-0.00235(9)	4306.475695(2)	1.9529(19)	0.06120(1)	-0.00420(1)	-0.00266(1)
R14	15	4309.255161(2)	1.6175(15)	0.05935(1)	-0.00439(1)	-0.00440(1)	4309.255175(2)	1.6205(17)	0.05982(2)	-0.00447(1)	-0.00424(1)
R15	16	4311.962439(2)	1.3148(13)	0.05804(1)	-0.00437(1)	-0.00400(1)	4311.962441(3)	1.3170(15)	0.05851(2)	-0.00434(1)	-0.00448(1)
R16	17	4314.597379(3)	1.0460(12)	0.05716(1)	-0.00428(1)	-0.00790(1)	4314.597390(3)	1.0493(13)	0.05809(2)	-0.00429(1)	-0.00817(1)
R17	18	4317.159797(3)	0.81218(10)	0.05583(1)	-0.00488(1)	-0.00250(2)	4317.159808(4)	0.81581(12)	0.05708(2)	-0.00490(1)	-0.00257(1)
R18	19	4319.649504(4)	0.61823(10)	0.05499(1)	-0.00441(2)	-0.00650(2)	4319.649495(5)	0.62026(11)	0.05586(3)	-0.00437(1)	-0.00702(1)
R19	20	4322.066588(5)	0.45889(9)	0.05337(2)	-0.00526(2)	-0.00140(3)	4322.066622(6)	0.45975(10)	0.05393(3)	-0.00540(2)	-0.00029(1)
R20	21	4324.410599(7)	0.33511(8)	0.05222(2)	-0.00463(3)	-0.00620(4)	4324.410613(8)	0.33516(9)	0.05210(3)	-0.00472(3)	-0.00540(4)
R21	22	4326.681547(9)	0.23923(8)	0.05093(3)	-0.00480(4)	—	4326.681617(1)	0.23934(9)	0.05100(4)	-0.00543(3)	—
R22	23	4328.879337(1)	0.16806(8)	0.05084(4)	-0.00512(5)	-0.00010(8)	4328.879332(1)	0.16865(9)	0.05165(8)	-0.00509(4)	-0.00013(1)
R23	24	4331.004092(2)	0.11634(8)	0.05065(5)	-0.00706(7)	-0.01220(12)	4331.004229(2)	0.11598(8)	0.04980(8)	-0.00738(5)	-0.01223(1)

Table 6-4. Retrieved experimental parameters in P-branch of CO-H_2 (2-0) spectra applying Voigt and SDV models. In this table, “a” is measured in [cm^{-1}/ (molecule cm^{-2})], “b, c” are coefficients measured in [cm^{-1} atm^{-1}] and “d”is in atm^{-1} at 296K.

		Retrieved parameters using Voigt model				Retrieved parameters using SDV model		
Line	m	Intensity (*10^{-21})^{a}	Broadening ^{b}	Shift ^{c}	Line Mixing ^{d}	Broadening ^{b}	Shift ^{c}	Line Mixing ^{d}
P24	-24	0.050960(22)	0.04360(4)	-0.0068(4)	—	0.04700(6)	-0.00830(1)	—
P23	-23	0.082276(24)	0.05560(3)	—	—	0.05490(4)	—	—
P22	-22	0.12477(25)	0.05780(2)	-0.00600(2)	—	0.05670(2)	-0.00600(2)	—
P21	-21	0.17422(25)	0.05700(2)	-0.00690(2)	0.0102(3)	0.05450(2)	-0.00700(1)	0.01120(3)
P20	-20	0.24618(26)	0.05670(1)	-0.00580(1)	—	0.05530(1)	-0.00580(1)	—
P19	-19	0.34190(27)	0.05720(1)	-0.00560(1)	—	0.05830(1)	-0.00660(1)	—
P18	-18	0.46923(28)	0.05940(1)	-0.00510(1)	—	0.05940(1)	-0.00510(1)	—
P17	-17	0.61705(29)	0.05920(1)	-0.00570(1)	0.0140(1)	0.05920(1)	-0.00570(1)	0.01390(8)
P16	-16	0.079954(30)	0.05889(4)	-0.00446(4)	0.0026(1)	0.05910(1)	-0.00450(2)	0.00236(1)
P15	-15	1.0191(31)	0.06007(4)	-0.00524(3)	0.0030(1)	0.05971(4)	-0.00524(3)	0.00297(5)
P14	-14	1.2647(32)	0.06132(3)	-0.00509(3)	0.0074(4)	0.06092(4)	-0.00509(3)	0.00740(4)
P13	-13	1.5398(34)	0.06135(3)	-0.00509(3)	0.0035(4)	0.06230(4)	-0.00511(2)	0.00340(1)
P12	-12	1.8158(35)	0.06075(2)	-0.00568(2)	0.0073(3)	0.06094(3)	-0.00563(2)	0.00720(1)
P11	-11	2.0951(37)	0.06157(2)	-0.00533(2)	0.0001(3)	0.06203(3)	-0.00525(2)	0.00001(2)
P10	-10	2.3454(38)	0.06205(2)	-0.00496(2)	-0.0009(3)	0.06246(3)	-0.00497(2)	-0.00112(1)
P9	-9	2.5547(39)	0.06238(2)	-0.00478(2)	-0.0003(2)	0.06327(3)	-0.00474(1)	-0.00018(2)
P8	-8	2.7004(40)	0.06324(2)	-0.00422(2)	-0.0019(2)	0.06354(3)	-0.00429(1)	-0.00187(1)
P7	-7	2.7577(41)	0.06399(2)	-0.00454(2)	-0.0035(2)	0.06466(3)	-0.00452(1)	-0.00347(1)
P6	-6	2.7042(42)	0.06454(2)	-0.00419(2)	-0.0053(2)	0.06486(3)	-0.00416(1)	-0.00535(2)
P5	-5	2.5366(42)	0.06614(2)	-0.00444(2)	-0.0023(3)	0.06656(4)	-0.00451(2)	-0.00178(1)
P4	-4	2.2345(41)	0.06736(3)	-0.00391(2)	-0.0064(3)	0.06789(4)	-0.00398(2)	-0.00641(1)
P3	-3	1.8211(41)	0.07003(3)	-0.00393(3)	0.0021(4)	0.07015(5)	-0.00359(2)	-0.00330(1)
P2	-2	1.2957(40)	0.07315(5)	-0.00339(4)	-0.0025(1)	0.07360(1)	-0.00340(2)	-0.00229(2)
P1	-1	0.67968(39)	0.07910(1)	-0.00160(1)	-0.0080(1)	0.07910(1)	-0.00160(1)	-0.00800(5)

Table 6-5. Retrieved experimental parameters in R-branch of CO-H_2 (2-0) spectra applying Voigt and SDV models. In this table, “a” is measured in [cm^{-1}/ (molecule cm^{-2})], “b, c” are coefficients measured in [cm^{-1} atm^{-1}] and “d”is in atm^{-1} at 296K.

		Retrieved parameters using Voigt model					Retrieved parameters using SDV model		
Line	m	Line Position(cm^{-1})	Intensity (*10^{-21})^a	Broadening ^{b}	Shift ^{c}	Line Mixing ^{d}	Broadening ^{b}	Shift ^{c}	Line Mixing ^{d}
R0	1	4263.83710(1)	0.71005(41)	0.08080(1)	-0.00270(2)	—	0.07950(1)	-0.00270(1)	—
R1	2	4267.54167(3)	1.3863(42)	0.07363(5)	-0.0018(10)	-0.0019(1)	0.07420(1)	-0.00200(3)	-0.00149(2)
R2	3	4271.17613(2)	2.0047(44)	0.07054(3)	-0.00243(7)	-0.0015(4)	0.07200(1)	-0.00240(2)	-0.00130(2)
R3	4	4274.74089(2)	2.5339(46)	0.06776(3)	-0.00399(6)	0.0014(3)	0.06828(4)	-0.00405(2)	0.00139(1)
R4	5	4278.23424(1)	2.9557(48)	0.06603(2)	-0.00336(5)	-0.0022(3)	0.06659(4)	-0.00341(2)	-0.00212(1)
R5	6	4281.65729(1)	3.2498(49)	0.06422(2)	-0.00448(5)	0.0029(2)	0.06449(3)	-0.00441(1)	0.00287(1)
R6	7	4285.00901(1)	3.4119(50)	0.06354(2)	-0.00410(4)	0.0037(2)	0.06359(3)	-0.00412(1)	0.00369(1)
R7	8	4288.28992(1)	3.4585(51)	0.06257(2)	-0.00432(4)	-0.0021(2)	0.06286(3)	-0.00431(1)	-0.00206(2)
R8	9	4291.49951(1)	3.3671(51)	0.06172(2)	-0.00378(4)	-0.0011(2)	0.06202(3)	-0.00369(1)	-0.00118(2)
R9	10	4294.63773(1)	3.1748(50)	0.06224(2)	-0.00390(5)	0.0015(2)	0.06290(3)	-0.00388(2)	0.00143(1)
R10	11	4297.70463(1)	2.9220(49)	0.06184(2)	-0.00384(5)	-0.0037(3)	0.06262(3)	-0.00386(2)	-0.00361(1)
R11	12	4300.70002(1)	2.6062(48)	0.06070(2)	-0.00388(5)	-0.0066(3)	0.06138(4)	-0.00380(2)	-0.00679(1)
R12	13	4303.62341(2)	2.2756(46)	0.06052(3)	-0.00421(6)	-0.0043(3)	0.06150(4)	-0.00432(2)	-0.00445(1)
R13	14	4309.25426(2)	1.9410(45)	0.06061(3)	-0.00424(6)	-0.0035(4)	0.06148(4)	-0.00419(2)	-0.00352(2)
R14	15	4311.96210(2)	1.6077(44)	0.05920(3)	-0.00377(7)	-0.0008(5)	0.06010(1)	-0.00377(2)	-0.00083(1)
R15	16	4314.59646(3)	1.3104(42)	0.05906(4)	-0.00527(8)	-0.0030(6)	0.05906(5)	-0.00528(4)	-0.00290(5)
R16	17	4317.15939(4)	1.0415(41)	0.05856(5)	-0.00340(1)	-0.0098(1)	0.05860(1)	-0.00335(4)	-0.01020(7)
R17	18	4319.64929(5)	8.0755(41)	0.05860(1)	-0.00560(1)	0.0055(1)	0.06060(1)	-0.00523(3)	-0.00342(5)
R18	19	4322.06620(1)	6.1879(39)	0.05620(1)	-0.00510(2)	—	0.05500(1)	-0.00505(1)	—
R19	20	—	4.5876(40)	0.05910(1)	-0.00560(2)	-0.0022(2)	0.06210(2)	-0.00567(4)	-0.0022.(3)
R20	21	—	3.2656(38)	0.05410(1)	—	-0.0155(2)	0.05290(1)	—	-0.01600(2)
R21	22	—	2.3293(37)	0.05350(2)	—	—	0.05220(2)	—	—
R22	23	—	1.6305(37)	0.05040(2)	—	—	0.05010(2)	—	—
R23	24	—	1.1775(39)	0.05210(3)	—	-0.0175(6)			

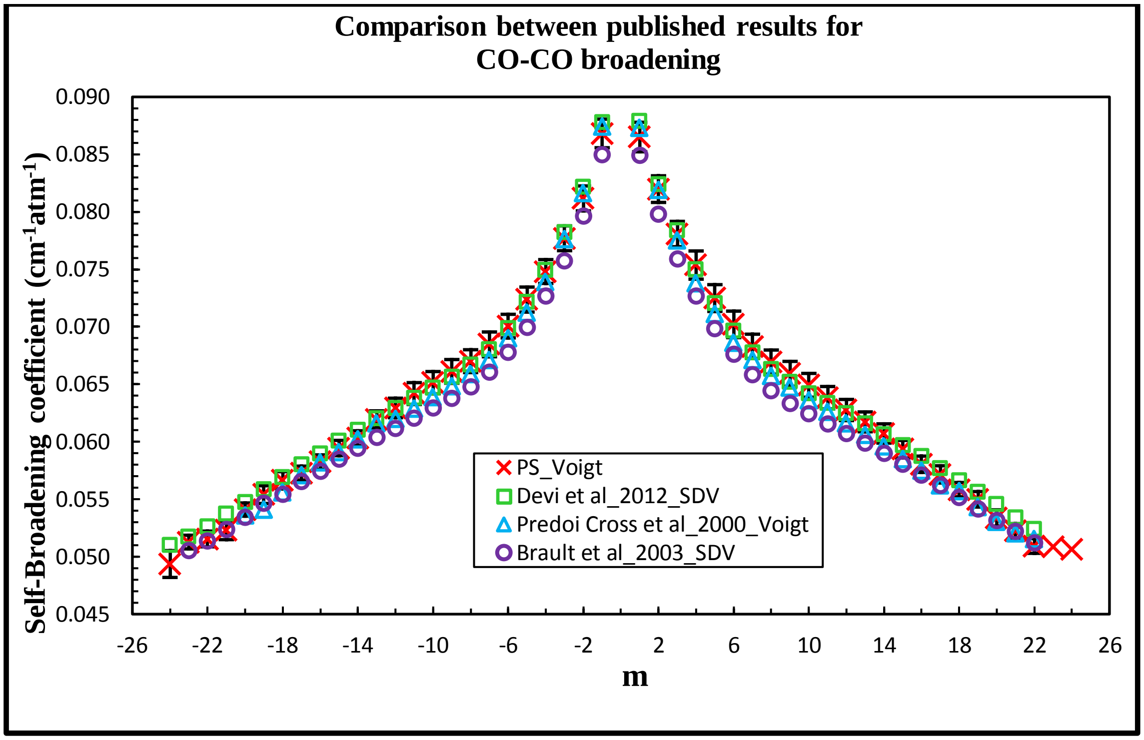

Figure 6.4. Measured Lorentz half-width of CO-CO present study (PS) using Voigt model and its comparison with three other similar studies.

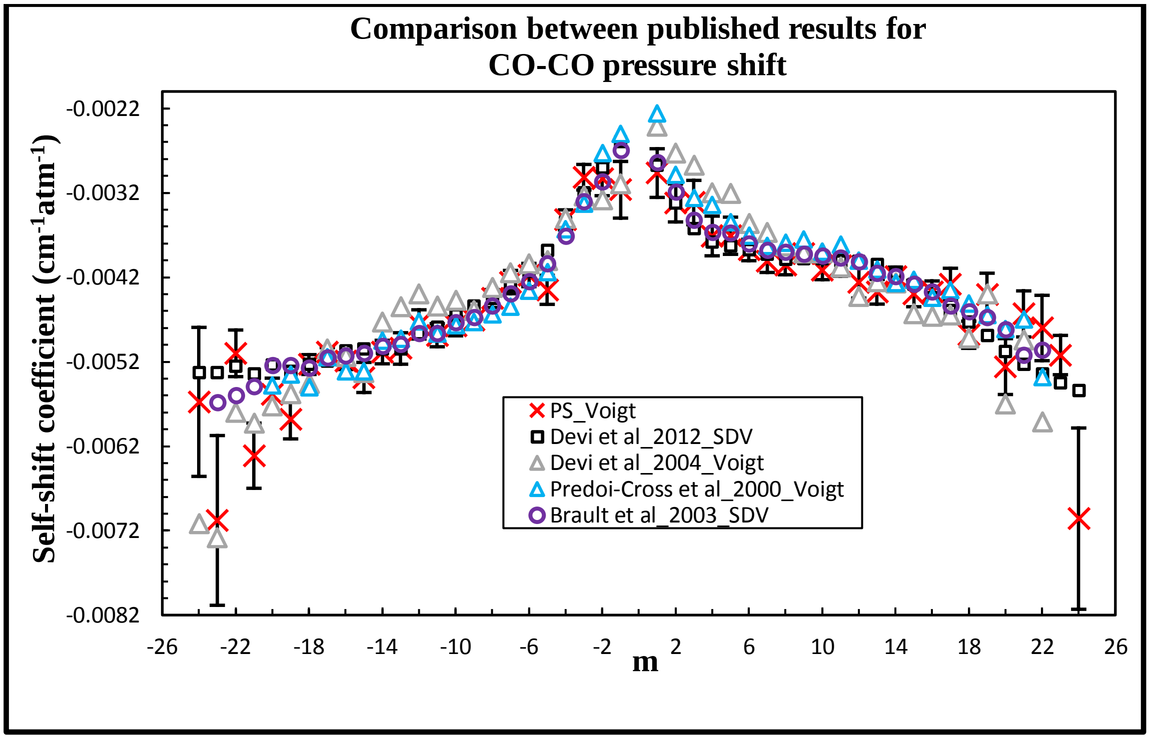

Figure 6.5. Measured collisional induced shift of CO-CO present study (PS) using Voigt model and its comparison with other similar studies.

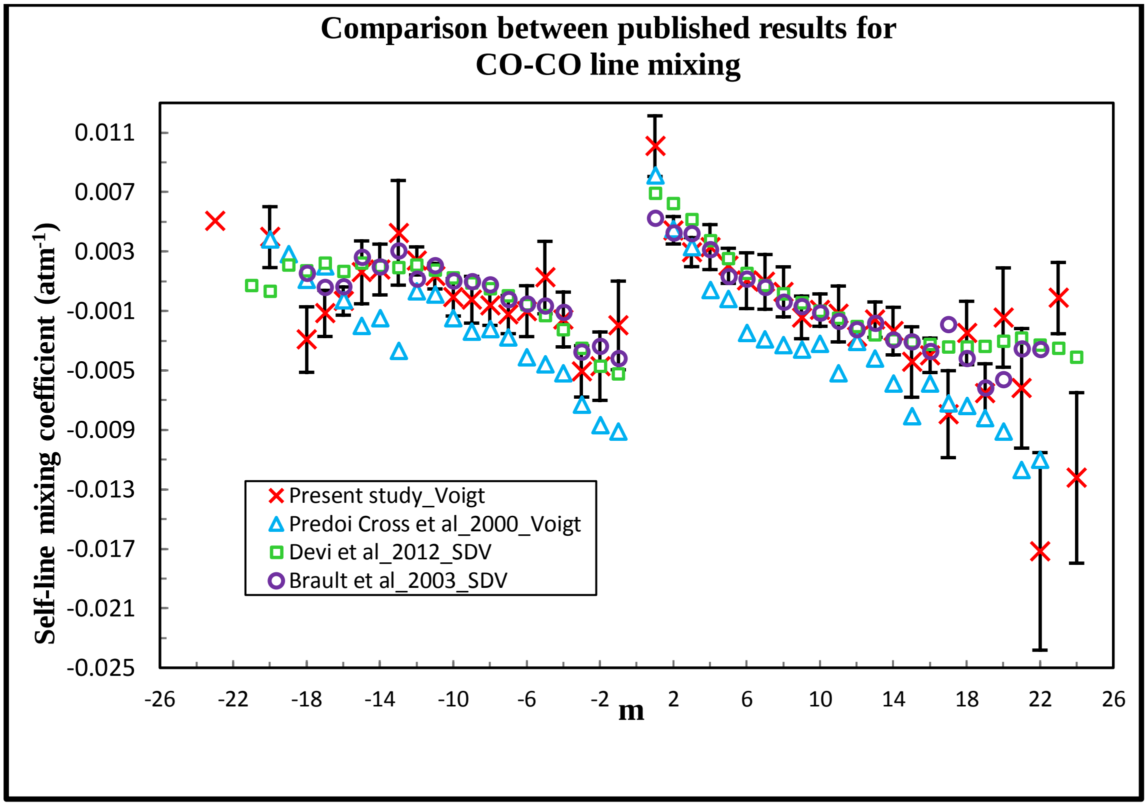

Figure 6.6. Measured coupled line mixing of CO-CO present study (PS) using Voigt model and its comparison with other similar studies.

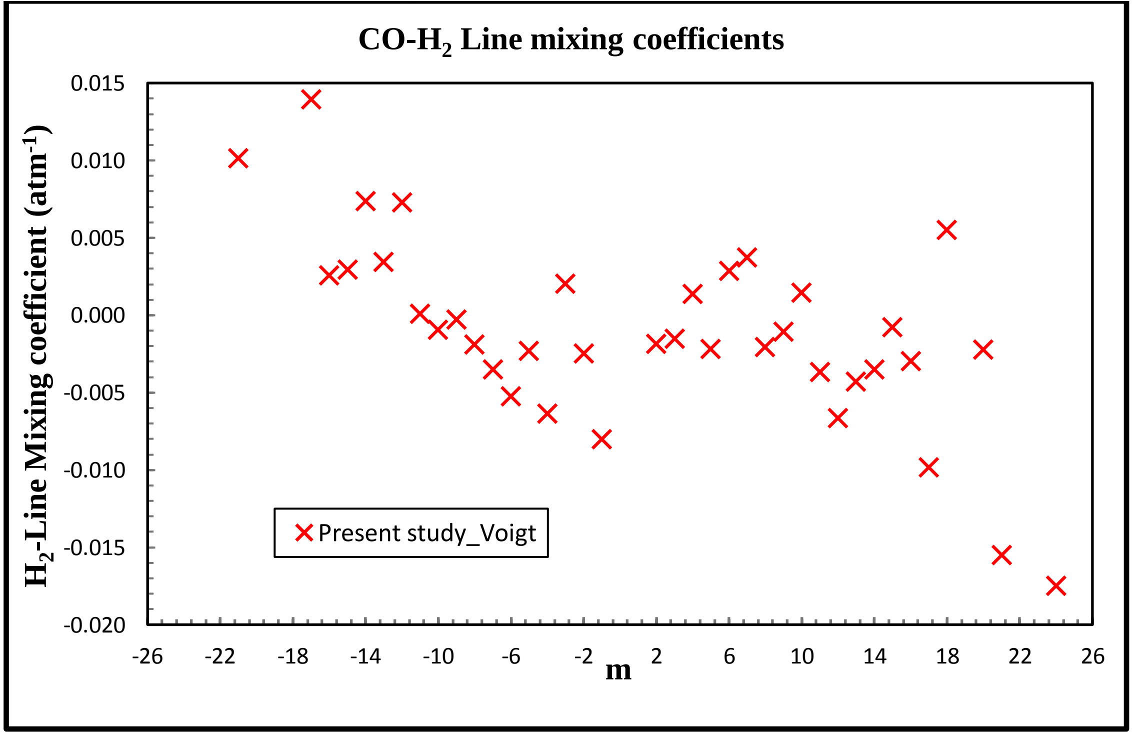

Figure 6.7. Measured coupled line mixing of CO-H_2 present study (PS) using Voigt model.

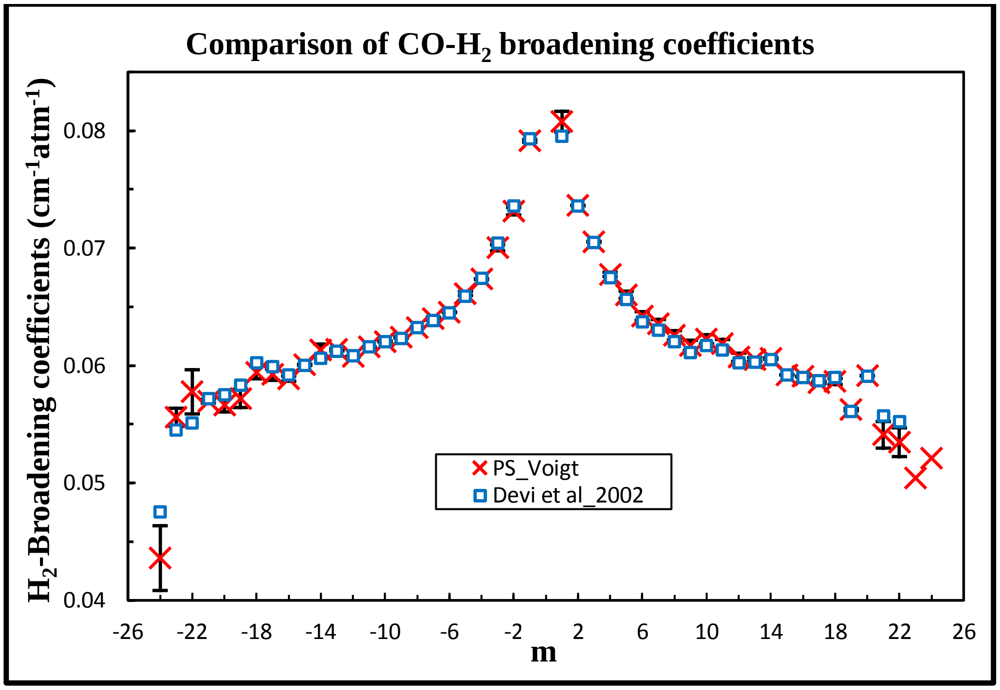

Figure 6.8. Measured Lorenz half-width of CO-H_2 present study (PS) using Voigt model and its comparison with literature.

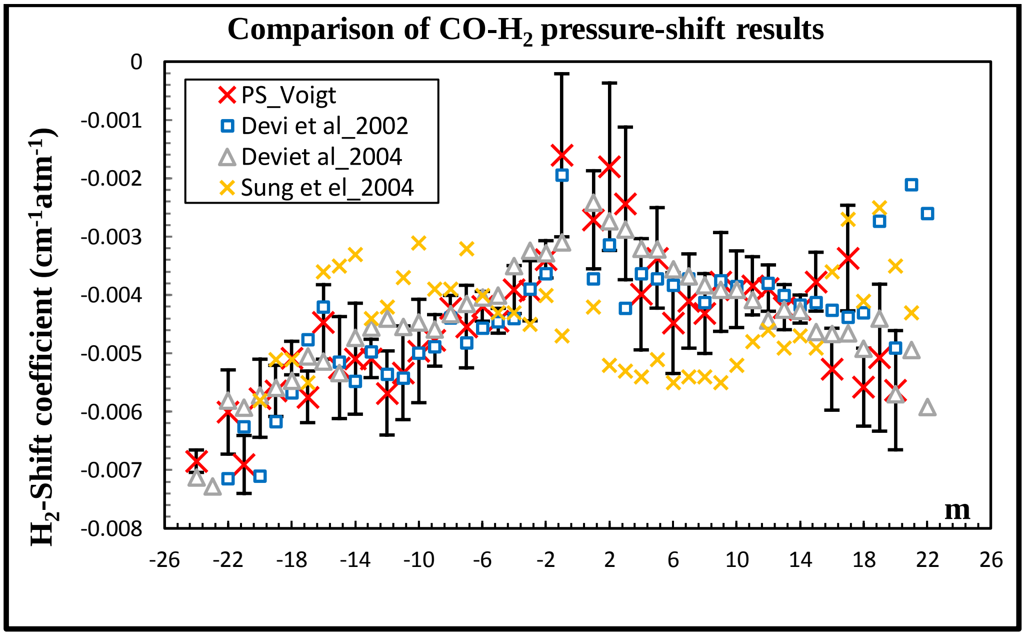

Figure 6.9. Measured pressure induced shift of CO-H_2 present study (PS) using Voigt model and its comparison with literature.

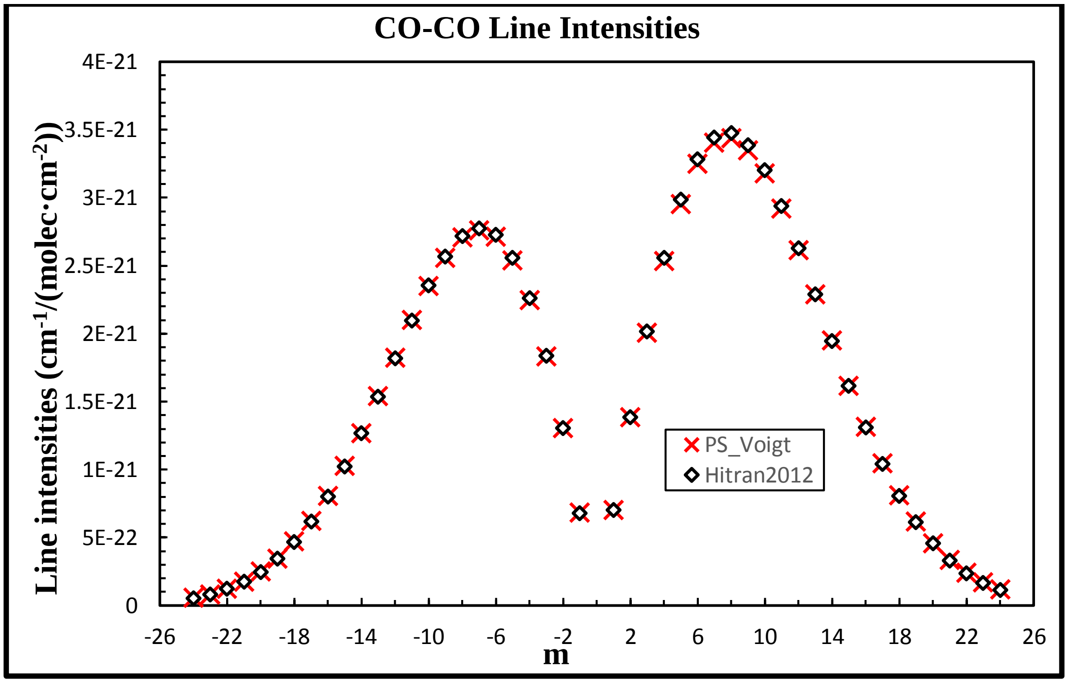

Figure 6.10. Measured line intensity of CO-CO present study (PS) using Voigt model and its comparison with HITRAN data base [5].

On the other hand, the off-diagonal elements of this matrix incorporates the elements that can be used to obtain the Line Mixing (line coupling) of the spectral lines. For simplicity, consider a simplest system of two transitions as depicted in Fig. 6.11.

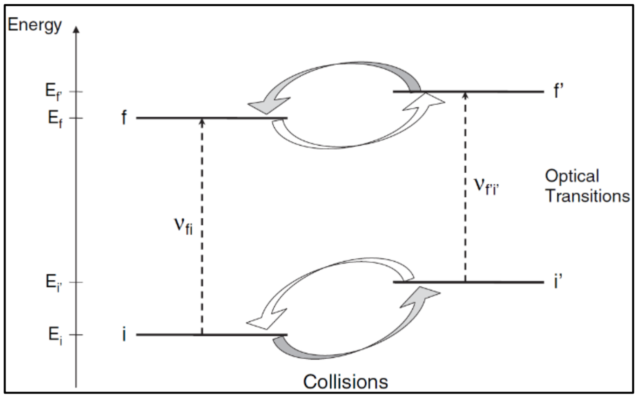

Figure 6.11. Schematic view of the two transitions causing a line coupling (intensity transition) [96].

Due to this perturbation of energy states caused by collisions, two adjacent line centers (energy gaps) become very close to each other. If the transitions $i \rightarrow$

f and $i' \rightarrow f'$ are shown by j and k, respectively, the relaxation matrix can be written by the following expression [119]:

$$\begin{bmatrix} W_{jj} & W_{jk} \\ W_{kj} & W_{kk} \end{bmatrix} \tag{6.2}$$

The obstacle that one needs to tackle is the lack of enough information of this relaxation matrix. The size of this matrix is n*n which n is the number of transitions (in the present study of CO, P and R branches totally 48 transitions). The diagonal elements which includes the broadening and shift parameters can be easily measured by experiment. However, there are several semi-empirical approaches that can estimate the off-diagonal elements. Among all of these scaling laws, we only limit our discussion to two of them namely, Exponential Power Gap (EPG) and Modified Exponential Gap scaling laws (MEGL) [96, 120].

EPG scaling law describes a collisional transfer rate, k_{jk}, in which the rate from lower to higher rotational states, $j \rightarrow k$, can be given by the following formula:

$$k_{jk} = a\left[\frac{|\Delta E_{j,k}|}{B_0}\right]^{-b} \exp\left(\frac{-c|\Delta E_{j,k}|}{k_B T}\right) \tag{6.3}$$

in which, B_0 is the rotational constant related to the vibrational level, $\Delta E_{j,k}$ is the energy gap between each two rotational transitions and a, b and c are the adjustable values that need to be optimized by fitting. A detailed balance is required to link the transfer rate from rotational level j to k (and vice versa) by the following equation:

$$k_{jk} = \left(\frac{2J_k+1}{2J_j+1}\right) \exp\left(\frac{\Delta E_{j,k}}{k_B T}\right) k_{kj} \tag{6.4}$$

Finally, to link the diagonal to off-diagonal elements the following summation rule must be met:

$$W_{kk} = \frac{1}{2}\left[\sum_{j>k} k_{jk}\right] + \frac{1}{2}\left[\sum_{k<j} k_{kj}\right] \tag{6.5}$$

In the case of MEGL, one more adjustable parameter is added to make the fitting easier. The collisional transfer rate accomplished by this law is given by:

$$k_{jk} = a_1 \left[\frac{1+a_2 E_j}{1+a_3 E_j}\right]^2 \exp\left(-a_4 \left|\Delta E_{j,k}\right|\right) \tag{6.6}$$

In the above expression, a_1, a_2, a_3 and a_4 are the adjustable parameters that need to be optimized and determined by fitting. $\Delta E_{j,k}$ is the energy difference between each two rotational levels. Moreover, $W_{jk} = -\beta k_{jk}$ should be satisfied during the fit, and β needs to be optimized. In the present study, β was determined to be 0.56 [8].

Obtained off-diagonal elements from two mentioned scaling laws, EPG and MEGL, must be substituted in the following famous first order line mixing (also known as Rosenkranz line mixing [121]) expression to retrieve the weak line mixing coefficients:

$$Y_k^0(T) = 2\sum_{j\neq k} \frac{d_j}{d_k} \frac{W_{jk}}{v_k - v_j} \tag{6.7}$$

$Y_k^0(T)$ is the first order line mixing coefficients between each two transitions. It is also worth noting that Rosenkranz line mixing works well if the energy gaps are well distinctive from each other or in the other words spectral lines are well separated enough. This theory can accurately enough estimate the line mixing values especially in the P and R branch regions of the light molecules. However, it is suggested to use the second order approximation for generating the line mixing of transitions located in Q branches (see page 161 of Ref. [96]). There are three types of dipole moment; the electric dipole, magnetic-dipole (such as oxygen) and also electric quadrupole dipole moments (nitrogen and some oxygen transitions). The CO molecule possess the electrical dipole moment and expression to calculate the electrical dipole moment for CO is described in details in Ref. [122] (see page 151).The comparisons of results are given through Fig.6.12 to 6.15.

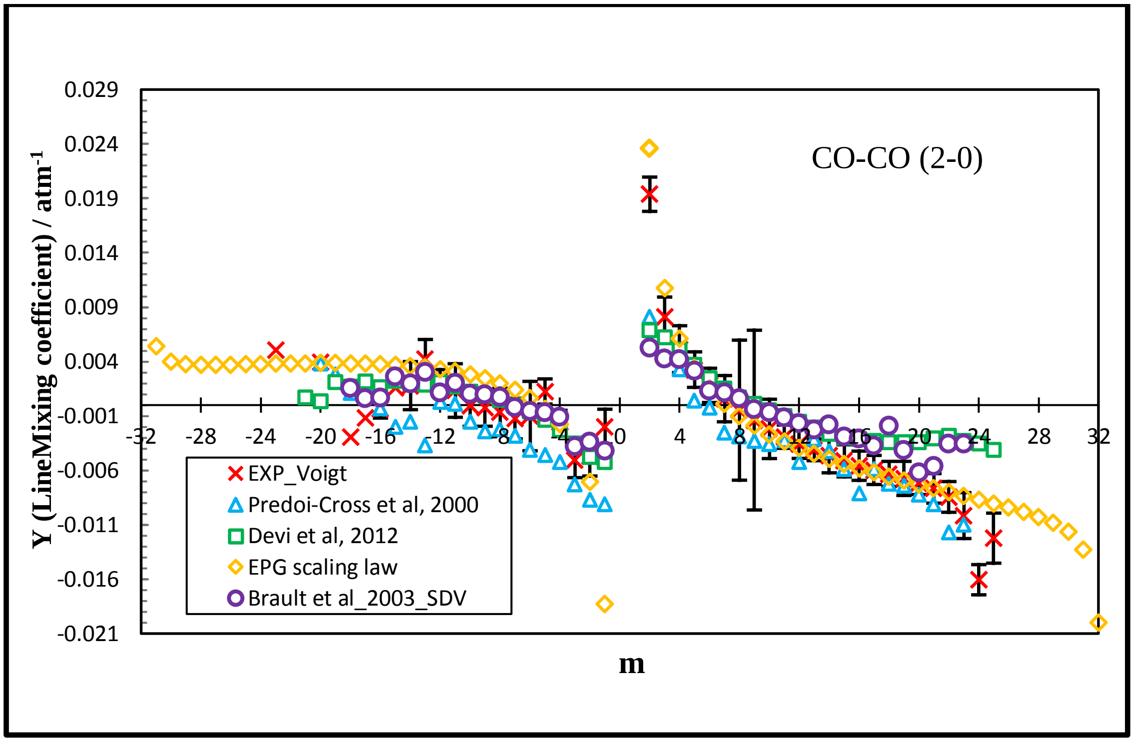

Figure 6.12. Measured and semi-empirical calculated line mixing coefficients of CO-CO applying EPG method and its comparison with literature.

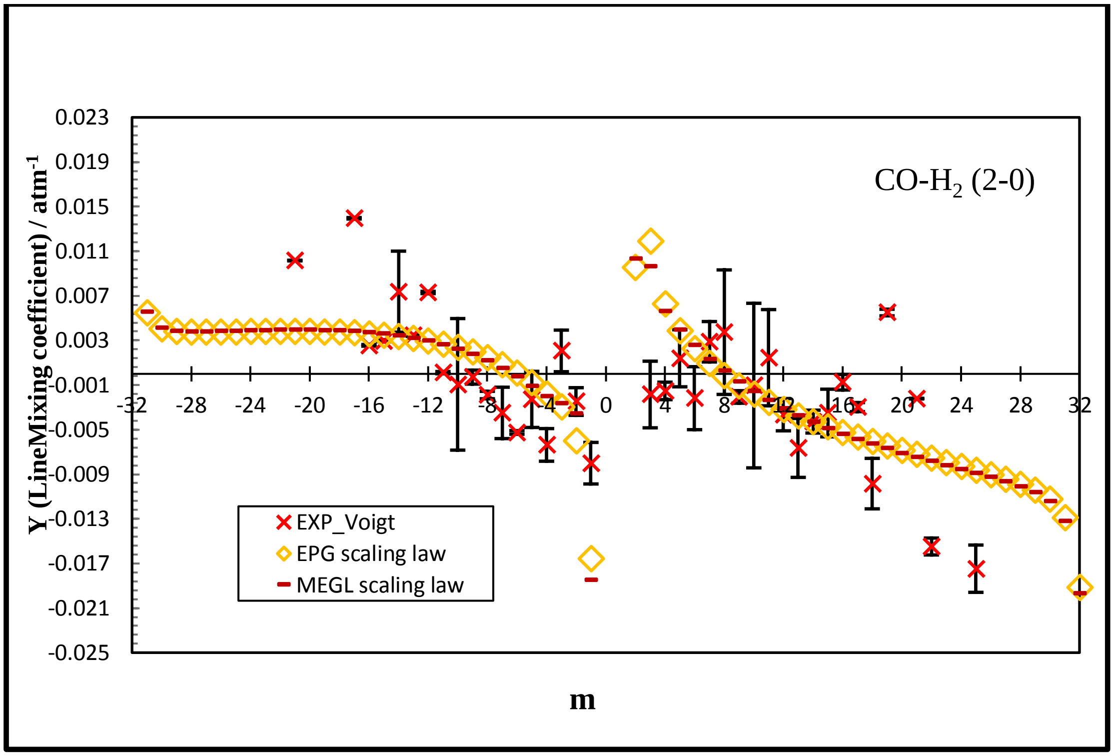

Figure 6.13. Measured and semi-empirical calculated line mixing coefficients of CO-H_2 applying EPG and MEGL methods.

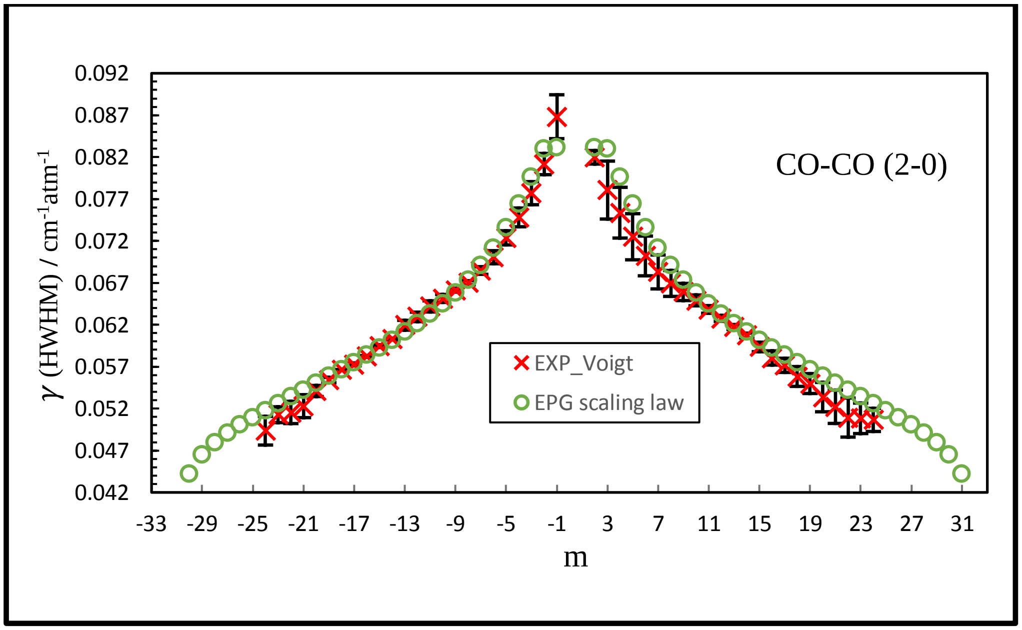

Figure 6.14. Measured and semi-empirical calculated broadening coefficients (HWHM) of CO-CO applying EPG.

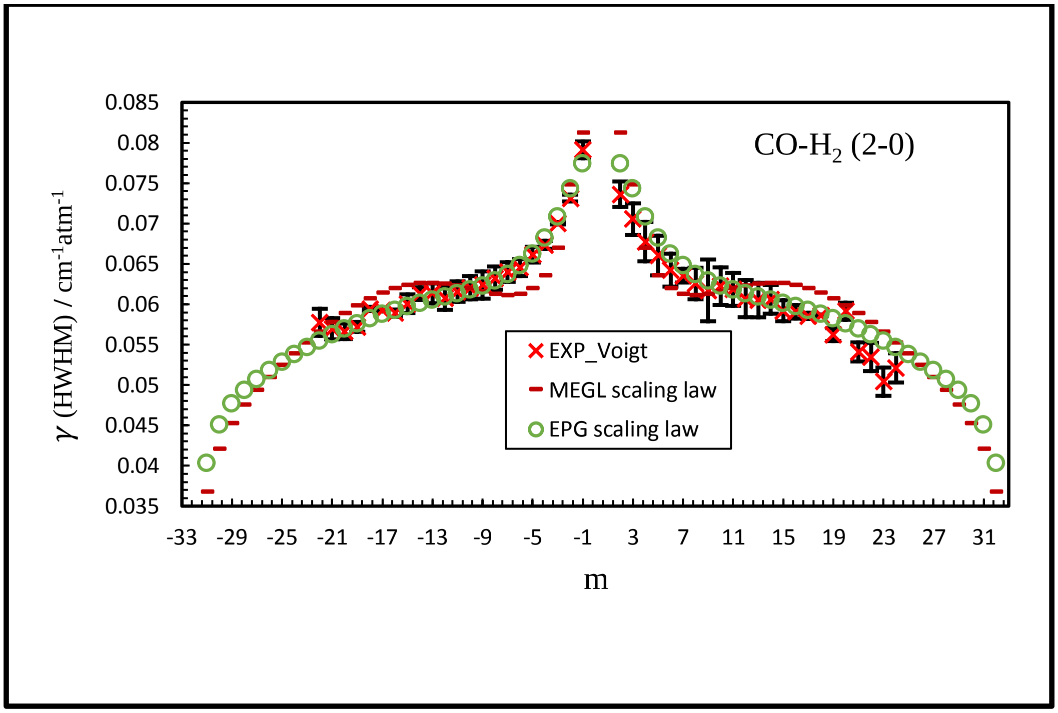

Figure 6.15. Measured and semi-empirical calculated broadening coefficients (HWHM) of CO-H_2 applying EPG and MEGL methods.

Table 6-6. Optimized adjustable parameters of EPG and MEGL techniques.

	EPG					MEGL	
	CO-CO		CO-H_2			CO-H_2	
Constants	P and R	Errors (*10^{-8})	P and R	Errors (*10^{-8})	Constants	P and R	Errors (*10^{-8})
a	0.04555	1.3094	0.02031	0.61454	a_1	1.2643	12.107
b	0.4198	7.2185	0.2304	7.3102	a_2	0.4323	2.1231
c	1.1063	23.835	1.1903	23.982	a_3	5.075	516.40
					a_4	1.3828	8.1937

Table 6-7. Calculated Lorentzian half-width and line mixing coefficients belonging to P-Branch employing EPG and MEGL methods.

		CO-CO		CO-H_2			
		Broadening HWHM ($cm^{-1}atm^{-1}$)	Line Mixing (atm^{-1})	Broadening HWHM ($cm^{-1}atm^{-1}$)		Line Mixing (atm^{-1})	
Lines	m	EPG	EPG	MEGL	EPG	MEGL	EPG
P(31)	-31	0.039533	0.005436	0.036784	0.040285	0.005576	0.005462
P(30)	-30	0.044195	0.003989	0.042087	0.045038	0.004107	0.004048
P(29)	-29	0.046493	0.003743	0.045269	0.047639	0.003814	0.003776
P(28)	-28	0.047963	0.003700	0.047517	0.049370	0.003759	0.003717
P(27)	-27	0.049085	0.003709	0.049341	0.050699	0.003769	0.003717
P(26)	-26	0.050047	0.003735	0.050963	0.051823	0.003800	0.003735
P(25)	-25	0.050931	0.003765	0.052474	0.052829	0.003835	0.003756
P(24)	-24	0.051776	0.003795	0.053909	0.053758	0.003869	0.003776
P(23)	-23	0.052600	0.003820	0.055276	0.054626	0.003896	0.003791
P(22)	-22	0.053414	0.003841	0.056569	0.055441	0.003917	0.003799
P(21)	-21	0.054223	0.003856	0.057777	0.056204	0.003928	0.003800
P(20)	-20	0.055033	0.003862	0.058883	0.056917	0.003931	0.003795
P(19)	-19	0.055846	0.003858	0.059873	0.057577	0.003902	0.003762
P(18)	-18	0.056668	0.003842	0.060729	0.058186	0.003859	0.003718
P(17)	-17	0.057502	0.003812	0.061438	0.058744	0.003802	0.003665
P(16)	-16	0.058356	0.003764	0.061987	0.059253	0.003705	0.003579
P(15)	-15	0.059235	0.003697	0.062369	0.059719	0.003585	0.003476
P(14)	-14	0.060151	0.003602	0.062582	0.060148	0.003423	0.003340
P(13)	-13	0.061115	0.003477	0.062629	0.060551	0.003211	0.003162
P(12)	-12	0.062143	0.003314	0.062525	0.060943	0.002945	0.002941
P(11)	-11	0.063253	0.003102	0.062292	0.061344	0.002620	0.002669
P(10)	-10	0.064470	0.002828	0.061970	0.061781	0.002233	0.002344
P(9)	-9	0.065825	0.002478	0.061613	0.062289	0.001765	0.001946
P(8)	-8	0.067357	0.002026	0.061298	0.062916	0.001194	0.001444
P(7)	-7	0.069115	0.001440	0.061135	0.063722	0.000516	0.000827
P(6)	-6	0.071159	0.000671	0.061279	0.064790	-0.000260	0.000088
P(5)	-5	0.073561	-0.000359	0.061965	0.066229	-0.001130	-0.000800
P(4)	-4	0.076389	-0.001774	0.063589	0.068183	-0.002030	-0.001850
P(3)	-3	0.079648	-0.003809	0.066978	0.070835	-0.002660	-0.002990
P(2)	-2	0.082958	-0.007042	0.074791	0.074330	-0.003560	-0.006020
P(1)	-1	0.083121	-0.018303	0.081274	0.077387	-0.018510	-0.016550

Table 6-8. Calculated Lorentzian half-width and line mixing coefficients belonging to R-Branch employing EPG and MEGL methods.

		CO-CO		CO-H_2			
		Broadening HWHM ($cm^{-1}atm^{-1}$)	Line Mixing (atm^{-1})	Broadening HWHM ($cm^{-1}atm^{-1}$)		Line Mixing (atm^{-1})	
Lines	m	EPG	EPG	MEGL	EPG	MEGL	EPG
R(1)	2	0.083121	0.023563	0.081274	0.077387	0.010326	0.009536
R(2)	3	0.082958	0.010785	0.074791	0.074330	0.009642	0.011915
R(3)	4	0.079648	0.006141	0.066978	0.070835	0.005601	0.006245
R(4)	5	0.076389	0.003420	0.063589	0.068183	0.003932	0.003878
R(5)	6	0.073561	0.001545	0.061965	0.066229	0.002544	0.002235
R(6)	7	0.071159	0.000131	0.061279	0.064790	0.001327	0.000942
R(7)	8	0.069115	-0.000990	0.061135	0.063722	0.000241	-0.000130
R(8)	9	0.067357	-0.001890	0.061298	0.062916	-0.000730	-0.001050
R(9)	10	0.065825	-0.002670	0.061613	0.062289	-0.001590	-0.001840
R(10)	11	0.064470	-0.003350	0.061970	0.061781	-0.002380	-0.002560
R(11)	12	0.063253	-0.003930	0.062292	0.061344	-0.003110	-0.003200
R(12)	13	0.062143	-0.004440	0.062525	0.060943	-0.003750	-0.003770
R(13)	14	0.061115	-0.004920	0.062629	0.060551	-0.004330	-0.004290
R(14)	15	0.060151	-0.005380	0.062582	0.060148	-0.004870	-0.004770
R(15)	16	0.059235	-0.005790	0.062369	0.059719	-0.005390	-0.005240
R(16)	17	0.058356	-0.006170	0.061987	0.059253	-0.005860	-0.005670
R(17)	18	0.057502	-0.006550	0.061438	0.058744	-0.006280	-0.006060
R(18)	19	0.056668	-0.006930	0.060729	0.058186	-0.006700	-0.006460
R(19)	20	0.055846	-0.007270	0.059873	0.057577	-0.007110	-0.006850
R(20)	21	0.055033	-0.007630	0.058883	0.056917	-0.007470	-0.007210
R(21)	22	0.054223	-0.007990	0.057777	0.056204	-0.007840	-0.007580
R(22)	23	0.053414	-0.008320	0.056569	0.055441	-0.008220	-0.007960
R(23)	24	0.052600	-0.008680	0.055276	0.054626	-0.008560	-0.008310
R(24)	25	0.051776	-0.009040	0.053909	0.053758	-0.008910	-0.008670
R(25)	26	0.050931	-0.009420	0.052474	0.052829	-0.009270	-0.009050
R(26)	27	0.050047	-0.009830	0.050963	0.051823	-0.009660	-0.009450
R(27)	28	0.049085	-0.010280	0.049341	0.050699	-0.010090	-0.009900
R(28)	29	0.047963	-0.010830	0.047517	0.049370	-0.010630	-0.010450
R(29)	30	0.046493	-0.011630	0.045269	0.047639	-0.011440	-0.011250
R(30)	31	0.044195	-0.013290	0.042087	0.045038	-0.013210	-0.012920
R(31)	32	0.039533	-0.019990	0.036784	0.040285	-0.019690	-0.019160

In this chapter, experimental results of self- and H_2- Lorentz half width, pressure induced shift parameters as well as other coefficients, such as line centers, line intensities and line mixing parameters were investigated for transitions in the first overtone (2-0) of carbon monoxide for 48 transitions (P(24) to R(23)). Two line shape functions, Voigt and speed dependent Voigt models were implemented to obtain the spectroscopic results. Due to the weak transitions located in the first overtone band of CO, no trend for speed dependency was observed.

Experimental results of broadening coefficients and electrical dipole moments provided in this band were used as inputs for two semi-empirical scaling laws described earlier (EPG and MEGL) to produce the first order line mixing coefficients. Table 6-6 to 6-8 represent the calculated values. The correctness and accuracy of broadening and line mixing parameters can be investigated by comparing to the experimental broadening coefficients. As it is clear from Figs. 6.14, the MEGL semi-empirical broadening coefficients between J=3 to J=20 are not in good agreements with experimental broadening coefficients in the case of CO-H_2 study. On the other hand, the EPG semi-empirical broadening coefficients are in good agreements with experimental coefficients in both CO-CO and CO-H_2 studies. This way of comparison can help us to examine the model and trust the semi-empirical line mixing coefficients.

7. Conclusions and Directions for Future Studies

The purpose of the spectroscopic studies presented here is the improvement of line shape parameters for selected molecules via a combination of spectroscopic instrumentation and analysis techniques, theoretical approximations and developed spectroscopic software. Our objective has been to offer sets of parameters that may be considered for inclusion in the present databases, such as HITRAN (acronym for HIgh resolution TRAnsmission) and GIESA (acronym for Gestion et Etude des Informations Spectroscopiques Atmosphériques) [4-6].

Chapter 1 starts with a brief presentation of the two spectroscopic techniques used in this study: laser spectroscopy and Fourier transform spectroscopy. A summary literature review of relevant spectroscopic studies on acetylene (C_2H_2), carbon monoxide (CO) and deuterium cyanide (DCN) is also presented in the Table 1-1 and 1-2. Chapter 2 outlines the quantum mechanics principles that govern the ro-vibrational spectroscopy in linear molecules. In addition, the origin of line shapes and associated line parameters are included in this chapter. Chapter 3 focuses on a description of the experimental setups used, such as a tunable diode laser spectrometer and two Fourier transform spectrometers used to record the absorption/emission spectra used in this thesis. Furthermore, detailed descriptions of the software used to retrieve line parameters (Labfit) are presented as well as the software called SyMath that blends in quantum calculations with spectral analysis for assignment work.

Chapter 4 reports the experimental Lorentz half width and collisional pressure shift coefficients of acetylene (C_2H_2) diluted by carbon dioxide (CO_2) in the R- branch of vibrational band v_1+v_3 located in the 6471 - 6617 cm^{-1} region along with their temperature dependency values. Spectra were recorded over a broad range of temperatures and pressures from 216 to 333 K and 50 Torr to 500 Torr, respectively. The data analysis was carried out using the conventional Voigt line shape model. Broadening parameters (HWHM) in the v_1+v_3 are compared with those reported by Martin *et al.* [48] in Fig 4.6. The comparison illustrates a good agreement between two studies especially at higher *J* values.

Three suggestions can be made to achieve improvements in this study. First, it is better to refit the spectra using Labfit software applied in the CO-CO and CO-H_2 study (see chapter 6). This software allows user to fit all the transitions simultaneously. This feature not only enables us to implement the line mixing effect easily but also to fit all the available spectra (all pressures and temperatures).

Secondly, due to having access to intermediate pressure of spectra, there is a possibility that Dicke narrowing effect can be observed within in this region meaning that spectral line shapes tend to be narrower than Voigt model suggests. This can be resolved by applying Galatry and Rautian-Sobelman profiles or speed dependence Voigt model since it also introduces narrower line shapes than Voigt profile by considering the speed dependency of the absorbers. Thirdly, two semi-empirical methods called Exponential Power Gap (EPG) and Modified Exponential Gap Law scaling laws can be accomplished to retrieve modified broadening coefficients as well as new line mixing values.

Chapter 5 focuses on the retrieval of ro-vibrational parameters corresponding to the vibrational levels up 5 (*v*=5) of $D^{12}C^{14}N$ in the region of 450 to 850 cm^{-1}. Self-calibration using Hydrogen Cyanide (HCN) as an impurity in the sample helped us to achieve better results compared with previous publication [58]. Next step that one can take along with this study is to obtain the line intensities of mentioned vibrational bands either using Symath or any other available spectroscopic analysis softwares.

Chapter 6 introduces an experimental and semi-empirical approaches to perform the data analysis of CO-CO and CO-H_2 study. The self- and foreign- Lorentz half width, induced pressure shift parameters along with line centers and intensities, and line mixing coefficients in the first overtone (2-0) of CO have reported. Two line shape functions, Voigt and speed dependent Voigt (SDV) models were employed. More improvement was observed applying the SDV model. In addition, EPG and MEGL were examined using the experimental results as input for these two scaling laws. MEGL was not able to reproduce the real broadening coefficients of line shapes very accurately.

One suggestion about the CO-H_2 study that can be made is to record the spectra in the first overtone band at various temperatures in order to find the pressure and temperature dependency of H_2- shift and-broadening coefficients. This is highly recommended since there is only one study in the literature [82] and these results needed to be validated. Temperature dependency coefficients are needed for the atmospheric study of planets Jupiter and Saturn (CO is the minor constituent, H_2 is the predominate constituent) since their temperature ranges are approximately between 145-277 K for Jupiter and 95-330 K for Saturn [123]. Another suggestion that can be made to obtain the semi-empirical line mixing coefficients is to use the Energy Corrected Sudden (ECS) [96] which is based upon the transfer of angular momentum during molecular collisions.

References

[1] F.A. Miller, *The History of Spectroscopy as Illustrated on Stamps*, Appl. Spectrosc., **37** (1983) 219-225.

[2] H. John Frederick William, *Catalogue of Nebulae and Clusters of Stars*, Philosophical Transactions of the Royal Society of London, **154** (1864) 1-137.

[3] G.R. Gordon, The LASER, Light Amplification by Stimulated Emission of Radiation, in: The Ann Arbor Conference on Optical Pumping, the University of Michigan, 1959, pp. 128.

[4] http://hitran.iao.ru.

[5] http://hitran.org.

[6] http://ether.ipsl.jussieu.fr/etherTypo/index.php?id=976&L=0.

[7] K.F. Renk, Basics of Laser Physics: For Students of Science and Engineering Springer, 2012.

[8] C. Povey, High Resolution Spectroscopy and Applications, in: Physics and Astronomy Department, University of Lethbridge, Canada, 2013.

[9] W.D. Perkins, *Fourier transform-infrared spectroscopy: Part l. Instrumentation*, Journal of chemical education, **63** (1986) A5.

[10] P.R. Griffiths, J.A. De Haseth, Fourier Transform Infrared Spectrometry, 2nd Edition ed., Wiley, United State, 2007.

[11] B.C. Smith, Fundamentals of Fourier Transform Infrared Spectroscopy CRC Press, New York, 1995.

[12] http://cdn.intechopen.com/pdfs-wm/37068.pdf.

[13] E. Davy, Notice of a new gaseous bicarburet of hydrogen, in, 1836, pp. 62-63.

[14] Bertholet, Tetra-Carbon Hydride and its Derivatives, in, 1860, pp. 805-808.

[15] R.A. Whitby, E.R. Altwicker, *Acetylene in the Atmosphere: Sources, Representative Ambient Concentrations And Ratios to Other Hydrocarbons,*, Atmospheric Environment, **12** (1977) 1289-1296.

[16] M.J.M. Horn. D, Winer. A. M, Herr. K.C, Pimentel G.C., *The composition of the Martian atmosphere: Minor constituents*, Icarus **16** (1972) 543-556.

[17] R.J. Vervack, B.R. Sandel, D.F. Strobel, *New perspectives on Titan's upper atmosphere from a reanalysis of the Voyager 1 UVS solar occultations*, Icarus, **170** (2004) 91-112.

[18] G.L.B. Pedro V. Sada, Donald E. Jennings, George H. McCabe, Paul N. Romani, *Observations of CH_4, C_2H_6, and C_2H_2 in the Stratosphere of Jupiter*, Icarus, **136** (1998) 192-201.

[19] J.B.B. Moses, Emmanuel Lellouch, G. Randall Gladstone, Helmut Feuchtgruber, Mark Allen, *Photochemistry of Saturn's Atmosphere I. Hydrocarbon Chemistry and Comparisons with ISO Observations*, Icarus, **143** (2000) 244-298.

[20] A. Coustenis, R.K. Achterberg, B.J. Conrath, D.E. Jennings, A. Marten, D. Gautier, C.A. Nixon, F.M. Flasar, N.A. Teanby, B. Bézard, R.E. Samuelson, R.C. Carlson, E. Lellouch, G.L. Bjoraker, P.N. Romani, F.W. Taylor, P.G.J. Irwin, T. Fouchet, A. Hubert, G.S. Orton, V.G. Kunde, S. Vinatier, J. Mondellini, M.M. Abbas, R. Courtin, *The composition of Titan's stratosphere from Cassini/CIRS mid-infrared spectra*, Icarus, **189** (2007) 35-62.

[21] T.Y. Brooke, A.T. Tokunaga, H.A. Weaver, J. Crovisier, D.B. Morvan, D. Crisp, *Detection of Acetylene in the Infrared Spectrum of Comet Hyakutake*, Nature, **383** (1996) 606-608.

[22] M. Herman, *The acetylene ground state saga*, Molecular Physics, **105** (2007) 2217-2241.

[23] D. Lambot, G. Blanquet, J.-P. Bouanich, *Diode laser measurements of collisional broadening in the v5 band of C2H2 perturbed by O2 and N2*, Journal of Molecular Spectroscopy, **136** (1989) 86-92.

[24] J.P. Bouanich, D. Lambot, G. Blanquet, J. Walrand, *N2- and O2-broadening coefficients of C2H2 IR lines*, Journal of Molecular Spectroscopy, **140** (1990) 195-213.

[25] P. Varanasi, *Intensity and linewidth measurements in the 13.7 μm fundamental bands of 12C2H2 and 12C13CH2 at planetary atmospheric temperatures*, Journal of Quantitative Spectroscopy and Radiative Transfer, **47** (1992) 263-274.

[26] A. Babay, M. Ibrahimi, V. Lemaire, B. Lemoine, F. Rohart, J.P. Bouanich, *Atmospheric Spectroscopy Applications 96Line frequency shifting in the v5 band of C2H2*, Journal of Quantitative Spectroscopy and Radiative Transfer, **59** (1998) 195-202.

[27] J.P. Bouanicha, G. Blanquetb, J.C. Populaireb, J. Walrand, *Nitrogen Broadening of Acetylene Lines in the ν_5 Band at Low Temperature*, Journal of Molecular Spectroscopy, **190** (1998) 7-14.

[28] J.-P. Bouanich, G. Blanquet, J. Walrand, *Line-Mixing Effects in He- and N2-Broadened $\Sigma \leftarrow \Pi$ Infrared Q Branches of C2H2*, Journal of Molecular Spectroscopy, **203** (2000) 41-48.

[29] G. Blanquet, J. Walrand, J.-P. Bouanich, *Line-Mixing Effects in He- and N2-Broadened Q Branches of C2H2 at Low Temperatures*, Journal of Molecular Spectroscopy, **210** (2001) 1-7.

[30] V. Malathy Devi, D. Chris Benner, C.P. Rinsland, M.A.H. Smith, B.D. Sidney, *Tunable Diode Laser Measurements Of N_2- And Air-Broadened Half Widths: Lines In The $(v4 + v5)^0$ Band Of $^{12}C_2H_2$ Near 7.4 μm*, Journal of Molecular Spectroscopy, **114** (1985) 49-53.

[31] M. Dhyne, L. Fissiaux, J.-C. Populaire, M. Lepère, *Temperature dependence of the -broadening coefficients of acetylene*, Journal of Quantitative Spectroscopy and Radiative Transfer, **110** (2009) 358-366.

[32] L. Fissiaux, M. Dhyne, M. Lepère, *Diode-laser spectroscopy: Pressure dependence of N2-broadening coefficients of lines in the band of C2H2*, Journal of Molecular Spectroscopy, **254** (2009) 10-15.

[33] M. Dhyne, P. Joubert, J.-C. Populaire, M. Lepère, *Collisional broadening and shift coefficients of lines in the v4+v5 band of 12C2H2 diluted in N2 from low to room temperatures*, Journal of Quantitative Spectroscopy and Radiative Transfer, **111** (2010) 973-989.

[34] S.W. Arteaga, C.M. Bejger, J.L. Gerecke, J.L. Hardwick, Z.T. Martin, J. Mayo, E.A. McIlhattan, J.M.F. Moreau, M.J. Pilkenton, M.J. Polston, B.T. Robertson, E.N. Wolf, *Line broadening and shift coefficients of acetylene at 1550nm*, Journal of Molecular Spectroscopy, **243** (2007) 253-266.

[35] C.P. McRaven, M.J. Cich, G.V. Lopez, T.J. Sears, D. Hurtmans, A.W. Mantz, *Frequency comb-referenced measurements of self- and nitrogen-broadening in the v1 + v3 band of acetylene*, Journal of Molecular Spectroscopy, **266** (2011) 43-51.

[36] N.T. Campbell, J.D. Cook, B.A. Coombs, E.P. Fuller, J.L. Hardwick, S.M. Hurley, L.K. Ho, P.A. Kovac, E.J. Robertson, E.N. Senning, J.K. Utterback, R.S. Wiser, *Temperature dependence of pressure broadening and shifts of acetylene at 1550 nm by N2*, Molecular Physics, **109** (2011) 2199-2208.

[37] A.S. Pine, *Self-Broadening, N_2-Broadening and Ar-Broadening and Line Mixing in HCN and C_2H_2.* , Journal of Quantitative Spectroscopy & Radiative Transfer, **50** (1993) 149-166

[38] H. Valipour, D. Zimmermann, *Investigation of J Dependence of Line Shift, Line Broadening, and Line Narrowing Coefficients in the v_1+3v_3 Absorption Band of Acetylene*, Journal of Chemical Physics, **114** (2001) 3535.

[39] C. Povey, A. Predoi-Cross, D.R. Hurtmans, *Line Shape Study of Acetylene Transitions in the* $v_1+v_2+v_4+v_5$ *Band Over a Range of Temperatures*, Journal of Molecular Spectroscopy, **268** (2011) 177-188.

[40] B.K. Dutta, D. Biswas, B. Ray, P.N. Ghosh, *Diode Laser Spectroscopic Measurement and Impact Theoretical Analysis of Collision Broadening of Acetylene Band Transitions*, The European Physical Journal D - Atomic, Molecular, Optical and Plasma Physics, **11** (2000) 99-108.

[41] P. Minutolo, C. Corsi, F. D'Amato, M. De Rosa, *Self-and Foreign-Broadening and Shift Coefficients for* C_2H_2 *Lines at 1.54 µm*, The European Physical Journal D-Atomic, Molecular, Optical and Plasma Physics, **17** (2001) 175-179.

[42] J.P. Bouanich, G. Blanquet, J. Walrand, *Oxygen Broadening of Acetylene Lines in the* v_5 *Band at Low Temperature* Journal of Molecular Spectroscopy **194** (1999) 269-277.

[43] J.L. Domenech, F. Thibault, D. Bermejo, J.P. Bouanich, *Ar-Broadening of Isotropic Raman Lines in the* v_2 *Band of Acetylene*, Journal of Molecular Spectroscopy, **225** (2004) 48-54.

[44] M. Lepère, G. Blanquet, J. Walrand, J. Bouanich, M. Herman, J. Vander Auwera, *Self-Broadening Coefficients and Absolute Line Intensities in the* $v_4 + v_5$ *Band of Acetylene*, Journal of Molecular Spectroscopy, **242** (2007) 25-30.

[45] F. Thibault, E.P. Fuller, K.A. Grabow, J.L. Hardwick, C.I. Marcus, D. Marston, L.A. Robertson, E.N. Senning, M.C. Stoffel, R.S. Wiser, *Experimental Line Broadening and Line Shift Coefficients of the Acetylene* v_1+v_3 *Band Pressurized by Hydrogen and Deuterium and Comparison with Calculations*, Journal of Molecular Spectroscopy, **256** (2009) 17-27.

[46] J.S. Li, G. Durry, J. Cousin, L. Joly, B. Parvitte, V. Zeninari, *Self-Broadening Coefficients and Positions of Acetylene Around 1.533µm Studied by High-Resolution Diode Laser Absorption Spectrometry*, Journal of Quantitative Spectroscopy and Radiative Transfer, **111** (2010) 2332-2340.

[47] H. Rozario, J. Garber, C. Povey, D. Hurtmans, J. Buldyreva, A. Predoi-Cross, *Experimental and theoretical study of N2-broadened acetylene line parameters in the v1 + v3band over a range of temperatures*, Molecular Physics, **110** (2012) 2645-2663.

[48] B. Martin, J. Walrand, G. Blanquet, J. Bouanich, M. Lepère, *CO2-broadening coefficients in the v4+ v5 band of acetylene*, Journal Of Molecular Spectroscopy, **236** (2006) 52-57.

[49] R. Hashemi, H. Rozario, C. Povey, A. Predoi-Cross, *Line-shape models testing on six acetylene transitions in the v1+v3 band broadened by N2*, Journal of Quantitative Spectroscopy and Radiative Transfer, **140** (2014) 58-66.

[50] L. Snyder, D. Buhl, *Observations of Radio Emission From Interstellar Hydrogen Cyanide*, The Astrophysical Journal **163** (1971) 47-52.

[51] A.A. Penzias, R.W. Wilson, *Deuterium Cyanide in the Orion Nebula*, The Astrophysical Journal, **179** (1973) 57- 59.

[52] H. Roberts, E. Herbst, T.J. Millar, *The chemistry of multiply deuterated species in cold, dense interstellar cores*, Astronomy and Astrophysics, **424** (2004) 905-917.

[53] R. Meier, T.C. Owen, D.C. Jewitt, H.E. Matthews, M. Senay, N. Biver, D. Bockelée-Morvan, J. Crovisier, D. Gautier, *Deuterium in Comet C/1995 O1 (Hale-Bopp): Detection of DCN*, Journal of Science, **279** (1998) 1707-1710.

[54] M. Winnewisser, J. Vogt, *l-Type Doublet Transitions of the Rare Stable Isotopic Species of Hydrogen Cyanide, HCN*, Journal of Zeitschrift für Naturforschung A, **33** (1978).

[55] J. Preusser, A.G. Maki, *Millimeter-Wave Measurements of Vibrationally Excited States of the HCN Isotopomers* $H^{13}C^{14}N$, $H^{12}C^{15}N$, $H^{13}C^{15}N$, $D^{12}C^{14}N$, $D^{13}C^{14}N$, $D^{12}C^{15}N$, *and* $D^{13}C^{15}N$, Journal of Molecular Spectroscopy, **162** (1993) 484-497.

[56] A.G. Maki, E.K. Plyler, R. Thibault, *Vibration–Rotation Bands of Deuterium Cyanide and Hydrogen Cyanide*, Journal of the Optical Society of America **54** (1964) 869-876.

[57] W. Quapp, M. Hirsch, G.C. Mellau, S. Klee, M. Winnewisser, A. Maki, *Climbing the Bending Vibrational Ladder in* $D^{13}C^{15}N$ *by Hot Gas Emission Spectroscopy*, Journal of Molecular Spectroscopy, **195** (1999) 284-298.

[58] E. Mollmann, A.G. Maki, M. Winnewisser, B.P. Winnewisser, W. Quapp, *High-Temperature Infrared Emission Spectra of* $D^{12}C^{14}N$ *and* $D^{13}C^{14}N$, Journal of Molecular Spectroscopy, **212** (2002) 22-31.

[59] A. Maki, W. Quapp, S. Klee, G.C. Mellau, S. Albert *Infrared Transitions of* $H^{12}C^{14}N$ *and* $H^{12}C^{15}N$ *Between 500 and 10000* cm^{-1}, Journal of Molecular Spectroscopy, **180** (1996) 323-336.

[60] A. Maki, W. Quapp, S. Klee, G.C. Mellau, S. Albert, *The CN Mode of HCN: A Comparative Study of the Variation of the Transition Dipole and Herman–Wallis Constants for Seven Isotopomers and the Influence of Vibration–Rotation Interaction*, Journal of Molecular Spectroscopy, **174** (1995) 365-378.

[61] W. Quapp, S. Klee, G.C. Mellau, S. Albert, A. Maki, *Fourier Transform Spectra of Overtone Bands of HCN from 4800 to 9600* cm^{-1}*: Some New Transitions of Bending Combination Modes*, Journal of Molecular Spectroscopy **167** (1994) 375-382.

[62] G.C. Mellau, B.P. Winnewisser, M. Winnewisser, *Near infrared emission spectrum of HCN*, Journal of Molecular Spectroscopy, **249** (2008) 23-42.

[63] J.P. Hofmann, B. Eifert, G.C. Mellau, *Near infrared emission spectrum of H13CN*, Journal of Molecular Spectroscopy, **262** (2010) 75-81.

[64] N. Hata, R.J. Scherrer, G. Steigman, D. Thomas, T.P. Walker, *Predicting Big Bang Deuterium*, Journal of Astrophysics, **458** (1996) 637.

[65] R. Beer, *Detection Of Carbon Monoxide In Jupiter*, The Astrophysical Journal, **200** (1975) 167-169.

[66] K.S. Noll, R.F. Knacke, T.R. Geballe, A.T. Tokunaga, *Detection Of Carbon Monoxide In Saturn* The Astrophysical Journal, **309** (1986) 91-94.

[67] T. Cavalié, F. Billebaud, M. Dobrijevic, T. Fouchet, E. Lellouch, T. Encrenaz, J. Brillet, G.H. Moriarty-Schieven, J.G.A. Wouterloot, P. Hartogh, *First observation of CO at 345GHz in the atmosphere of Saturn with the JCMT: New constraints on its origin*, Icarus, **203** (2009) 531-540.

[68] R.K. Kakar, J.W. Walters, W.J. Wilson, *Mars: Microwave Detection of Carbon Monoxide*, Science, **196** (1977) 1090-1091.

[69] R.K. Kakar, J.W. Waters, W.J. Wilson, *Venus: Microwave Detection of Carbon Monoxide*, Science **191** (1976) 379-380.

[70] V. Malathy Devi, D. Chris Benner, M.A.H. Smith, A.W. Mantz, K. Sung, L.R. Brown, A. Predoi-Cross, *Spectral line parameters including temperature dependences of self- and air-broadening in the 2←0 band of CO at 2.3μm*, Journal of Quantitative Spectroscopy and Radiative Transfer, **113** (2012) 1013-1033.

[71] R.L. Dickman, R.L. Snell, F.P. Schloerb, *Carbon Monoxide As An Extragalactic Mass Tracer*, Astrophysical Journal, Part 1, **309** (1986) 326-330.

[72] E.K. Plyler, R.J. Thibault, *Self-Broadening of Carbon Monoxide In the 2v and 3v Bands*, Journal Of Research of the National Bureau of Standards-A. Physics and Chemistry, **67A** (1963) 209.

[73] T.C. James, E.K. Plyler, *Linewidths in the 2–0 Band of Carbon Monoxide Broadened by Nitrogen and Hydrogen*, The Journal of Chemical Physics, **40** (1964) 221.

[74] R.H. Hunt, *High-Resolution Determination of the Widths of Self-Broadened Lines of Carbon Monoxide*, The Journal of Chemical Physics, **49** (1968) 3909.

[75] J.P. Bouanich, C. Brodbeck, *MESURE DES LARGEURS ET DES DEPLACEMENTS DES RAIES DE LA BANDE 0 -2 DE CO AUTOPERTURBE ET PERTURBE PAR N_2, O_2*

,H_2, HCl, NO ET CO_2, Journal of Quantitative Spectroscopy & Radiative Transfer, **13** (1973) 1-7.

[76] J.P. Bouanich, *On The Temperature Dependence Of Self-Broadening In The First Overtone Band Of CO*, Journal of Quantitative Spectroscopy and Radiative Transfer, **31** (1984) 561-567.

[77] J.P. Bouanicha, D. Bermejo, J.L. Domenech, R.Z. Martinez, J. Santos, *Pressure-Induced Line Shifts In The 2 ← 0 Band of CO Self-Perturbed and Perturbed by He, Kr, O_2, and N_2*, Journal of Molecular Spectroscopy, **179** (1996) 22–31.

[78] A. Predoi-Cross, J.P. Bouanich, D.C. Benner, A.D. May, J.R. Drummond, *Broadening, Shifting, And Line Asymmetries In The 2-0 Band Of CO and CO–N_2 : Experimental Results And Theoretical Calculations*, Journal Of Chemical Physics, **113** (2000) 158-168.

[79] Q. Zou, P. Varanasi, *New Laboratory Data On The Spectral Line Parameters In The 1-0 and 2-0 bands of $^{12}C^{16}O$ Relevant To Atmospheric Remote Sensing*, Journal of Quantitative Spectroscopy and Radiative Transfer, **75** (2002) 63–92.

[80] V. Malathy Devi, D.C. Benner, M.A.H. Smith, C.P. Rinsland, A.W. Mantz, *Determination Of Self- And H_2-Broadening And Shift Coefficients In The 2-0 Band Of $^{12}C^{16}O$ Using A Multispectrum Fitting Procedure*, Journal of Quantitative Spectroscopy & Radiative Transfer, **75** (2002) 455–471.

[81] J.W. Brault, L.R. Brown, C. Chackerian, R. Freedman, A. Predoi-Cross, A.S. Pine, *Self-broadened 12C16O line shapes in the v=2←0 band*, Journal of Molecular Spectroscopy, **222** (2003) 220-239.

[82] K. Sung, P. Varanasi, *Hydrogen-broadened half-widths and hydrogen-induced line shifts of relevant to the Jovian atmospheric spectra*, Journal of Quantitative Spectroscopy and Radiative Transfer, **85** (2004) 165-182.

[83] L. Régalia-Jarlot, X. Thomas, P. Von der Heyden, A. Barbe, *Pressure-broadened line widths and pressure-induced line shifts coefficients of the (1-0) and (2-0) bands of*, Journal of Quantitative Spectroscopy and Radiative Transfer, **91** (2005) 121-131.

[84] V. Malathy Devi, A. Predoi-Cross, D. Chris Benner, M.A.H. Smith, C.P. Rinsland, A.W. Mantz, *Self- and H2-broadened width and shift coefficients in the 2←0 band of 12C16O: revisited*, Journal of Molecular Spectroscopy, **228** (2004) 580-592.

[85] J.M. Hollas, Modern Spectroscopy,, 4th Edition ed., Wiley, England, 2004.

[86] P.F. Bernath, Spectra of Atoms and Molecules, Oxford University Press, New York, 1995.

[87] http://lumenistics.com/what-is-full-spectrum-lighting.

[88]http://chemwiki.ucdavis.edu/Core/Physical_Chemistry/Quantum_Mechanics/07._Angular_Momentum/7.5%3A_Rigid_Rotor.

[89] D.M. Fluri, Molecular Universe, in, Institute of Astronomy ETH Zurich, 2009.

[90] https://en.wikiversity.org/wiki/Spectroscopy/Rotational_spectroscopy.

[91]http://mackenzie.chem.ox.ac.uk/teaching/Molecular%20Vibrational%20Spectroscopy.pdf.

[92] H. Rozario, Spectroscopic Study of Acetylene and Hydrogen Cyanide, in: Department of Physics and Astronomy, University of Lethbridge, Canada, 2012.

[93] https://en.wikipedia.org/wiki/Rotational%E2%80%93vibrational_spectroscopy.

[94] J. Schostag, Intensity Analysis of Transitions Between Highly Excited Ro-vibrational States, in: Department of Physical Chemistry, Justus-Liebig-University, Germany, 2011.

[95]http://chemwiki.ucdavis.edu/Physical_Chemistry/Kinetics/Reaction_Rates/Experimental_Determination_of_Kinetcs/Spectrophotometry.

[96] D. Robert, J.M. Hartmann, C. Boulet, Collisional Effects on Molecular Spectra, Elsevier Science, United Kingdom, 2008.

[97] D.E. Heard, Analytical Techniques for Atmospheric Measurement, Wiley-Blackwell, 2006.

[98] G.E. Thomas, K. Stamnes, Radiative Transfer in the Atmosphere and Ocean, Cambridge University Press, United Kingdom, 2002.

[99] C.D. Boone, K.A. Walker, P.F. Bernath, *Speed-Dependent Voigt Profile for Water Vapor in Infrared Remote Sensing Applications*, Journal of Quantitative Spectroscopy and Radiative Transfer, **105** (2007) 525-532.

[100] L. Galatry, *Simultaneous Effect of Doppler and Foreign Gas Broadening on Spectral Lines*, Physical Review, **122** (1961) 1218-1223.

[101] H. Li, A. Farooq, J.B. Jeffries, R.K. Hanson, *Diode laser measurements of temperature-dependent collisional-narrowing and broadening parameters of Ar-perturbed H2O transitions at 1391.7 and 1397.8nm*, Journal of Quantitative Spectroscopy and Radiative Transfer, **109** (2008) 132-143.

[102] S.G. Rautian, I.I. Sobel'man, *The Effect Of Collisions On The Doppler Broadening Of Spectral Lines*, Soviet Physics Uspekhi, **9** (1967) 701.

[103] M. Nelkin, A. Ghatak, *Simple Binary Collision Model for Van Hove'sGs(r, t)*, Physical Review, **135** (1964) A4-A9.

[104] http://www.atecorp.com/products/neslab/ult-80.aspx.

[105] https://en.wikipedia.org/wiki/Methanol.

[106] NEScom 4.0 Temperature Control Software for Windows User Manual., in: T. Scientific (Ed.), 2014.
[107] https://en.wikipedia.org/wiki/Resistance_thermometer.

[108] http://www.sensor-technology.com.br/en/site/download.

[109] http://www.npl.co.uk/educate-explore/factsheets/temperature.

[110]http://www.lakeshore.com/products/cryogenic-temperature-monitors/model-218/Pages/Overview.aspx.

[111] D.C. Benner, C.P. Rinsland, V.M. Devi, M.A.H. Smith, D. Atkins, *A Multispectrum Nonlinear Least Squares Fitting Technique*, Journal of Quantitative Spectroscopy and Radiative Transfer, **53** (1995) 705-721.

[112] F. Rohart, H. Mäder, H.W. Nicolaisen, *Speed dependence of rotational relaxation induced by foreign gas collisions: Studies on CH3F by millimeter wave coherent transients,* The Journal of Chemical Physics, **101** (1994) 6475-6486.

[113] F. Rohart, A. Ellendt, F. Kaghat, H. Mäder, *Self and Polar Foreign Gas Line Broadening and Frequency Shifting of CH3F: Effect of the Speed Dependence Observed by Millimeter-Wave Coherent Transients,* Journal of Molecular Spectroscopy, **185** (1997) 222-233.

[114] R. Wehr, R. Ciuryło, A. Vitcu, F. Thibault, J.R. Drummond, A.D. May, *Dicke-narrowed spectral line shapes of CO in Ar: Experimental results and a revised interpretation*, Journal of Molecular Spectroscopy, **235** (2006) 54-68.

[115] V. Malathy Devi, D.C. Benner, L.R. Brown, C.E. Miller, R.A. Toth, *Line mixing and speed dependence in CO2 at 6348 cm−1: Positions, intensities, and air- and self-broadening derived with constrained multispectrum analysis*, Journal of Molecular Spectroscopy, **242** (2007) 90-117.

[116] A.G. Maki, G.C. Mellau, S. Klee, M. Winnewisser, W. Quapp, *High-Temperature Infrared Measurements in the Region of the Bending Fundamental of H12C14N, H12C15N, and H13C14N*, Journal of Molecular Spectroscopy, **202** (2000) 67-82.

[117] L.S. Rothman, I.E. Gordon, Y. Babikov, A. Barbe, D. Chris Benner, P.F. Bernath, M. Birk, L. Bizzocchi, V. Boudon, L.R. Brown, A. Campargue, K. Chance, E.A. Cohen, L.H. Coudert, V.M. Devi, B.J. Drouin, A. Fayt, J.M. Flaud, R.R. Gamache, J.J. Harrison,

J.M. Hartmann, C. Hill, J.T. Hodges, D. Jacquemart, A. Jolly, J. Lamouroux, R.J. Le Roy, G. Li, D.A. Long, O.M. Lyulin, C.J. Mackie, S.T. Massie, S. Mikhailenko, H.S.P. Müller, O.V. Naumenko, A.V. Nikitin, J. Orphal, V. Perevalov, A. Perrin, E.R. Polovtseva, C. Richard, M.A.H. Smith, E. Starikova, K. Sung, S. Tashkun, J. Tennyson, G.C. Toon, V.G. Tyuterev, G. Wagner, *The HITRAN2012 molecular spectroscopic database*, Journal of Quantitative Spectroscopy and Radiative Transfer, **130** (2013) 4-50.

[118] P.W. Rosenkranz, *Shape Of The 5 mm Oxygen Band In The Atmosphere*, IEEE Transactions on Antennas and Propagation, **23** (1975) 498-506.

[119] R.S. Pope, Collional Effects in the Absorption Spectra of the Oxygen A Band and Nitric Oxide Fundamental Band, in: School of Engineering of the Air Force Institute of Technology Air Education and Training Command United States Air Force, Ohio Wright-Patterson Air Force Base, United States, 1998.

[120] C. Povey, A. Predoi-Cross, *Computations of temperature dependences for line shape parameters in the 30012←00001 and 30013←00001 bands of pure CO2*, Journal of Molecular Spectroscopy, **257** (2009) 187-199.

[121] P.W. Rosenkranz, IEEE, Trans, Anten. Propag. , **23** (1975) 498-506.

[122] M. Šimečková, D. Jacquemart, L.S. Rothman, R.R. Gamache, A. Goldman, *Einstein A-coefficients and statistical weights for molecular absorption transitions in the HITRAN database*, Journal of Quantitative Spectroscopy and Radiative Transfer, **98** (2006) 130-155.

[123] http://www.nasa.gov, NASA.

[124] D.H. Rank, D.P. Eastman, W.B. Birtley, T.A. Wiggins, *Shapes and Breadths of Some Molecular Rotation-Vibration Band Lines Perturbed by Rare Gases*, The Journal of Chemical Physics, **33** (1960) 327.

[125] P. Varanasi, B.R.P. Bangaru, *Intensity and Half-Width Measurements in 1.525 mm Band of Acetylene*, Journal of Quantitative Spectroscopy and Radiative Transfer, **15** (1975) 267-273.

[126] J.S. Wong, *Pressure Broadening of Single Vibrational-Rotational Transitions of Acetylene at v=5*, Journal of Molecular Spectroscopy, **82** (1980) 449-451.

[127] D. Lambot, A. Olivier, G. Blanquet, J. Walrand, J.P. Bouanich, *Diode-Laser Measurements of Collisional Line Broadening in the* ν_5 *Band of* C_2H_2, Journal of Quantitative Spectroscopy & Radiative Transfer **45** (1991) 145-155.

[128] D. Lambot, J.C. Populaire, J. Walrand, G. Blanquet, J.P. Bouanich, *Diode-Laser Measurements of Self-Broadening Coefficients in the* ν_5 *Band of* C_2H_2 *at Low Temperature*, Journal of Molecular Spectroscopy, **165** (1994) 1-11.

[129] M. Herman, R. Georges, D. Hurtmans, D. Van Der Vorst, *Ar and Self-Pressure Broadening Coefficient of the R(11), 5*v_3 *Line of12* C_2H_2 Journal of Molecular Spectroscopy **185** (1997) 187-188.

[130] D. Biswas, B. Ray, S. Dutta, P.N. Ghosh, *Diode Laser Spectroscopic Measurement of Line Shape of* n_1*+3*n_3 *Band Transitions of Acetylene*, Applied Physics B-Lasers and Optics **68** (1999) 1125-1130.

[131] J.J. Olivero, R.L. Longbothum, *Empirical Fits To The Voigt Line Width: A Brief Review*, Journal of Quantitative Spectroscopy & Radiative Transfer, **17** (1977) 233-236.

[132] F. Herregodts, D. Hurtmans, J. Vander Auwera, M. Herman, *Laser Spectroscopy of the* v_1 *+3*v_3 *Absorption Band in* $^{12}C_2H_2$*. I. Pressure Broadening And Absolute Line Intensity Measurements*, Journal of Chemical Physics **111** (1999) 7954.

[133] F. Herregodts, M. Hepp, D. Hurtmans, J. Vander Auwera, M. Herman, *Laser Spectroscopy of the* v_1 *+3*v_3 *Absorption Band in* $^{12}C_2H_2$*. II. Self-Collisional Lineshift Measurements* Journal of Chemical Physics, **111** (1999) 7961.

[134] J.U. White, *Long Optical Paths of Large Aperture*, Journal of the Optical Society of America, **32** (1942) 285-288.

[135] C. Yelleswarapu, A. Sharma, *Pressure-Induced Self-Broadening and Frequency Shift Measurements of Absorption Lines of Acetylene Using Tunable Diode Laser Absorption Spectroscopy*, Journal of Quantitative Spectroscopy & Radiative Transfer, **69** (2001) 151-158.

[136] D.R. Herriott, H.J. Schulte, *Folded Optical Delay Lines*, Appl. Opt., **4** (1965) 883-889.

[137] D. Jacquemart, J.Y. Mandin, V. Dana, L. Regalia-Jarlot, X. Thomas, P.V.d. Heyden, *Multispectrum Fitting Measurements Of Line Parameters For 5 micron Cold Bands Of Acetylene*, Journal of Quantitative Spectroscopy & Radiative Transfer, **75** (2002) 397-422.

[138] J.R. Podolske, M. Loewenstein, P. Varanasi, *Diode Laser Line Strength Measurements of the* $(v_4 + v_5)^0$ *Band of* $^{12}C_2H_2$., Journal of Molecular Spectroscopy **107** (1984) 241–249.

[139] W.C. Swann, S.L. Gilbert, *Pressure-Induced Shift and Broadening of 1510–1540-nm Acetylene Wavelength Calibration Lines* Journal of the Optical Society of America B, **17** (2000) 1263-1270.

[140] J.-P. Bouanich, J. Walrand, G. Blanquet, *Argon-Broadening Coefficients in the v5 Band Of Acetylene At Room and Low Temperatures*, Journal of Molecular Spectroscopy, **219** (2003) 98-104.

[141] C. Povey, M. Guillorel-Obregon, A. Predoi-Cross, S.V. Ivanov, O.G. Buzykin, F. Thibault, *Low Pressure Line Shape Study of Nitrogen-Perturbed Acetylene Transitions in the* $\nu_1 + \nu_3$ *Band Over a Range of Temperatures*, Canadian Journal of Physics, **91** (2013) 896-905.

[142] M.J. Cich, C.P. McRaven, G.V. Lopez, T.J. Sears, D. Hurtmans, A.W. Mantz, *Temperature-Dependent Pressure Broadened Line Shape Measurements in the* $\nu_1+\nu_3$ *Band of Acetylene Using a Diode Laser Referenced To a Frequency Comb*, Applied Physics B, **109** (2011) 373-384.

[143] A.S. Pine, *Asymmetries and Correlations in Speed-Dependent Dicke-Narrowed Line Shapes of Argon-Broadened HF*, Journal of Quantitative Spectroscopy & Radiative Transfer, **62** (1999) 397-423.

Appendix A: Review of spectroscopic studies on acetylene

The first study on the pressure broadening of acetylene in the vibrational band of v_1+v_3 located at 6451 cm^{-1} has been accomplished in 1960 [124]. Varanasi and Bangaru [124] measured the self-broadened half-widths in the R-branch of the v_1+v_3 band of acetylene at 171 K, 200 K, 250 K, 295 K, and the hydrogen-broadened half-widths at 171 K, 200 K, and 295 K [125]. Wong [126] studied the self-broadening of acetylene in the R-branch of the v_1+v_3 and 5v_3 at room temperature within the range of his dye laser based spectrometer.

Lambot *et al.* [127] retrieved self-broadening coefficients in the v_5 band for 27 R- and P-branch lines of acetylene at room temperature using a tunable diode-laser spectrometer. The authors used semi-classical models to calculate the self-broadening parameters. A second study on self-broadening coefficients by Lambot *et al.* [128] covered 21 P- and R-branch transitions of C_2H_2 in the v_5 band (670-790 cm^{-1}) at low temperature (173 K) using same laser spectrometer described in Ref [127].

Self-, N_2- and Ar-foreign broadened transitions of acetylene lines located nearby 4091 cm^{-1} in the v_1+v_5 band has been studied by Pine [37] using a frequency-difference laser spectrometer. He was able to quantify the line mixing effect in the Q-branch using scaling laws. He also accounted for the Dicke narrowing effect because of the possibility of being in this regime by using the Rautian Profile (RP), also known as the hard collision [102] model.

Georges *et al.* [129] measured the Ar- and self-broadening parameter of the R (11) transition belonging to 5v_3 of C_2H_2 using a ring dye laser spectrometer. Biswas *et al.* [130] published measurements of the self- and N_2-broadening of six transitions, P(7), P(8), P(13), P(15), R(9) and R(11) of C_2H_2 in the v_1+3v_3 band located nearby 12787 cm^{-1}. The line parameters have been extracted using the Voigt profile (VP) [131]. Absorption spectra in the near-infrared region have been collected using a tunable diode laser spectrometer.

Twenty two lines belonging to the v_1+3v_3 band of acetylene have been studied by Herregodts *et al.* [132]. The Voigt model was used to retrieve the self-broadening parameters. The authors used a Ti:Sa autoscan laser spectrometer to record the spectra at different pressures between 10 and 600 Torr. They reported observing the Dicke narrowing effect at pressures below150 Torr due to molecular confinement. Their results confirmed that self-broadening coefficients are independent of vibration. Herregodts *et al.* [133] have measured the self-collisional line shifts for transitions in the same band as Ref [132]. Herregodts *et al.* determined the self-shift values for 30 transitions belonging to P and R branches of C_2H_2 employing a multiple-pass cell referred to as a White cell [134].

Yelleswarapu and Sharma [135] have published the pressure-induced and self-broadening parameters of multiple absorption transitions of C_2H_2 in the v_1+3v_3 band over a range of pressures between 5 to 600 Torr. They used a diode laser as light source in the 12820 cm^{-1} region and a multi-pass cell to reach 35 meter path-length. The absorption spectra were modelled by using the Voigt Profile.

A study by Minutolo *et al.* [41] reported measurements on self-, N_2-, O_2- and CO_2-broadening as well as pressure shifts obtained using the Voigt model for several transitions of acetylene and $H^{13}C^{12}CH$ belonging to 4 different vibrational bands located nearby 6493 cm^{-1}.

A multi-pass Herriot cell [136] and a laser system functioning at 12690 cm^{-1} were used by Valipour and Zimmermann [38] to determine the shift, line broadening, and line narrowing values for 20 transitions in the P- and R-branches broadened by air, N_2, O_2, He, Ne, Ar, Kr, and Xe. They interpreted the spectrum using the Galatry Profile (GP) [100] (also known as the soft collision model) in order to be able to take into account for the Dicke narrowing phenomenon.

Jacquemart [137] have measured the self-broadening and self-shifting coefficients, for transitions in the cold bands located in the 2000 cm^{-1} range of C_2H_2. Nitrogen- and air-broadening of acetylene parameters for several spectral lines in the v_4+v_5 band located near 1351 cm^{-1} range have been reported by Devi *et al.* [30] using a diode laser spectrometer and the Voigt line shape model. N_2-and He-broadening parameters of several R-branch transitions of acetylene in the v_4+v_5 combination band at 1351 cm^{-1} have been measured by Podolske *et al.* [138] using a diode laser spectrometer.

Swann and Gilbert [139] have measured the self-broadening and collisional pressure shift coefficients of C_2H_2 using spectra recorded for 15 transitions at several pressures in the 6622 to 6493 cm^{-1} region. The nitrogen broadening coefficients for acetylene transitions retrieved using the Rautian profile [102] have been reported by Bouanich *et al.* [27]. They collected the spectra for 22 lines in the P- and R-branches of the v_3 band at 173.4 K over the spectral range of 661–762 cm^{-1} employing a tunable diode-laser spectrometer.

An investigation by Bouanich *et al.* [140] reported of argon-broadening parameters in the ν_5 band of acetylene. They were successful to obtain broadening coefficients at room and 173.15 K temperatures using a tunable diode laser working in the spectral range of 665–795 cm^{-1}. The spectra were examined using the Voigt and Rautian profiles and the uncorrelated General Rautian profile (GRP) [102] in order to consider the Dicke narrowing effect and the speed dependence of the collisional cross-sections for the last two models, respectively. In 1999 Bouanich *et al.* [42] has published a study on the oxygen-broadening coefficients for 29 transitions in the ν_5 band. The spectra were recorded at low temperatures for the P- and R-branches of the same band (ν_5) in the 714 cm^{-1} region. The results were retrieved using the Rautian and Voigt profiles.

Self-, air- and O_2-broadening coefficients have been reported by Dutta *et al.* [40] for transitions in the v_1+3v_3 overtone band of acetylene using a near infrared diode laser that covers the 12987- 12578 cm^{-1} range. The spectrum were least squares fitted using the Voigt model. In addition, the authors modelled the spectrum using a semi-classical impact theory involving quadrupole and dispersion interactions.

A high resolution Raman spectrometer was used by Domenech *et al.* [43] to measure Ar-broadening coefficients of acetylene in the Q branch at temperatures of 295, 174 and 134 K, respectively. The authors examined the data using the Rautian profile and comparing them with theoretical values emerging from close coupling and coupled states calculations.

Lepère *et al.* [44] have studied the self-broadening coefficients for 30 transitions in the R- and P-branches of C_2H_2 belonging to v_4+v_5 combination bands at room temperature, over the spectral range of 1275–1390 wavenumber. The authors have compared their results obtained using the Voigt and Rautian models with the results of a semi-classical calculation taking into account the electrostatic interactions and anisotropic dispersion contribution.

An intense near infrared study at 6451 cm^{-1} has been done by Arteaga *et al.* [34] to measure the broadening and shift parameters of C_2H_2 perturbed by H_2, D_2, N_2, air, and noble gases at room temperature. They measured the spectra corresponding to the combination band v_1+v_3 located between 6613–6468 cm^{-1} from P(31) to R(27) using the Voigt profile.

Dhyne *et al.* [31] have published broadening coefficients of seven transitions of the C_2H_2 perturbed by nitrogen in the v_1+v_3 band located in the 1330 wavenumber region. An infrared diode laser was utilized as light source to scan the range at different temperatures (173.2, 198.2, 223.2, 248.2, and 273.2 K). The absorption spectrum were modeled using Voigt and the Rautian lineshape functions.

An experimental and theoretical study by Thibault *et al.* [45] reported the broadening and line shift parameters for nearly 50 transitions from P(25) to R(25) of acetylene mixed with hydrogen and deuterium in the combination band v_1+v_3. A tunable diode laser spectrometer was used to record the absorption spectra at 295K. The results have been computed using the Voigt Profile.

Song Li *et al.* [46] have measured the self-broadening coefficients of the acetylene for 10 transitions of P-branch belonging to the v_1+v_3 band in the 6666 cm^{-1} spectral range employing a high resolution tunable diode laser spectrometer designed for the Martian space mission PHOBOS-Grunt. They have modeled their recorded spectra using both the Voigt and the Rautian model.

A 3-channels diode laser spectrometer was employed by Povey *et al.* [39] to measure the self-broadening, pressure induced line shift and line mixing coefficients for 20 R-branch lines in the v_1+v_2+v_4+v_5 combination bands of C_2H_2. The authors collected spectra over a wide range of temperatures, and they examined them using the Voigt and Speed Dependent Voigt models (SDV) [99]. Moreover, Povey *et al.* [141] determined broadening and narrowing coefficients of low-pressure acetylene perturbed by nitrogen gas for six transitions of the v_1+v_3 band over a range of five pressures (5–40 Torr) and five temperatures (213–333 K). They have used the hard collision [102] model to take into account the narrowing phenomena.

Rozario *et al.* [47] have published an experimental and theoretical study on acetylene pressurized by nitrogen in the v_1+v_3 combinations band over a broad range of pressures and temperatures using the experimental setup described in Ref [39]. They determined the broadening and line shift parameters and their temperature dependences for almost 50 lines for R and P branches using the Voigt and Rautian Profiles (RP) [102].

Hashemi *et al.*[49] have studied six absorption lines of both P- and R-branches of acetylene broadened by nitrogen. The authors measured the spectra at room temperature over a pressure range from 5 to 250 Torr. They have analyzed the spectral absorption employing several models including the Voigt [28], Speed Dependent Voigt (SDV) [99], Rautian [102], Correlated Rautian (CR), Galatry, Rautian –Galatry (RGP) [142], Speed Dependent Rautian (SDR) and Correlated Speed Dependent Rautian (CSDR) [143] line-shape profiles.

Up to date, it seems only one study has been performed on acetylene broadened by carbon dioxide. Martin *et al.* [48] have published the broadening coefficients of 24 P- and R-branch transitions involving in the v_4+v_5 bands of acetylene mixed by carbon dioxide. They have examined their absorption spectra applying several line shape functions, such as the Voigt, Rautian, Galatry models.

Appendix B: Brief summary of spectroscopic line shape studies of pure carbon monoxide and carbon monoxide mixed with hydrogen

Measurements of the self-broadened half-widths for 21 transitions belonging to the first and second overtone bands of carbon monoxide were reported by *Plyler et al.* [72]. Authors have measured spectra over the wide range of pressures from 1254 to 2622 Torr at room temperature at different pathlengths using a grating spectrometer.

James *et al.* [73] have reported the line widths of 20 transitions in the first overtone of CO pressurized by bitrogen and hydrogen employing a Jarrel-Ash Ebert spectrometer. The measurements were carried out at 295 K and pressures ranging from 10 to 35 Torr.

Hunt *et al.* [74] have published the self-half-widths broadening of Carbon Monoxide in the first overtone band for 31 transitions. The measurement was performed using a Littrow type grating spectrometer having resolution of 0.045 cm^{-1} over the range of 760 to 1520 Torr in the room temperature. The accuracy of their results is estimated to be ±3.0% changing from 0.088 to 0.044 $cm^{-1}atm^{-1}$.

Twenty two self and foreign-broadened half widths of carbon monoxide transitions in the first overtone band have been retrieved by Bouanich *et al.* [83]. The spectra of CO broadened by N_2, O_2, H_2, HCl, NO and CO_2 were recorded at pressures between 1 and 5 atm and a temperature of 299 K [75]. Furthermore, Bouanich *et al.* [76] studied the self-half widths broadening of CO in the first overtone corresponding to 23 transitions. The authors collected spectra at temperatures of 298, 198, 131, 85 K and were able to measure their temperature dependencies of the half-widths. In 1996, Bouanich *et al.* [77] used a tunable difference frequency laser spectrometer to measure the pressure-induced shifting and broadening parameters for rotational transitions in the first overtone of CO. The authors have carried out the study of several transitions belonging to P- and R branches for self, O_2, He, Kr, and N_2 broadened lines of CO. They also compared their results with theoretical calculations obtained using a semi-classical model and different interaction potentials.

Predoi-Cross *et al.* [78] measured the broadening, shifting and line mixing coefficients of 21 lines of P and R branches in the 2-0 vibrational band of pure CO and CO-N_2. The data collection was carried out utilizing a Bomem DA8.003 Fourier transform spectrometer and pressures up to 760, 4560 Torr at 303 K. A Voigt profile was used to model the spectral line parameters as well as an empirical line shape function (HC_v) obtained by convolving the hard collision and speed-dependent Lorentz models.

Self- and air-broadening and collisional pressure shift coefficients located in the vibrational bands (1-0) and (2-0) of carbon monoxide have been analyzed for several rotational quantum numbers between P(24) and R(26) by Zou and Varanasi [79]. The authors reported the line centers, intensities and the broadening and shifting temperature dependencies. A high-resolution Fourier-transform spectrometer Bruker IFS-120HR, provided with a globar source and a liquid-nitrogen-cooled, InSb, detector was employed to record the absorption spectra at several temperatures between 174 K to the ambient temperature.

Devi *et al.* [80] have published the line parameters for pure CO and CO pressurized in hydrogen in the (1-0) vibrational band. Their measurements covered the 4130 to 4345 wavenumber range, corresponding to rotational transitions from P(27) to R(27). The measurements were carried out using a Fourier transform spectrometer at the McMath-Pierce facility of the National Solar Observatory located at Kitt Peak, AZ.

Brault *et al.* [81] have reported the self-broadening, pressure induced shift, and line mixing parameters, line positions and intensities in the first overtone band of carbon monoxide for 46 rotational transitions belonging to P and R branches as well as transition dipole moments. All the spectra were recorded at the temperature between 297.8 to 301.6 K. A simultaneous multispectrum fit was used to retrieve the results.

Hydrogen-broadened half-widths and pressure-induced line shift coefficients and computed temperature dependencies of several P and R branch lines in the fundamental, first overtone and second overtone vibrational bands of CO have been studied by Sung *et al.* [82]. The spectra were recorded at temperatures ranging from 83 to 302 K and pressures from 101 to 540 Torr.

Devi *et al.* [84] have analyzed half-width and pressure-induced shift coefficients of pure CO and CO diluted by H_2 for rotational lines from P(24) to R(24) in first overtone vibrational band of CO at room temperature and pressure between 3 to 643 Torr. The authors used a Voigt model and a constrained multispectrum [92] fit approach. In this approach lines with the same absolute m values in the P and R branch are constrained to have identical half-width coefficients.

A custom Fourier transform spectrometer designed in Reims was used by Jarlot *et al.* [83] to study the fundamental (1-0) and first overtone (2-0) bands of carbon monoxide diluted by air and H_2. Devi *et a*l. [70] have measured the self- and air-broadened Lorentz half-width and pressure-induced shift parameters of CO, as well as their temperature dependence exponents in the (1-0) band. The authors have used spectra recorded over a temperature and pressure range from 151.15 to 298 K and 5.11 to 699.14 Torr, respectively.